Multi Walled Carbon Nanotube Based Chemoresistive Methane Sensors

BY

Md Tanim Humayun
B.Sc., Bangladesh University of Engineering and Technology, 2008
M.S., University of Illinois at Chicago, 2013

THESIS

Submitted as partial fulfillment of the requirements
for the degree of Doctor of Philosophy in Electrical and Computer Engineering
in the Graduate College of the
University of Illinois at Chicago, 2016

Chicago, Illinois

Defense Committee:
Dr. Igor Paprotny, Chair and Advisor
Dr. Ralu Divan, Argonne National Laboratory
Dr. Lara Gundel, Lawrence Berkeley National Laboratory
Dr. Paul A. Solomon, US Environmental Protection Agency
Dr. Alan Feinerman
Dr. Michael Stroscio

To my parents, my teachers, and my wife.

ACKNOWLEDGMENTS

I must mention my supervisor Dr. Igor Paprotny, my mentor/philosopher Dr. Ralu Divan, and two of my best teachers, Dr. Lara Gundel and Dr. Paul A. Solomon, for their invaluable guidance.

I am specially thankful to Dr. Alan Feinerman and Dr. Michael Stroscio who were members of my defense committee.

My wife Umme Shainaz Urmee was always with me in the difficult periods of my PhD life.

I would like to mention my uncle Dr. Fayzul Pasha for his moral support in critical times.

In particular I would like to thank Liliana Stan, Dr. Yuzi Liu, Dr. David Gosztola, Daniel Rosenmann and Suzanne Miller of Center for Nanoscale Materials (CNM), Argonne National Laboratory (ANL); Dr. Alex B. Martinson of Materials Science Division (MSD), ANL; Dr. Richard Rosenberg of Advanced Photon Source (APS), ANL; and Troy Cados of Lawrence Berkeley National Laboratory (LBNL) for their important assistance in various fabrication steps and characterization of the methane sensor.

I am grateful to all members of the Air-microfludics group (AMFG) and the Micro-mechatronics Lab (MSL) at UIC.

Finally, I always accuse my friend and brother poet Zafar Ahmad Rashed for seeding in my mind the idea of pursuing a PhD.

Use of the Center for Nanoscale Materials and Advanced Photon Source, Office of Science user facilities, was supported by the U. S. Department of Energy, Office of Science, Office

ACKNOWLEDGMENTS (Continued)

of Basic Energy Sciences, under Contract No. DE-AC02-06CH11357. The project is in part funded by a grant from Aclima Inc., award # 2015-07496 and College of Engineering, UIC. The US Environmental Protection Agency, through its Office of Research and Development, collaborated in the research described here.

M T H

TABLE OF CONTENTS

TABLE OF CONTENTS (Continued)

CHAPTER **PAGE**

LIST OF TABLES

LIST OF FIGURES

LIST OF FIGURES (Continued)

LIST OF FIGURES (Continued)

LIST OF FIGURES (Continued)

LIST OF FIGURES (Continued)

LIST OF FIGURES (Continued)

FIGURE **PAGE**

LIST OF FIGURES (Continued)

FIGURE **PAGE**

LIST OF ABBREVIATIONS

ALD	Atomic Layer Deposition
ALD	Atomic Force Microscopy
AMFG	Air-Microfludics Group
ANL	Argonne National Laboratory
APS	Advanced Photon Source
CNM	Center for Nanoscale Materials
CNT	Carbon Nanotube
CRDS	Cavity Ring-Down Spectroscopy diethylzinc
DEZ	Diethylzinc
DMSS	Distributed Methane Sensor System
DRIE	Deep Reactive Ion Etching
GPM	Gaussian Plume Model
HRTEM	High Resolution Transmission Electron Microscope
IR	Infrared
LBNL	Lawrence Berkeley National Laboratory
LDL	Lowest Detection Limit
LOR	Lift-off Resist

LIST OF ABBREVIATIONS (Continued)

MWCNT	Multi Walled Carbon Nanotube
MONCs	Metal Oxide Nano-crystals
NCF	Nanotechnology Core Facility
NCs	Nano-crystals
NPs	Nano-particles
PPM	Parts per Million
PL	Photoluminescence
PVD	Physical Vapor Deposition
QCL	Quantum Cascade Laser
RH	Relative Humidity
RIE	Reactive Ion Etching
RT	Room Temperature
SEM	Scanning Electron Microscopy
SnO_2-MWCNT	Tin Oxide Functionalized Multi Walled Carbon Nanotube
SOI	Silicon on Insulator
SSA	Specific Surface Area
SWCNT	Single Walled Carbon Nanotube
TM	Tangential Mode

LIST OF ABBREVIATIONS (Continued)

TEM	Transmission Electron Microscope
UIC	University of Illinois at Chicago
USEPA	The U.S. Environmental Protection Agency
UV	Ultra Violet
UVO	Ultra Violet Ozone
XPS	X-ray Photoelectron Spectroscopy
ZnO-MWCNT	Zinc Oxide Functionalized Multi Walled Carbon Nanotube

SUMMARY

Carbon nanotube (CNT) low power chemoresistive sensors have the potential to detect sub-ppm levels of methane (CH_4), one of the most prominent greenhouse gases. Multi-walled carbon nanotube (MWCNT) surface was activated by O_2-plasma or UV-O_3 (UVO) treatment. This was followed by deposition of metal-oxide nanocrystals (MONCs) on to the surface of MWCNTs. The sensor surface has been functionalized for methane by this process. Surface-activated, MONCs-functionalized MWCNT chemoresistors were able to sense 10 ppm of methane in dry air at room temperature.

The effects of O_2-plasma and UVO activation of the MWCNT surface have been studied using Raman spectroscopy, X-ray photoelectron spectroscopy (XPS), and transmission electron microscopy (TEM). The morphology of the MONCs, deposited by atomic layer deposition (ALD) process on to the MWCNT surface, was characterized by scanning electron microscopy (SEM) and TEM; the chemical composition was characterized by energy dispersive x-ray spectroscopy (EDS) and Raman spectroscopy; the crystal quality was characterized by Raman spectroscopy and TEM. The photonic property of the functionalizing ZnO nanocrystals has been characterized by photoluminescence (PL) spectroscopy. Characterization results suggest reactive functional groups such as COOH, COH, and C=O are formed as a result of surface pre-activation of MWCNT, and are essential for the nucleation and binding of the high crystal quality MONCs on to the MWCNT surface.

SUMMARY (Continued)

Surface pre-activated and MONC-functionalized MWCNT (MONC-MWCNT) chemoresistor methane sensors were tested at room temperature in presence of 10 ppm methane in dry air mixture. The sensitivity of the sensor was 4 times higher at 10 ppm methane compared to other existing sensors. The improved performance of the sensor is a result of strong electron transfer to the MONCs from methane molecules and energetically favorable electron transport at the junction between these particular MONCs (i.e., ZnO or SnO_2) and MWCNT. The surface pre-activation processes were essential for functionalization of MWCNT by the ZnO or SnO_2 NCs and hence the reversible response of the sensor in presence or absence of 10 ppm methane in dry air. Compared to UVO technique the O_2-plasma based surface pre-activation process was more effective in enhancing sensor response to 10 ppm methane in air mixture. After being exposed to the methane in air mixture the change in the resistance of the sensors was reversed by N_2 purging, zero air purging, N_2 purging along with UV irradiation or UV irradiation alone. UV irradiation was highly effective in reducing the sensor recovery time. As a result of the UV irradiation, the recovery time was reduced 2 orders of magnitude compared to previous result.

Change in baseline resistance of the MONC-MWCNT sensor as a function of varying relative humidity was studied as well. The sensors showed strong dependence on RH change necessitating the fabrication of a differential resistive grid composed of selectively functionalized CNTs. The differential grid uses constructive and destructive interference of the responses from different grid elements at different RH levels, hence nullify the RH interference during methane sensing.

CHAPTER 1

INTRODUCTION

Despite having a shorter lifetime than CO_2, CH_4 is more efficient at trapping infrared radiation (1; 2). The impact of CH_4 on climate change is estimated to be 25 times stronger than CO_2 (pound for pound) over a 100-year period (2). In 2013, 10% of emitted greenhouse gas in the US was CH_4, while 29% of CH_4 emission was thermogenic, i.e., the source is man-made, such as natural gas and petroleum systems (2). Hence, an extensive deployment of low cost, highly sensitive, selective, and continuous CH_4 monitoring networks throughout the natural gas extraction and distribution infrastructure is of vital importance.

The objective of this research was to develop a methane sensor with (a) high sensitivity to methane: achievable by tuning the composition and dimension of the nanocomposites; (b) low power consumption: achievable by using state-of-the-art nanomaterials; (c) low cost: achievable by using microfabrication processes; and (d) highly selective only to methane: achievable through use of nanostructure engineering.

Surface pre-activated MONC functionalized multi-walled carbon nanotube (MONC-MWCNT) chemoresistive CH_4 sensors were developed able to detect 10 ppm CH_4 in air at room temperature. The sensors were fabricated using the cleanroom facilities at the Center for Nanoscale Materials (CNM) at Argonne National Laboratory (ANL) and Nanotechnology Core Facility at the University of Illinois at Chicago (UIC). Different characterization tools at the CNM at ANL, and the Advanced Photon Source (APS) at ANL were used to characterize the morphology,

chemical composition, and nano-scale dimension of the surface activated and MONC-MWCNT. O_2 plasma and UVO techniques were developed to activate the inert surface of bare MWCNT. Surface activation helped nucleation and binding of MONCs (ZnO or SnO_2) on to the surface of the MWCNT. An ALD-based MONC functionalization of surface pre-activated MWCNT was developed. Surface activated and MONC-MWCNT chemoresistor sensors were tested with 10 ppm CH_4 in air at the Air-Microfludics Group (AMFG) laboratory at UIC. The Indoor Environment Group, at Lawrence Berkeley National Laboratory (LBNL) collaborated in developing the experimental system for characterizing the sensitivity and selectivity of the MONC-MWCNT sensor. The U.S. Environmental Protection Agency (USEPA), through its Office of Research and Development, collaborated on the research described here.

The structure of the thesis is as follows: Chapter 2 provides a background of the work and discusses the motivation behind using MWCNT to build chemoresistive CH_4 sensors; Chapters 3 and 4 present studies of CH_4 sensors with zinc oxide (ZnO) and tin oxide (SnO_2) nanocrystals functionalized MWCNT; Chapter 5 discusses the effect of surface activation on MONC-MWCNT CH_4 sensors; Chapter 6 discusses UV surface recovery of the MONC-MWCNT sensor from exposure to CH_4; Chapter 7 describes an algorithm for a distributed CH_4 sensing system based on the fabricated MONC-MWCNT sensors; the conclusion is presented in Chapter 8.

CHAPTER 2

BACKGROUND

CH_4 sensing technologies, available commercially or in literature, can be divided into two broad branches: optical and chemical.

Section 2.1 presents a survey of optical methane monitoring technologies. Section 2.2 reviews chemical CH_4 monitoring technologies. Section 2.2.1 describes metal oxide chemoresistive CH_4 sensors. Section 2.2.2 analyzes CNT chemoresistive CH_4 sensors from the perspectives of: (a) fundamental properties of the CNT chemoresistive sensor, (b) comparison between multi- and single-walled CNT, (c) functionalization of MWCNT, and (d) surface activation of MWCNTs. Section 2.3 summarizes the discussion.

2.1 Optical methane monitoring technologies

One of the most common optical CH_4 monitoring technologies uses the filtered IR detection, which can detect methane in the ppm range from its absorption of IR light. This technology has been widely used in gas extraction, transmission, and distribution pipelines. An airborne IR spectroscopic remote measurement method measures CH_4 plumes released from anthropogenic sources including oil and gas infrastructure (3). Massie et. al. (4) reported an optical sensor for CH_4 detection with a 1 % response at 500 ppm of CH_4. Lai et al. (5) reported an on-chip methane sensor using near-IR absorption with a detection limit of 100 ppm and a response of

almost 1 %. Nadezhdinskii et al. (6) reported a near-IR diode laser based CH_4 sensor with a detection limit of 10 K ppm of CH_4.

The strongest optical absorption of CH_4 occurs in the mid-IR region, around 3.3 μm (7). However, other hydrocarbon gases have absorption bands/lines in the same spectral region, hence, mid-IR CH_4 detectors are not methane-specific (4). Also, mid-IR CH_4 detectors are expensive and often need to be cooled to achieve better signal-to-noise ratios, increasing their power consumption (8).

An absorption line in near-IR region can be used to overcome the limitations of mid-IR CH_4 detectors. However, the near-IR absorption line of CH_4 is significantly weak, giving rise to considerable noise even when operated at room temperature (4).

Another commonly used optical CH_4 monitor, Cavity ring-down spectroscopy (CRDS), is based on an optical cavity. IR absorption loss in the optical cavity is measured to quantify the mole-fraction of the gases (9). The isotopic ratios of the stable isotopes of both carbon and hydrogen, along with the atmospheric concentration and distribution of the CH_4, can be used to derive the location and magnitude of CH_4 sources. CRDS is a laser-based technique where IR absorption loss in a sample cell is measured to quantify the mole-fraction of the gases (9). Rella et al. (9) reported a CH_4, $\delta^{13}CH_4$, and C_2H_6 monitoring instrument based on CRDS with a detection limit for CH_4 of 0.4 ppb. Roscioli et al. (10) reported a dual-tracer flux measurement to measure magnitude and origin of CH_4 from natural gas gathering and processing facilities with a detection limit of 3 ppb. Quantum cascade laser (QCL) spectrometers (CH_4 detection limit of 1 ppb) along with CRDS were used in their two mobile laboratories (operated by

Aerodyne Research Inc. and Carnegie Mellon University) to measure CH_4. Jahjah et. al. (11) reported a QCL CH_4 monitoring technique with a lower detection limit of 62 ppb. The principal limitation of CRDS and QCL are their complex structure and immobility making the detection technologies significantly expensive (12).

2.2 Chemical methane monitoring technologies

Three configurations of chemical methane sensors are possible: (a) electrochemical, (b) chemoresistor, and (c) chemical field effect transistor (chemFET).

In an electrochemical sensor CH_4 is passed through an electrochemical cell. Current flowing through the cell changes due to oxidation of methane by the electrolyte solution (13). The principal limitation of electrochemical sensors are their short lifetime (14).

A chemoresistive gas sensor is a variable resistor whose resistance varies as a result of chemisorption of CH_4 on the sensor surface (Figure 1). Consequently, the resistance change in a chemoresistor CH_4 sensor is directly related to the concentration of the nearby CH_4. Metal oxides are widely used for chemoresistors.

A ChemFET can be considered a chemoresistor with an external gate voltage bias. Gate voltage helps to create a conductive channel. ChemFET CH_4 sensors are not as widely used as chemoresistors and CH_4 sensors and have not been reported. Probably because the electronics of chemFET are more complex than for chemoresistors. ChemFET also needs an additional voltage source. Hence the discussion below emphasizes metal oxide and CNT chemoresistor CH_4 sensors.

2.2.1 Metal oxide chemoresistive methane sensors

Metal-oxides, such as zinc oxide (ZnO), tin oxide (SnO_2), indium oxide (In_2O_3), both in bulk and nanoscale form, have been widely used to build micro-fabricated, low-cost chemoresistive methane sensors (15; 16; 17). Figure 2 illustrates a commonly accepted physical and energy-band model for metal oxide chemoresistive methane sensors (18; 19). It shows the individual grains of an n-type metal oxide semiconductor (such as ZnO or SnO_2) connected with an electrical source (not shown in the picture). Figure 2a shows the grains and adsorbed oxygen on their surfaces, where the adsorbed oxygen attracted the conduction electrons from the near-surface region of the grains, leading to formation of an insulating electron-depleted layer (18; 19). Figure 2b illustrates the band model corresponding to the physical model of the metal oxide powder grains. To conduct current, electrons must pass from one grain to the next, passing through these electron-depleted insulating regions or barrier. The barrier the electrons need to overcome is indicated as qV_s (q is the charge of an electron and V_s is the potential height of the barrier), where V_s increases as the concentration of O^- increases. The higher the concentration of oxygen on the surface, the higher the barrier, resulting in fewer electrons making the transition, and a higher resistance. This model is based on the following 2 chemical half reactions:

$$2O_2 + 4e^- \rightarrow 4O^- \tag{2.1}$$

$$CH_4 + 4O^- \rightarrow CO_2 + 2H_2O + 4e^- \tag{2.2}$$

Net reaction:

$$CH_4 + 2O_2 \rightarrow CO_2 + 2H_2O \tag{2.3}$$

A steady state between these two reactions determines the concentration of O^- on the surface of the semiconductor determines V_s, and therefore, determines the conductance of the sensor.

Various catalysts, such as platinum (Pt) (20), rhodium (Rh) (21), osmium (Os) (22), potassium (K) (23), calcium (Ca) (23), and magnesium (Mg) (23) speed up the chemical reaction, hence increasing the response ($\Delta R/R$) of the metal-oxide sensors. But continuous heating is necessary to initiate the chemisorption of oxygen on these metal-oxides. Consequently the power consumption of these sensors is high (hundreds of mWs and higher) (15; 16; 17). A summary of various parameters for metal oxide chemoresistor sensors is presented in Table I.

2.2.2 CNT chemoresistive methane sensors

This section covers background information on (a) fundamental properties of CNT chemoresistive sensors, (b) comparison of multi- and single-walled CNTs, (c) functionalization of CNT, and (d) surface activation of MWCNTs.

2.2.2.1 Fundamental properties of CNT chemoresistive sensors

CNTs were discovered by Iijima (24). In his 1991 letter to "Nature" magazine he reported "a new type of finite carbon structure consisting of needle-like tubes". He used an arc-discharge evaporation method where the "needle" grew on the negative end of an electrode.

Dresselhaus et. al. (25), in their 1995 article on CNTs, defined them as: "[CNTs are] like rolled-up cylinders of graphene sheets of sp^2 bonded carbon atoms, except that the tubule diameters in some cases are small enough to exhibit the effects of one-dimensional (1D) periodicity".

Zhang et. al. (26) reported that due to the conversion from a uniform distribution of electron clouds in graphite to an asymmetric distribution of electron clouds around cylindrical nanotubes, a rich π-electron conjugation forms outside of the CNTs, making them electrochemically active. Consequently when electron-withdrawing/electron-donating molecules (e.g. NO_2 or CH_4) interact with the semiconducting CNTs, they alter the density of electrons/holes in the "core" of the nanotube, changing the overall conductance of CNTs (26). This is the primary reason for using CNTs as gas sensors. Due to the very high surface area-to-volume ratio, CNTs show greater absorptive capacity, resulting in a remarkable modulation of the electrical properties in the presence of target gas molecules (26; 25; 27; 28), which enables the detection of some gases at low ppm at room temperature.

Because of low power consumption, the CNT chemoresistors are very attractive candidates as methane sensors. Overall, the large response to methane, low power requirements, low-cost (due to batch microfabrication processes), and low response to temperature make CNT-based sensors ideal for distributed outdoor leak detection applications. A summary of various parameters for CNT chemoresistor sensors is given in Table II.

2.2.2.2 Comparison between multi- and single-walled CNT

MWCNTs have lower specific surface areas (SSA, m^2/g) than single-walled carbon nanotubes (SWCNTs) (29). SSA depends on the total mass of the carbon atoms in the CNT, and the total mass of the carbon atoms is much higher for MWCNTs than SWCNTs. The outermost shell of a MWCNT is of more interest, since, according to the proposed gas sensing mechanism described in the literature, electron transfer takes place between the CNT and the gas molecules via a functional groups on the surface of the CNT (27; 28). Therefore, compared to MWCNTs, SWCNTs offer no additional advantages in accessing gas molecules. Rather, MWCNTs work like larger diameter SWCNTs with current primarily flowing through the outermost shell. The core of the nanotube acts as a "mechanical support" for the electrically active outermost shell (30).

In addition, MWCNTs are easier to grow and less expensive than SWCNTs. Consequently, the MWCNTs are more attractive than the SWCNTs for sensing methane.

2.2.2.3 Functionalization of MWCNT

Pristine MWCNT chemoresistive gas sensors have the following limitations: (a) low response to gas molecules for which MWCNT has a low affinity, (b) low selectivity to target gases, (c) irreversibile resistance change, and (d) relatively long recovery time.

The available literature shows that to obtain selective, reversible gas sensing with shorter recovery time it is necessary to functionalize the surface of the CNTs, i.e, embed it with active sites, through controlled deposition of nano-materials on the surface of CNTs (27; 28; 31; 32; 33). Nano-scale integration of MONCs and MWCNTs opens a unique path to building sensitive (i.e

high $\Delta R/R$ at low ppm range) and selective chemoresistor gas sensors that operate without external heat.

The CH_4 sensor described here uses MWCNTs functionalized by metal oxide nanocrystals (MONCs) to sense methane. We used two well known MONCs, ZnO and SnO_2 that are widely used methane sensing materials and are inexpensive. ZnO and SnO_2 promote energetically favorable electron transport at the MO–MWCNT junction (34; 28). The work function of ZnO was reported to be almost 4.64 eV (35) or 5.2 eV (36), while SnO_2 has a work function of 4.7 eV (28). The work functions of these MONCs are almost equal to the work function of MWCNTs (4.7-4.9 eV) (28; 37). Therefore, the Schottky barrier height at the MONC-MWCNT junction is low, making it easy for the electrons to transfer between MWCNTs and MONCs. The low Schottky barrier improves the overall sensitivity of the sensor (i.e high $\Delta R/R$ at low ppm), making the hybrid MONC-MWCNT system a potentially superior sensing element to either of its constituent components (28).

Figure 3 shows the gas sensing mechanism of the MONC-MWCNT sensor. The surfaces of pre-treated MWCNTs are reported as p-type (38; 28), whereas ZnO and SnO_2 MONCs are n-type (28; 39). Consequently, a p-n junction and a depletion region are formed at the interface of MONC-MWCNT. Lu et al. (28) proposed that when a SnO_2-MWCNT comes in contact with an oxidizing gas such as NO_2, as a result of acceptance of electrons by the oxidizing gas molecules, the depletion region at the MONC-MWCNT junction increases. Therefore, the Fermi level (E_F) of the p-type MWCNT shifts closer to the valence band and the electrical conductance of the p-type MWCNT increases (28). Accordingly, when the hybrid structure of an n-type

MONC and a p-type MWCNT interact with CH_4, a reducing gas, because of electron donation, the depletion region at the MONC-MWCNT junction decreases. The Fermi level (E_F) of the p-type MWCNT also shifts further from the valence band, decreasing the electrical conductance of the p-type MWCNT. Results presented in this dissertation are consistent with earlier studies that describe the relative change in resistance due to CH_4 exposure as follows:

$$\Delta R/R = (R_{methane} - R_{air})/R_{air}$$

R_{air} is defined as the initial resistance of the sensor before it is exposed to CH_4 and $R_{methane}$ is the resistance in presence of air and methane and is assumed constant throughout the experiment or measurement period.

2.2.2.4 Surface activation of MWCNTs

It is challenging to embed functionalizing particles on the surface of a bare CNT due to the inertness arising from sp^2 "graphitic" carbon impeding the binding of the functionalizing particles with the MWCNT surface (40). Therefore, conventionally, prior to embedding functionalizing materials, the surfaces of bare CNTs are activated by exposing them to gases at high temperature (41) and/or through wet chemistry (42). High temperature and air-exposure may actually destroy or excessively damage the MWCNTs (41). Acid treatments used in wet chemistry can degrade the mechanical and electronic performance of the CNTs by introducing large numbers of defects (40). Wet chemistry also involves several additional steps, such as dissolution, sonication, mixing and drying, these processes also often cause undesirable agglomeration of treated MWCNTs (41).

To increase the efficiency of the functionalizing process, two alternative dry activation processes have been previously reported: (a) gas plasma (43; 42; 41), and (b) UV-ozone (UVO) treatment (44).

O_2 plasma pre-treatment creates -C$^{\cdot}$ free radicals on the MWCNT surface. When exposed to atmosphere, -C$^{\cdot}$ free radicals react with the atmospheric H_2O to produce functional groups such as -COOH (carboxyl), =CO (carbonyl), COH (alcohol), and -C-O-C (ether) (42; 45; 46).

During UVO activation O_2 molecules are excited by the UV light from their ground spin-triplet state into a singlet state. This reduces the energy required for O_2 to react with the MWCNT surface and gives rise to these groups on the surface of the MWCNTs (44). Both the gas plasma and UVO exposure have no effect on the aspect ratio (i.e. length to diameter ratio) of the MWCNTs (40). These polar chemical groups consequently act as active sites for the nucleation of MONCs (42; 45; 46; 40), which improve the capacity of the MWCNT to adsorb CH_4 .

2.3 Summary

In this chapter different sensing properties of existing methane monitoring systems were surveyed. The operating principle, advantages, and disadvantages of commercially available and reported optical CH_4 sensors were discussed. The principal disadvantage of the metal oxide chemoresistive CH_4 senors, i.e., high power consumption was explained from the perspective of a reported energy band model-based mechanism. Important physical and chemical properties of MWCNTs, arising from its nano-scale dimension were described. The reported mechanisms for CNT-based CH_4 sensors were reviewed and a hypothesis was developed. The MWCNT was

compared with the SWCNT and the basis of using MWCNTs instead of SWCNTs for CH_4 sensing was explained. An analysis of the dry processes, such as UVO or O_2 plasma methods, for pre-activating the surface of the MWCNT, was also presented.

In comparison to existing methane monitoring systems MWCNT chemoresistor CH_4 sensors are low power consuming, have the potential to selectively and reversibly detect low-ppm CH_4, are easy to fabricate, and less-expensive. ZnO and SnO_2 are widely used methane sensing materials and are inexpensive. They promote energetically favorable electron transport at the MO–MWCNT junction. Hence, to improve the CH_4 adsorption-capacity of the MWCNTs we deposited ZnO and SnO_2 NCs on pre-activated MWCNT surfaces.

---

[1]Definitions of parameters described in Table I and Table II: N.M. = Not-mentioned. RT = Room temperature. LDL: lower detection limit; vol % = 1 cc methane/100 cc balance gas; $\Delta I/I$ = relative change of current passing through a chemoresistor sensor. In general: response time = time required for reaching 90 % of maximum resistance; recovery time = time for reducing to 10 % of maximum resistance starting from 90 % of maximum resistance.

TABLE I: Characteristics of metal oxide chemoresistive methane sensors.

Material	Response $\Delta R/R$ in percent	LDL	Response Time	Recovery Time	Operating Temperature	Interferences	Ref.
Pd-SnO_2	80	1000 ppm	10 s	10 s	385 °C	CO, H_2, C_3H_8, C_4H_{10}	(47)
Os-SnO_2	160	1000 ppm	2.5 min	4 min	200 °C	N.M.	(22)
Ca-SnO_2	24	1000 ppm	N.M.	N.M.	400 °C	N.R.	(48)
Ca, Mg, K-SnO_2	80 (Ca), 30 (Mg), 60 (K)	1000 ppm	N.M.	N.M.	400 °C	N.M.	(23)
ZnO (Thin Film)	40	1 vol %	8.3 s	11.7 s	250 °C	H_2	(49)
ZnO (1D struc.)	1.75	100 ppm	1 min	2-3 min	300 °C	H_2, CO	(15)
Pd-ZnO	47.5	1 vol %	4.6 s	22.7 s	70 °C	H_2	(50)
In_2O_3	40	6000 ppm	N.M.	N.M.	350 °C	N.M.	(17)

Note.[1]

TABLE II: Characteristics of CNT chemoresistor sensors

Material	Response in percent	LDL	Response Time	Recovery Time	Operating Temperature	Interference Gases	Ref.
Pd-SWCNT	$\Delta I/I = 0.02$	15 ppm	3.3 min at 40 °C	N.M.	R.T.	N.M.	(27)
Pd-MWCNT	$\Delta R/R = 0.03$	3 vol %	35 s	10 s	R.T.	H_2, NH_3	(51)
Pd-MWCNT	$\Delta R/R = 4$	2 vol	310 s	176 s	R.T.	N.M.	(42)
Carbon Nanofiber	$\Delta R/R = 15$	500 ppm	45 s	N.M.	R.T.	N.M.	(52)

Note.[1]

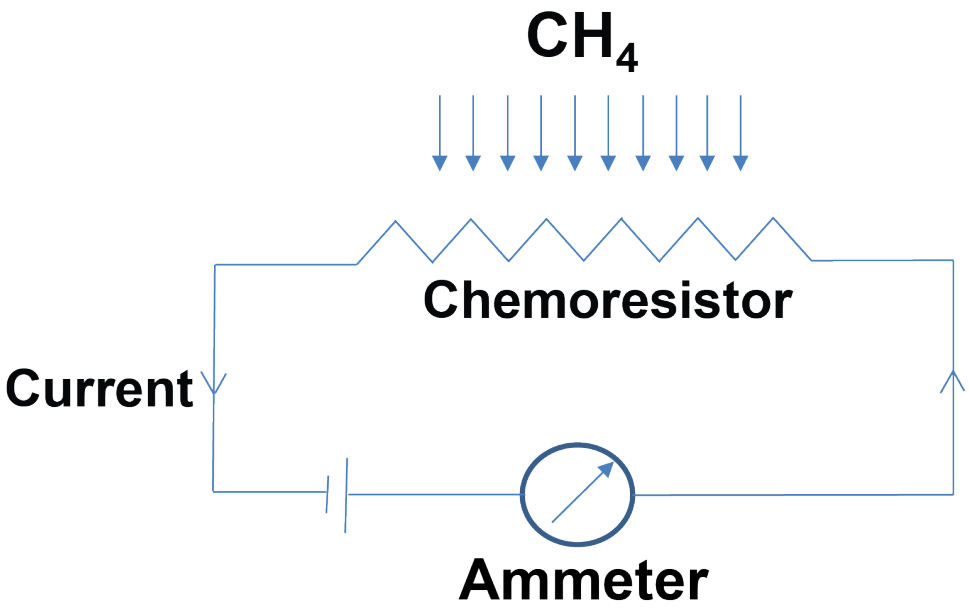

Figure 1: Fundamental model for a chemoresistor CH_4 sensor. The current measured by the ammeter varies according to the resistance change of the chemoresistor which is a function of the concentration of CH_4 molecules present.

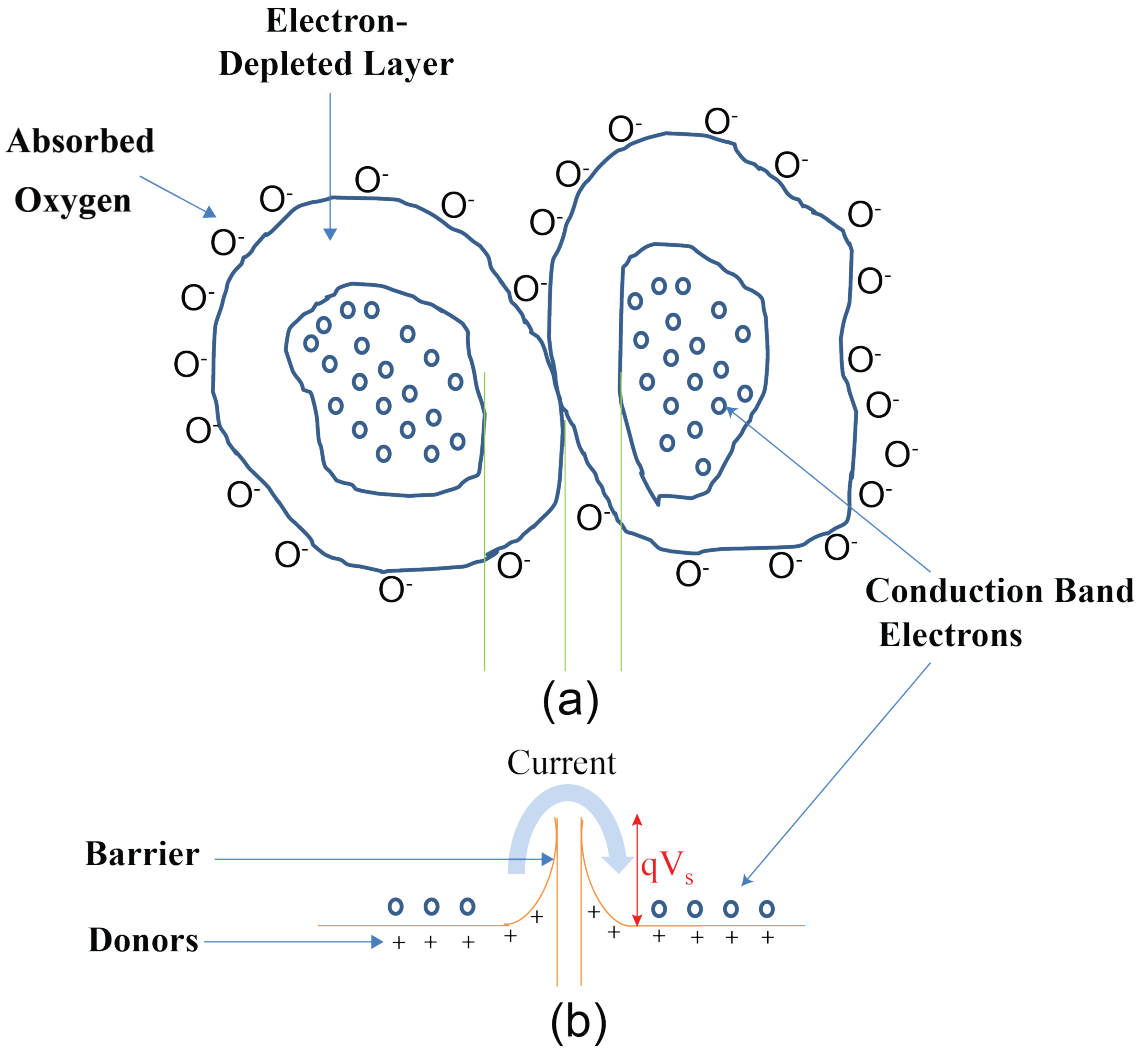

Figure 2: (a) The illustration shows two contacting metal oxide powder grains that form depletion regions at the points of contact, as a result of electron entrapment by the absorbed oxygen molecules. (b) The band model corresponding to the physical model of the metal oxide powder grains.

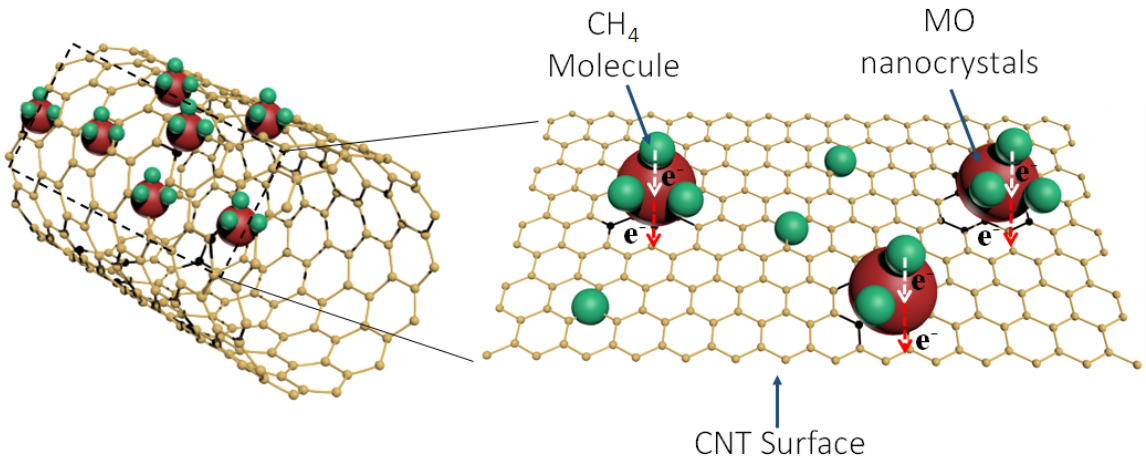

Figure 3: Proposed sensing mechanism of surface pre-activated MONC-MWCNT chemoresistor sensors. The surface of the chemoresistor adsorbs methane molecules and triggers electron transfer, changing the resistance of the MONC-MWCNT.

CHAPTER 3

ZINC OXIDE NANOCRYSTALS FUNCTIONALIZED MWCNT-BASED METHANE SENSORS

(A major portion of the chapter was previously published as: "ZnO Functionalization of Multi-walled Carbon Nanotubes for PPM Level Methane Sensing", Md Humayun, R. Divan, L. Stan, A. Gupta, D. Rosenmann, L. Gundel, P. A. Solomon, and I. Paprotny, J. Vac. Sci. Technol. B 33, 06FF01 (2015))

Despite the high potential for modulating electron transport, bare CNTs are insensitive towards most target gases due to poor gas interaction with the pristine graphitic surfaces. Consequently, chemoresistive gas sensing requires either covalent (based on carboxylic acid groups) or non-covalent (based on supramolecular complexation) functionalization of CNTs with analyte-specific entities to enable modulation of their electrical properties in the presence of a target gas (26). Atomic layer deposition (ALD) allows precise, uniform and conformal deposition of oxide coatings on geometrically complex substrates, such as MWCNTs (53; 54), enabling their non-covalent functionalization. In particular, ZnO nano-particles have been previously reported as a promising methane sensing material (15; 55) and promote energetically favorable electron transport at the ZnO-MWCNT junction (34) compared with previously reported Pd-MWCNT (28). Consequently ZnO was chosen as a functionalizing material for surface pre-treated MWCNTs. Three key characteristics make ZnO-MWCNT hetero-structures one of the most attractive chemoresistive sensors for ppm level CH_4 detection: (a) the large relative resistance change of

ZnO NPs to low levels of CH_4; (b) energetically favorable electron transport at ZnO-MWCNT junction, and; (c) a strong electrical current modulation potential due to ballistic transport of electrons through the MWCNTs. This chapter focuses on the design and fabrication of a methane sensor based on MWCNTs functionalized with ZnO deposited by ALD. This chapter is structured as follows: Section 3.1 describes the fabrication and ZnO functionalization of the MWCNT-based methane sensor. The experimental protocol used to conduct methane exposure experiments is described in Section 3.2. Section 3.3 describes the experimental results, among other the resistance change down to 2 ppm of CH_4 at room temperature. Summary remarks are offered in Section 3.4.

3.1 Fabrication

The fabrication of the ZnO-MWCNT methane sensor is described in Figure 4. A 1 μm thick SiO_2 layer was grown on Si (100) wafers using wet oxidation at a temperature of 1100 °C for 3 hr. (Figure 4a). Following the growth of the oxide layer, a set of interdigitated gold (Cr/Au) electrodes were fabricated on the SiO_2 coated Si wafer, implementing a lift-off based photolithography technique (Figure 4 b-f). A bi-layer of Microchem Lift-Off Resist 3A (LOR 3A) and S 1813 photoresists was spin-coated onto the SiO_2/Si wafer while a direct laser writer (LW 405) was used to do the optical exposure (Figure 4b, c). After the development process (Figure 4d) a 100 nm Au film on top of a 10 nm Cr layer was deposited on the patterned photoresist using a PVD 250 Lesker e-beam evaporator (Figure 4e). Deposited metal was lifted off by ultrasonicating the samples immersed in an 1165 remover bath (Figure 4f). Gaps between the interdigitated electrodes varied in the range of 5 μm to 10 μm (Figure 5).

A batch of 98% pure MWCNTs with 12 nm average diameter, 10 μm average length, and a specific surface area of about 220 m^2/g was purchased from Sigma Aldrich. An ultrasonicated solution of 1 mg/50 mL of MWCNTs in ethanol was used to produce a well dispersed MWCNT mesh. Using a micro-syringe, 50 μL aliquot was deposited on an 1 mm^2 active area of the fabricated metal electrodes, which was followed by baking at 75 ° C to remove the solvent and to improve adhesion (Figure 4g, Figure 6). The deposited MWCNTs were O_2 plasma or UVO treated inside a reactive ion etching chamber (March RIE) and a UVO chamber (Nanomax Ultra- 100), respectively, for durations varying from 5 min to 60 min (Figure 4h). The ALD method was used to deposit ZnO nanoparticles onto the surface pre-treated MWCNTs. Using diethylzinc (DEZ, $(C_2H_5)_2Zn$) as a precursor, ALD populated the surface of the MWCNTs with ZnO nanoparticles at the oxygeneted defects on the MWCNTs (Figure 4i). An Arradiance Gemstar tool was used to carry out the ALD. ALD temperature varied from 175 to 220 °C . The deposition process consisted of 48 cycles. The exposure time for both DEZ and water vapor was 22 ms. The DEZ reacted with H_2O through the following chemical reaction:

$$Zn(C_2H_5)_2(g) + H_2O(g) \rightarrow ZnO(s) + 2C_2H_6(g) \tag{3.1}$$

The ALD process resulted in the formation of ZnO nanoparticles from 7.74 nm to 10.8 nm in size (mean "diameter") on the MWCNT surface, which was confirmed by TEM. The electrical conductivity of the fabricated electrodes, the MWCNT-deposited resistive network, and ALD-functionalized-MWCNT devices were measured using a digital multimeter (Fluke 115). Parasitic and contact resistance was on the order of single-digit ohm values and was

considered insignificant compared to the resistance of the chemoresistor (100 Ω to 5 MΩ). The VEGA 3 (Tescan) SEM was used to image the ZnO-MWCNTs and perform the EDX on the ZnO-MWCNT samples. A micro-Raman system (Renishaw Invia) was used (at 514 nm green laser) for characterization of the ZnO-MWCNT samples at room temperature. The power of the incident laser and acquisition time for the Raman signals were kept constant during the analyses of the samples fabricated by the process described above.

3.2 Experimental setup

ZnO-MWCNT sensors were tested in a sealed test chamber (1.43 L) connected with gas inlets and electrical feedthroughs (Figure 7 shows a schematic of the test set up). The residence time (equal to 3 volume changes) of flow through the chamber was 4.5 min at a flow rate of 0.94 L/min. Relative humidity and temperature inside the test chamber were continuously monitored and recorded by a commercial data-logger (HOBO U-10 series). A computer with a custom interface circuit and an analog-to-digital converter recorded electrical signals generated from the sensors in real time. A mixture of 10 ppm methane in dry air (Praxair Inc.) was introduced to the chamber at a constant flow rate (0.94 L/min) and monitored by a rotameter for 30 min. The relative humidity inside the test chamber was kept constant, confirmed by the humidity sensor. Dry N_2 or synthetic air (a specific synthesis of 79.19 % of N_2 and 20.81 % of O_2) was used to purge CH_4 mixture from the chamber and to recover the devices to their baseline resistance after each CH_4 exposure. To verify the detection limit at low CH_4 concentrations, the change in electrical resistance of the sensors was also monitored while they were placed inside a plastic glove box filled with 2 ppm of CH_4 in ambient air. A commercially available CH_4

detector (Tpi 721, manufacturer: Test Products International) confirmed the concentration of CH_4 . The commercial reference sensor used in this experiment (Tpi 721, manufactured by Test Products Int.) only provides accurate data under static conditions (i.e., no flow) since it is highly sensitive to surrounding gas flow (56). The metal oxide based microfabricated chemoresistor (Figaro 2611, manufactured by Figaro USA Inc.) in the Tpi 721 commercial sensor has a high relative power requirement limiting its use, e.g., when power is not available or many measurements are required.

3.3 Results and discussion

In order for the MWCNT network to function as a chemoresistor, the ALD-deposited ZnO should not create a direct conductive path between the electrodes outside of the MWCNT mesh, i.e., the sensor electrodes were only connected via the MWCNT network. This was confirmed by electrical testing; depending on the structure of the interdigitated metal electrodes and the density of the deposited MWCNTs in ethanol solution. The resistance of the MWCNT-connected electrodes in the sensors varied between 100 Ω to 5 MΩ, while the resistance outside of the MWCNT mesh was infinite. The resistances of six of the MWCNT sensors, before and after the ZnO deposition by ALD, are presented in Table III. The results show little change (around 10 % on an average) in the resistance value before and after ALD. Original resistances of the sensors might vary because of lack of precision in MWCNT placement on the devices during drop deposition of the MWCNT solution. Variability in sensor resistance can be reduced by chemical assembly based placement of MWCNTs on patterned substrate, so that MWCNTs adhere only to selective parts of the patterns (57).

The ALD process was optimized for CNT functionalization, and thus the deposited ZnO creates a discontinuous layer that was not electrically conductive. This was verified by depositing ZnO on interdigitated Au electrodes only (not on CNTs). The resulting non-conductive 8 nm thick ZnO film (48 cycles of ALD) confirmed that CNTs were an essential constituent of the sensor element. SEM images confirmed that the functionalized MWCNTs were in proper contact with the interdigitated Au metal pads (Figure 6). SEM and EDX results showed that ZnO nanoparticles were only deposited on the active sites of the MWCNT surface rather than on the SiO_2 surface (Figure 8). The tendency of the ZnO nanoparticles to be deposited on the MWCNTs (active sites), rather than on the SiO_2 substrate, was increased as the ALD temperature was increased from 175 to 220 °C.

TEM results showed the uniform distribution of "spherical" ZnO NCs on the surface of the pre-activated MWCNTs (Figure 9a and Figure 9d). The deposited ZnO NCs was of high crystal quality with clear lattice fringes (Figure 9b and Figure 9e). It was found that as the ALD emperature was increased from 175 to 220 °C the mean diameter of the ZnO NCs increased from 7.74 nm to 10.8 nm (Figure 9c and Figure 9f).

The higher resolution TEM (HRTEM) image in Figure 10 illustrates the wurtzite structure of the ZnO NC and its good crystalline quality with clearly visible lattice fringes. The interplanar spacing of 2.8 Å, 2.68 Å and 2.48 Å correspond to <100>, <002> and <101> planes of ZnO(58).

Two different approaches were used to pre-treat the surface of the MWCNTs before the ZnO ALD, UVO and O_2 plasma. Both pre-treatments improved the affinity between the MWCNT

surface and functionalizing ZnO nanoparticles by producing nucleation sites for the nanoparticles on the MWCNT surface.

Raman spectroscopy of ZnO-MWCNT samples showed the characteristic Raman peaks (D, G and G') originating from the MWCNTs (39), as well as characteristic Raman peaks of ZnO (${E_2}^{high} - {E_2}^{low}$, ${E_2}^{high}$ and $A_1(LO)$) (39; 59) (Figure 11). As seen in Figure 11a - c, the ZnO modes were sharper and more intense at the higher temperature ALD grown samples compared to those originating at the lower temperatures. Based on the literature, the Raman frequency shift in the range of 566.51 to 574.92 cm^{-1}, for various samples processed under different conditions, is denoted as the $A_1(LO)$ peak of ZnO (39; 60). A Raman frequency shift in the range of 424 to 435.97 cm^{-1} is regarded as ${E_2}^{high}$, while the region 320.79 to 329.44 cm^{-1} is regarded as the ${E_2}^{high} - {E_2}^{low}$ peak of ZnO (39; 60). Raman peaks for different samples grown under different ALD temperatures are summarized in Table IV, which shows that the ${E_2}^{high} - {E_2}^{low}$ peak was not present in the Raman spectra of the 175 °C ALD sample. Furthermore, in the Raman spectra of the 175 °C ALD samples the ${E_2}^{high}$ and $A_1(LO)$ peaks were weak in comparison with those for samples grown at ALD temperature of 200 and 220 °C. The broadening of Raman peaks of ZnO nanoparticles compared to bulk ZnO crystals has been attributed to the confinement of optical phonons, oxygen deficiencies, and residual stress in the ZnO nanoparticles (61). The Raman results presented in Figure 11 and Table IV demonstrate that as the ZnO ALD temperature increases, the aforementioned three phenomena become less prominent, indicating that the ZnO crystal quality was improved. Superior crystal quality of the functionalizing ZnO nanoparticles enhances the electron transport in the MWCNT-ZnO

junction (34) thus having a positive impact on sensor performance with respect to relative resistance change ($\Delta R/R$), i.e., sensor response. It was important to ensure the chemical stability and robustness of the functionalizing material so that the sensor operates accurately in harsh environments (26). The high crystal quality of the functionalizing nanomaterials helps control or minimize cross-response to the gases listed below, and maintain better reversibility as the sensor undergoes aging (26; 62). However, only the response of 175 °C ALD samples was examined since the adhesion of the external metal wires to the Au electrodes or pads degraded significantly at higher ALD temperatures (the phenomenon is illustrated in Figure 12). A shadow mask based technique is being developed to overcome this issue.

The ZnO-MWCNT network exhibited significant resistance change when exposed to methane even at a low concentrations. Data presented in Figure 13a and b were obtained from ZnO-MWCNT sensors kept in a plastic chamber and exposed to a continuous flow of a certified pre-mixed calibration gas containing 10 ppm CH_4 in dry air (supplied by Praxair Inc.). The experiments were conducted at constant relative humidity (RH). Figure 13a shows that the relative resistance ($\Delta R/R = (R_{methane} - R_{air})/R_{air}$) of the ZnO-MWCNT sensors (5 min O_2 plasma-treatment and ZnO ALD at 175 °C) increases monotonically while being exposed to 10 ppm CH_4 in dry air at a constant flow rate (0.94 L/min), and reproducibly returns back to the original levels when purging the test chamber with N_2. No response to CH_4 was observed for sensors fabricated with non-functionalized MWCNTs (Figure 13b) corroborating our hypothesis that the change in resistance was caused by the transfer of electrons from the MWCNT surface to the intermediate complex generated by the ZnO nanoparticles and CH_4 molecules.

No change in resistance was observed in non-pretreated but functionalized MWCNTs, indicating that the surface pre-treatment was an important component of CNT functionalization. The best relative resistance change for the ZnO-MWCNT sensors at 10 ppm CH_4 in dry air was 12.1 % on an average with a standard deviation of 2.11 %.

No reversible change in resistance was observed in O_2 plasma pretreated but *not ZnO functionalized* MWCNTs (Figure 14a) and UVO pretreated but *not ZnO functionalized* MWCNTs (Figure 14b) indicating that the ZnO functionalization is *essential* for the reversible resistance change of the chemoresistor sensor in presence and absence of 10 ppm CH_4 in air.

Synthetic air was also used to recover the ZnO-MWCNT sensor back to baseline (Figure 15). The synthetic air mixture, supplied by Praxair Inc.was a specific synthesis of N_2 (79.19 %) and O_2 (20.81 %). No other gas elements such as CO_2 and other hydrocarbons, common in natural air, were present in the synthetic gas. The same synthetic air was used as the balance gas to prepare the 10 ppm CH_4 in air mixture. The resistance of the ZnO-MWCNT sensor increased monotonically while it was exposed to the 10 ppm of CH_4 in synthetic air. The flow rate was 2 SCFH with a residence time of 4.5 mins inside the test chamber. The sensor was recovered by synthetic air keeping the same flow rate. The sensor resistance went back to its base level as a result of recovery by the synthetic air. The RH during the test was low, 1 to 2 %.

Based on the data in Figure 16 the limit of detection is less than 2 ppm CH_4 .

ZnO functionalized CNT based chemoresistor sensors are sensitive to CO (63) and NO_2 (64). H_2O, O_2, and H_2 are also possible interfering gases (65). In particular, understanding the effect of relative humidity (RH) is important to estimate the outdoor performance of microfabricated

gas sensors. To gauge the effect of relative humidity (RH) on sensor performance, the change in the baseline relative resistance of the surface pre-treated ZnO-MWCNT sensors was measured at room temperature due to a change in RH. Humidity was provided by a controlled flow of moist air (flow rate 0.94 L/min) into a plastic test chamber (residence time 4.5 mins). The baseline relative resistance of the sensor increased as the RH was increased from 10% to 91% and returned back to the original baseline once the RH was reduced back to 10 %. This suggests a strong electron transfer between the ZnO-MWCNTs and water molecules (Figure 17a). Thus it was essential to control the humidity inside the test chamber while exploring CH_4 sensitivity.

To decouple the sensor response to CH_4 from the interference of variable RH during the tests, the RH inside the test chamber was kept constant during each test period. A stream of dry N_2 was introduced first to bring the test chamber RH to a low level (approximately 5%), then 10 ppm CH_4 in dry air was introduced at the same flow rate keeping the RH inside the test chamber constant (Figure 17b).

3.4 Summary

The chapter presented (a) a lift-off based photolithography technique to fabricate interdigitated metal electrodes, (b) a drop deposition based technique to disperse MWCNTs onto the electrode surface, and (c) an ALD process to functionalize the surface preactivated MWCNTs with ZnO NCs. The morphology, chemical composition, and crystal quality of the functionalizing ZnO NC were characterized by using SEM, EDX, Raman, and TEM. The crystalline quality and dimensions of the functionalizing ZnO NCs were strongly dependent on the ALD temperature. The ZnO-MWCNT chemoresistor sensor was able to detect low parts per million

CH_4 in dry air at room temperature. The best response, so far, was observed with an O_2 plasma pretreated MWCNTs with ZnO deposition at 175 ° C.

Future plans include exposing the ZnO-MWCNT sensor to CO_2, H_2, and O_2 to map the response to these interfering gases.

TABLE III: Resistances of MWCNT sensors before and after the ZnO was deposited by the ALD.

Sensor#	1	2	3	4	5	6
Before ZnO Deposition (Ω)	468.8	1.67 K	445	585.6	563.9	147 K
After ZnO deposition (Ω)	414.8	1.68 K	394.7	515.1	555	141 K

TABLE IV: Frequency shift originating from different ZnO Raman modes for ZnO nanoparticles deposited at different ALD temperatures on the MWCNTs.

ALD temperature (°C)	$E_2{}^{high} - E_2{}^{low}$ peak position (cm^{-1})	$E_2{}^{high}$ peak position (cm^{-1})	$A_1(LO)$ peak position (cm^{-1})
175	Mostly absent	430.78 - 431.5 (weak)	568.84 - 574.86 (weak)
200	329.44	424 - 429.13	564.82 - 571.55
220	320.79 - 327.71	430.84 - 435.97	566.51 - 574.92

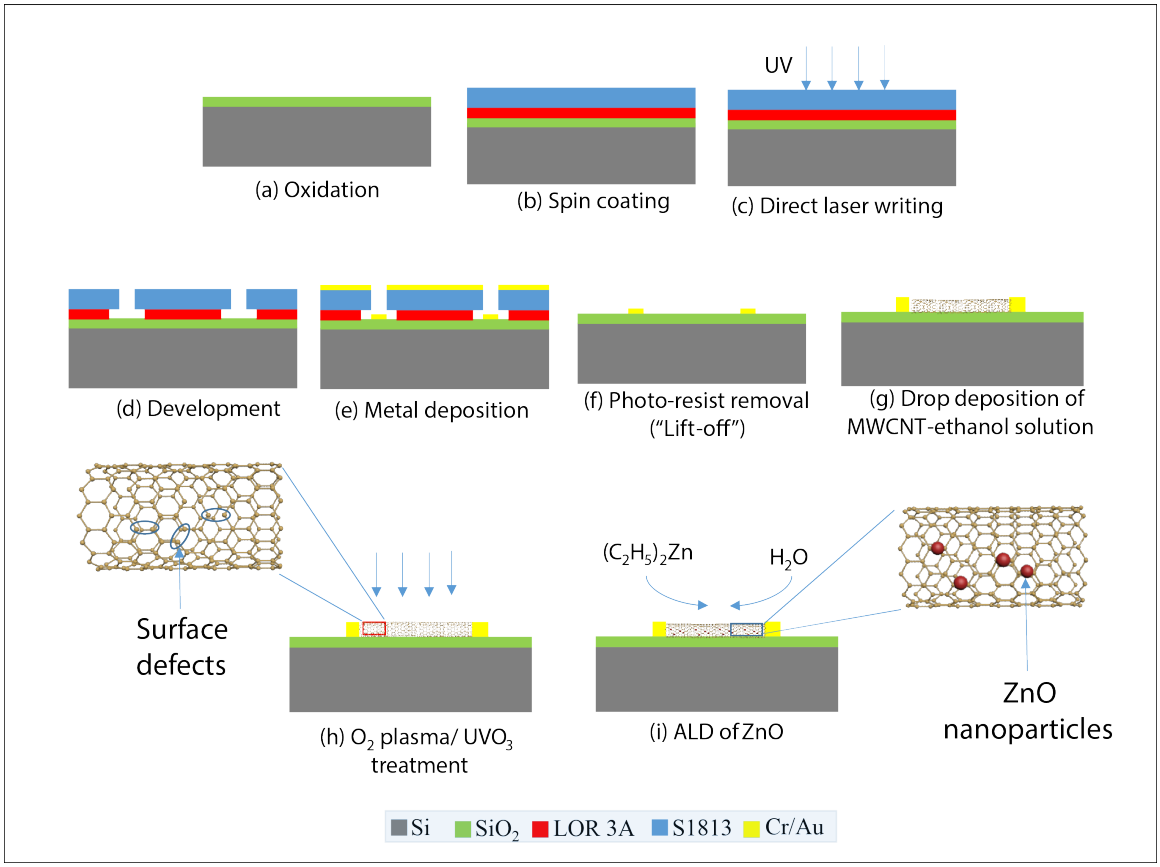

Figure 4: Schematic of the fabrication process of surface pretreated ZnO functionalized MWCNT methane sensor.

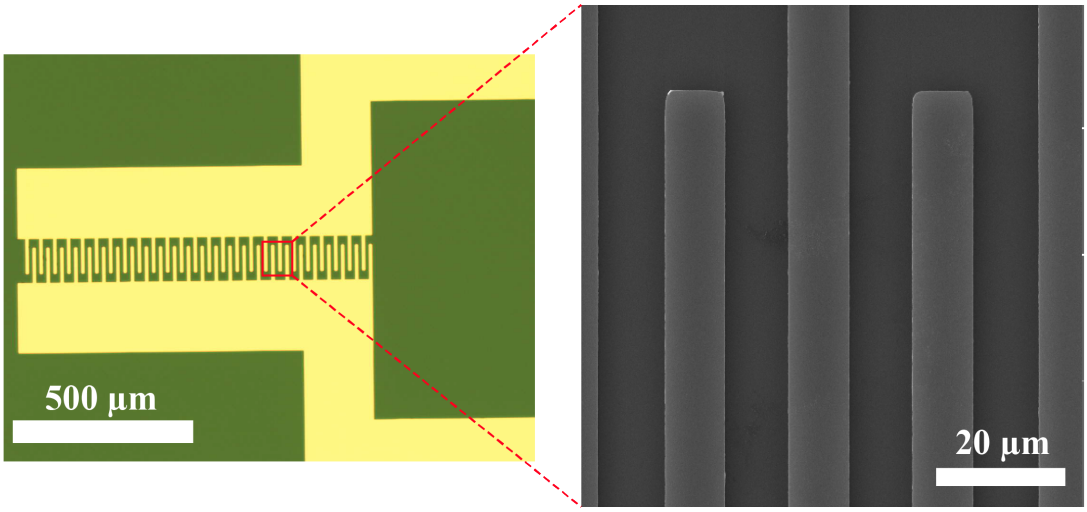

Figure 5: (a) Optical microscopy image of photolithography based microfabricated interdigitated Au electrodes. (b) SEM image magnifying the same electrodes.

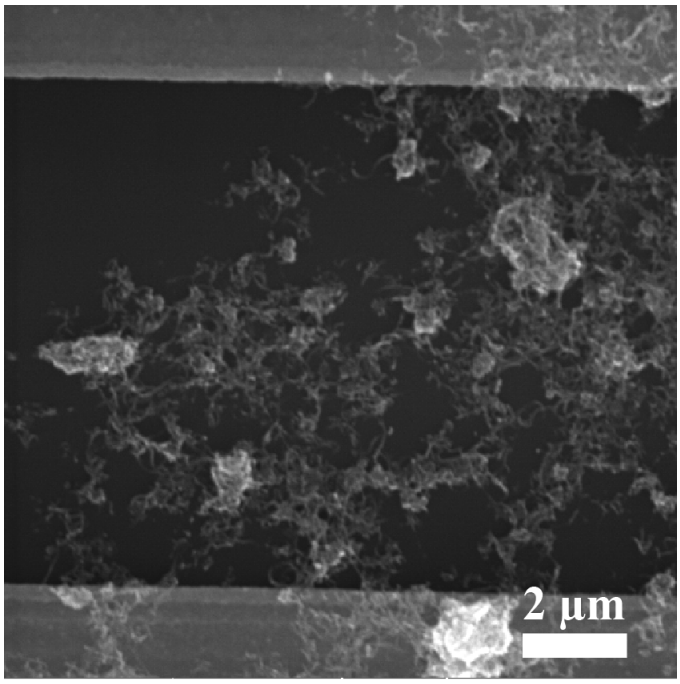

Figure 6: SEM image of MWCNT mesh confined between two Au electrodes.

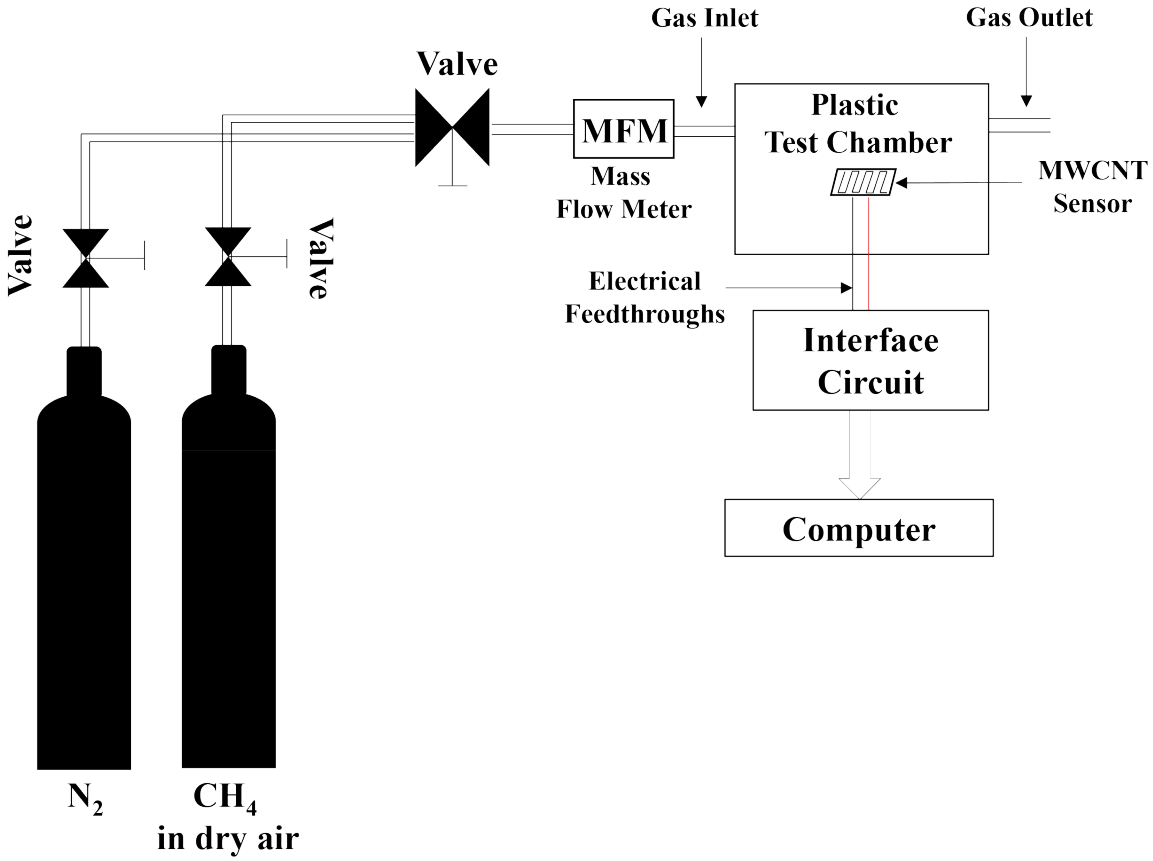

Figure 7: Schematic of the experimental system used to test the ZnO–MWCNT sensor with CH_4 in dry air. N_2 was used to flush the test chamber so the sensors could recover after each cycle of exposure to the CH_4 in dry air mixture.

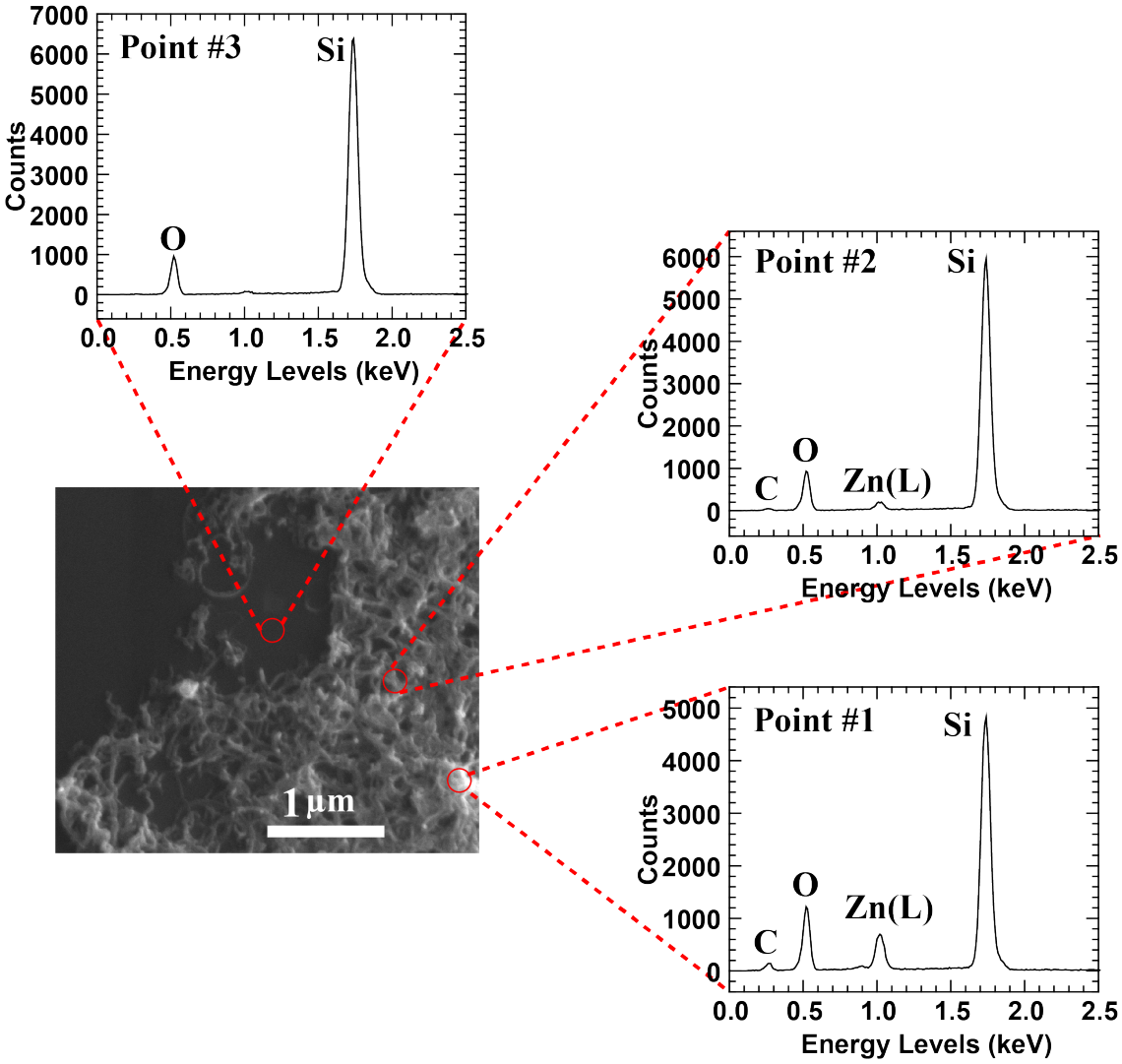

Figure 8: SEM and EDX results obtained from a UVO treated ZnO–MWCNT sample fabricated by ALD at 220 °C. The strong peak of the L-line of Zn was only found on the MWCNT (brighter point 1). The relatively weaker peak of Zn was found on the less bright point 2. Point 3, which was on the SiO_2 substrate, did not show a Zn signal.

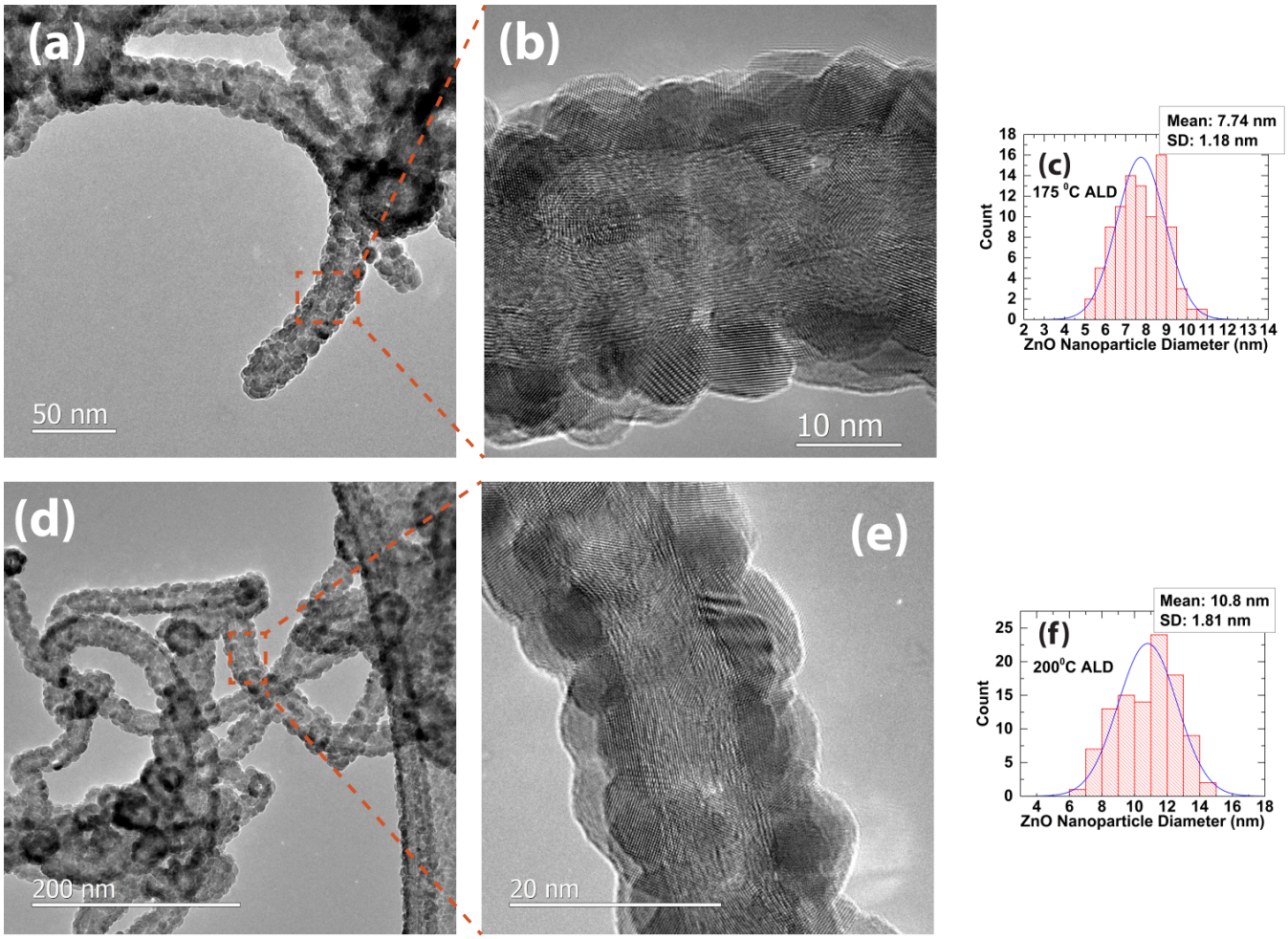

Figure 9: (a) TEM images of ZnO-MWCNT fabricated at 175 °C ALD temperature. (b) High resolution TEM (HRTEM) micrograph of 175 °C ALD ZnO-MWCNT sample showing the high crystal quality of the deposited ZnO NCs on the surface pre-activated MWCNT with clearly visible lattice fringes. (c) Size distribution of the 175 °C ALD ZnO NCs showing that the mean diameter of the functonalizing ZnO was 7.74 nm. (d) TEM images of ZnO-MWCNTs fabricated at 200 °C ALD temperature. (e) HRTEM micrograph of 200 °C ALD ZnO-MWCNT sample showing the high crystal quality of the deposited ZnO NCs on the surface pre-activated MWCNT. (f) Size distribution of the 200 °C ALD ZnO NCs showing that the mean diameter increased to 10.8 nm.

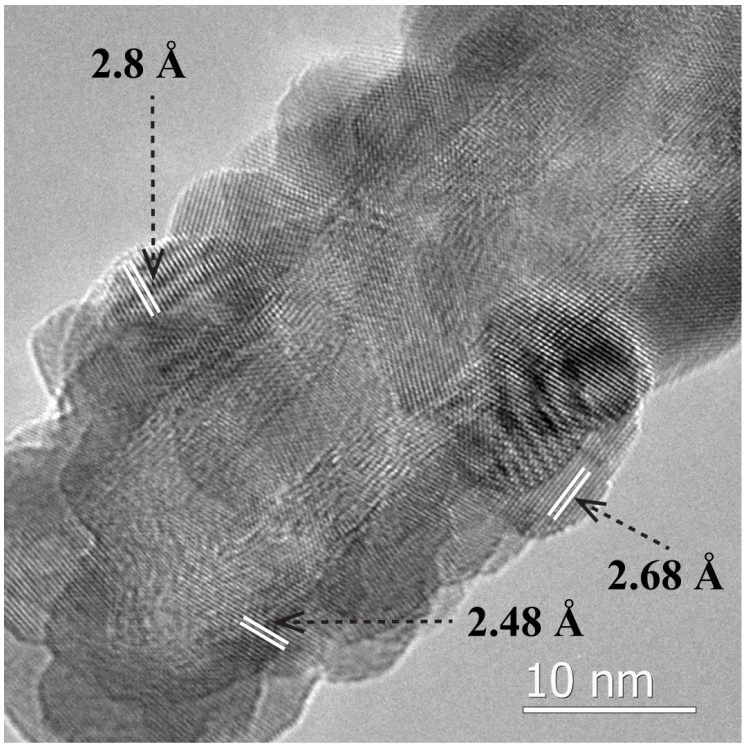

Figure 10: HRTEM image of a ZnO–MWCNT (ALD at 175 ^{0}C) sample showing interplanar spacing of 2.8 Å, 2.68 Å, and 2.48 Å corresponding to $< 100 >, < 002 >$, and $< 101 >$ planes of ZnO.

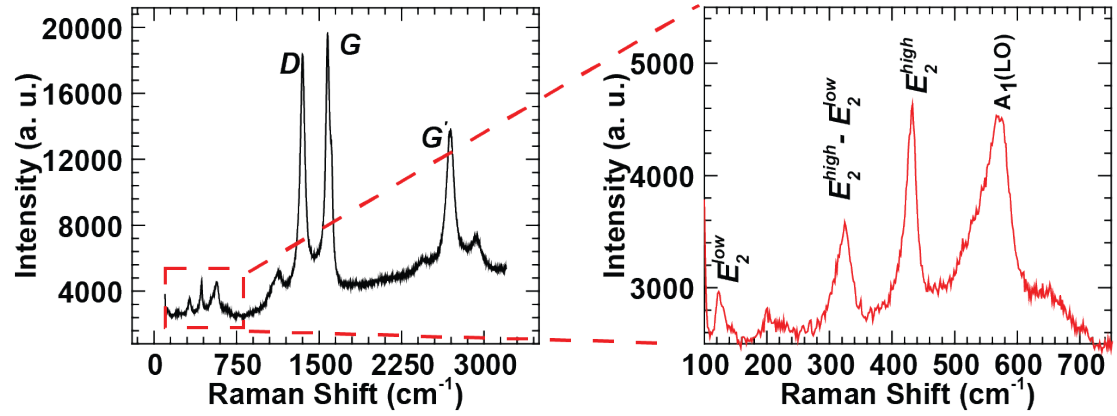

(a) 220 ^{0}C ALD

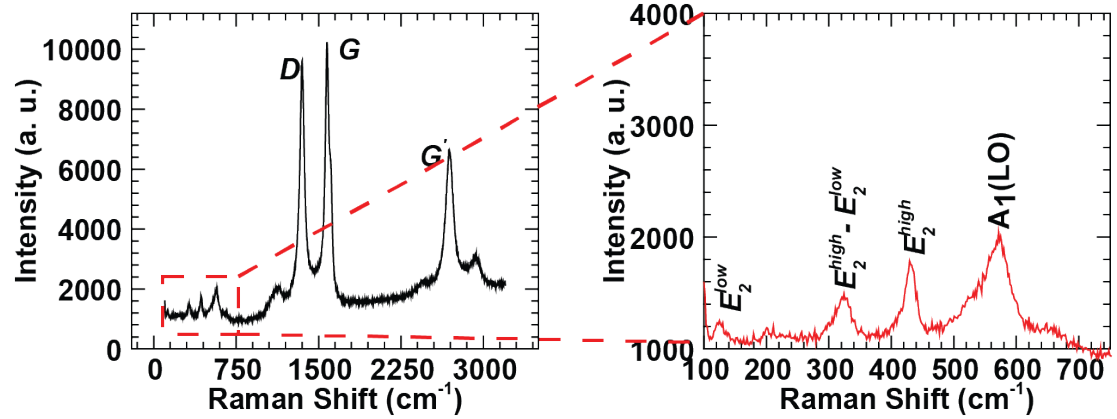

(b) 200 ^{0}C ALD

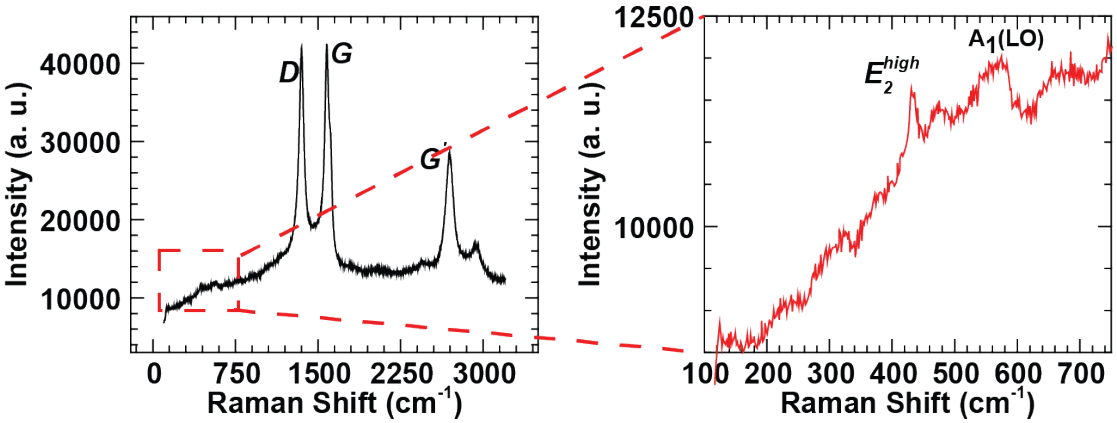

(c) 175 ^{0}C ALD

Figure 11: Raman spectra obtained from the ZnO-MWCNT samples at ALD temperatures of (a) 220 °C, (b) 200 °C, and (c) 175 °C. The peaks at 200.6, 429.13, 572.2, and 329.44 cm^{-1} correspond to $2E_2{}^{low}$, $E_2{}^{high}$, $A_1(LO)$, $E_2{}^{high} - E_2{}^{low}$ low modes of ZnO, respectively.

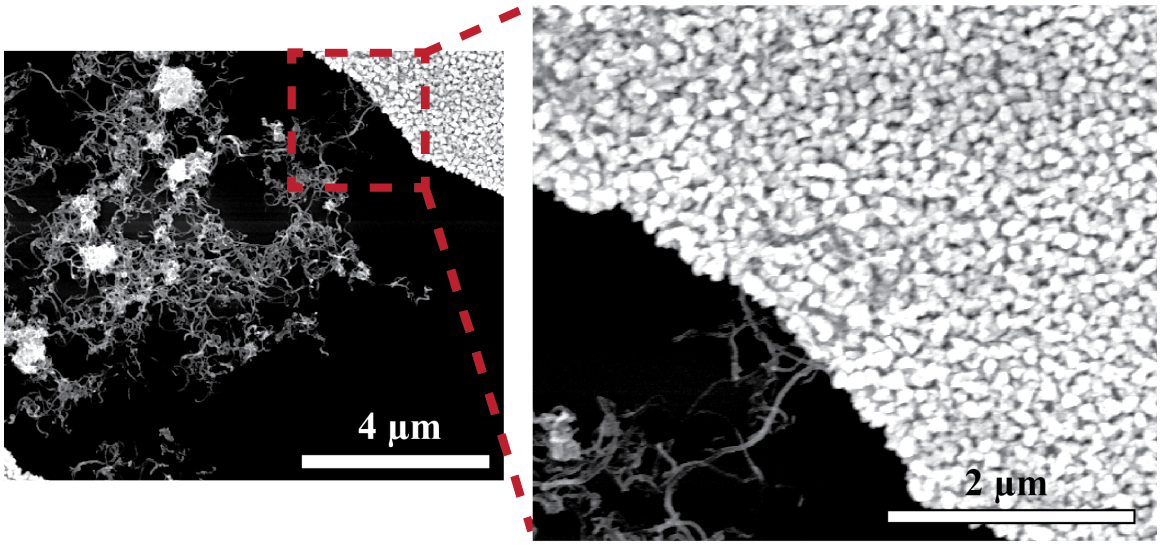

Figure 12: SEM images of a ZnO–MWCNT sensor with the ALD temperature at 220 °C. Inset shows the change in texture of the interdigitated Au electrodes due to the high (220 °C) temperature during the ALD process.

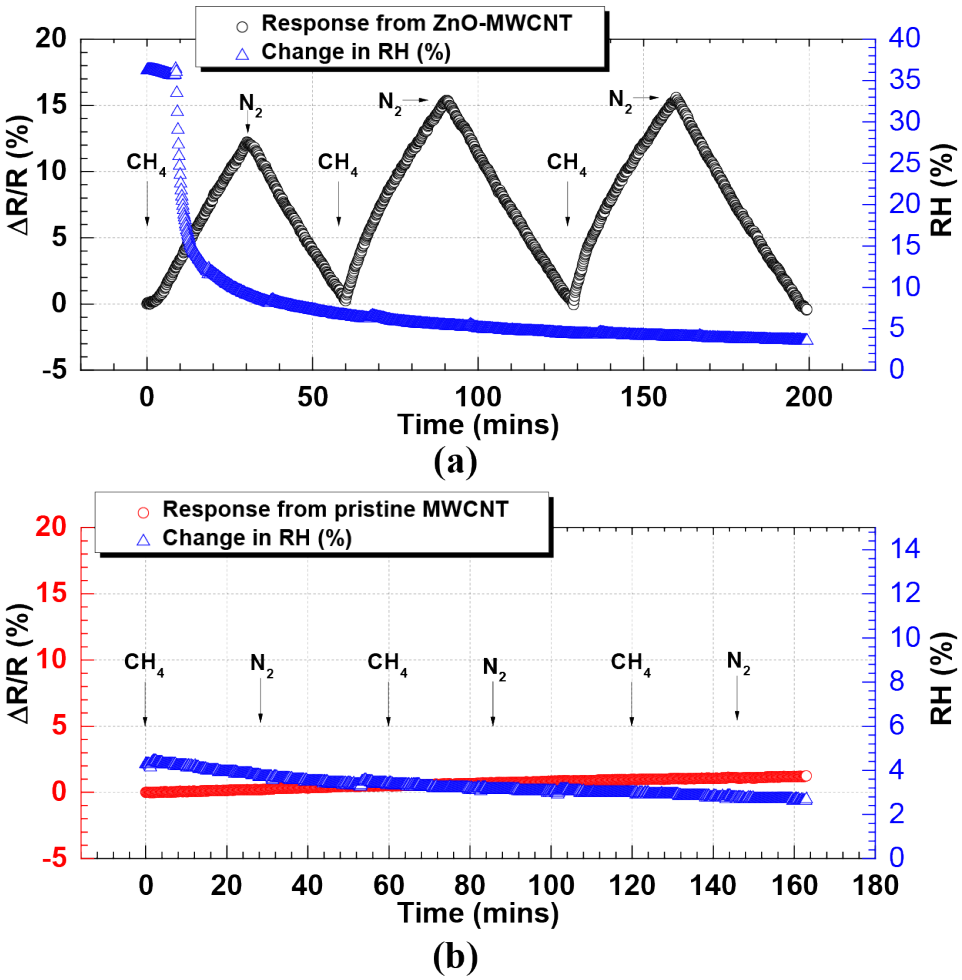

Figure 13: (a) Relative resistance change of the ZnO–MWCNT (5 min O_2 plasma pretreated) sensor while subjected to alternating exposure of 10 ppm CH_4 in dry air and N_2. (b) Relative resistance change of the pristine MWCNTs while subjected to repetitive exposure of 10 ppm CH_4 in dry air and N_2. Right hand y-axes in both plots show change in RH (%) inside the test chamber during the tests.

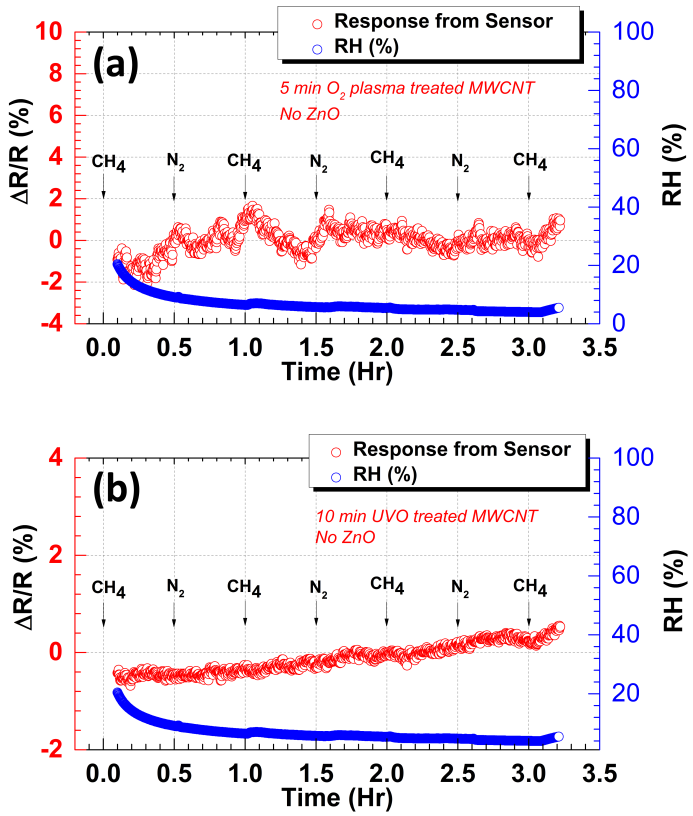

Figure 14: (a) Relative resistance change of the 5 min O_2 plasma pretreated but *not-ZnO functionalized* MWCNT sensor while subjected to alternating exposure of 10 ppm CH_4 in dry air and N_2. (b) Relative resistance change of the 10 min UVO pretreated but *not-ZnO functionalized* MWCNT sensor while subjected to alternating exposure of 10 ppm CH_4 in dry air and N_2. Right hand y-axes in both plots show change in RH (%) inside the test chamber during the tests. The RH inside the test chamber was kept constant at 5%.

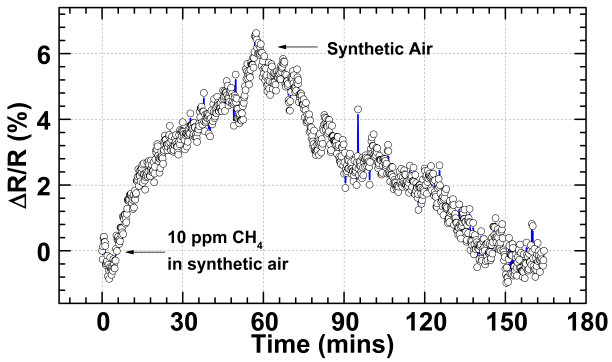

Figure 15: Relative resistance change of the ZnO–MWCNT (5 min O_2 plasma pretreated) sensor exposed to 10 ppm CH_4 in synthetic air and recovered by synthetic air. The RH inside the test chamber was kept constant at 1–2%.

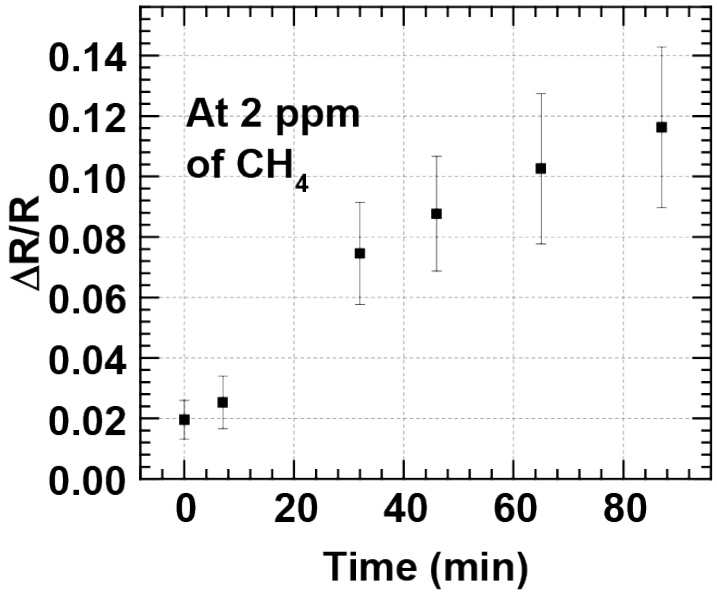

Figure 16: Relative resistance change of the ZnO-MWCNT sensor while exposed to 2 ppm concentration of CH_4 in air.

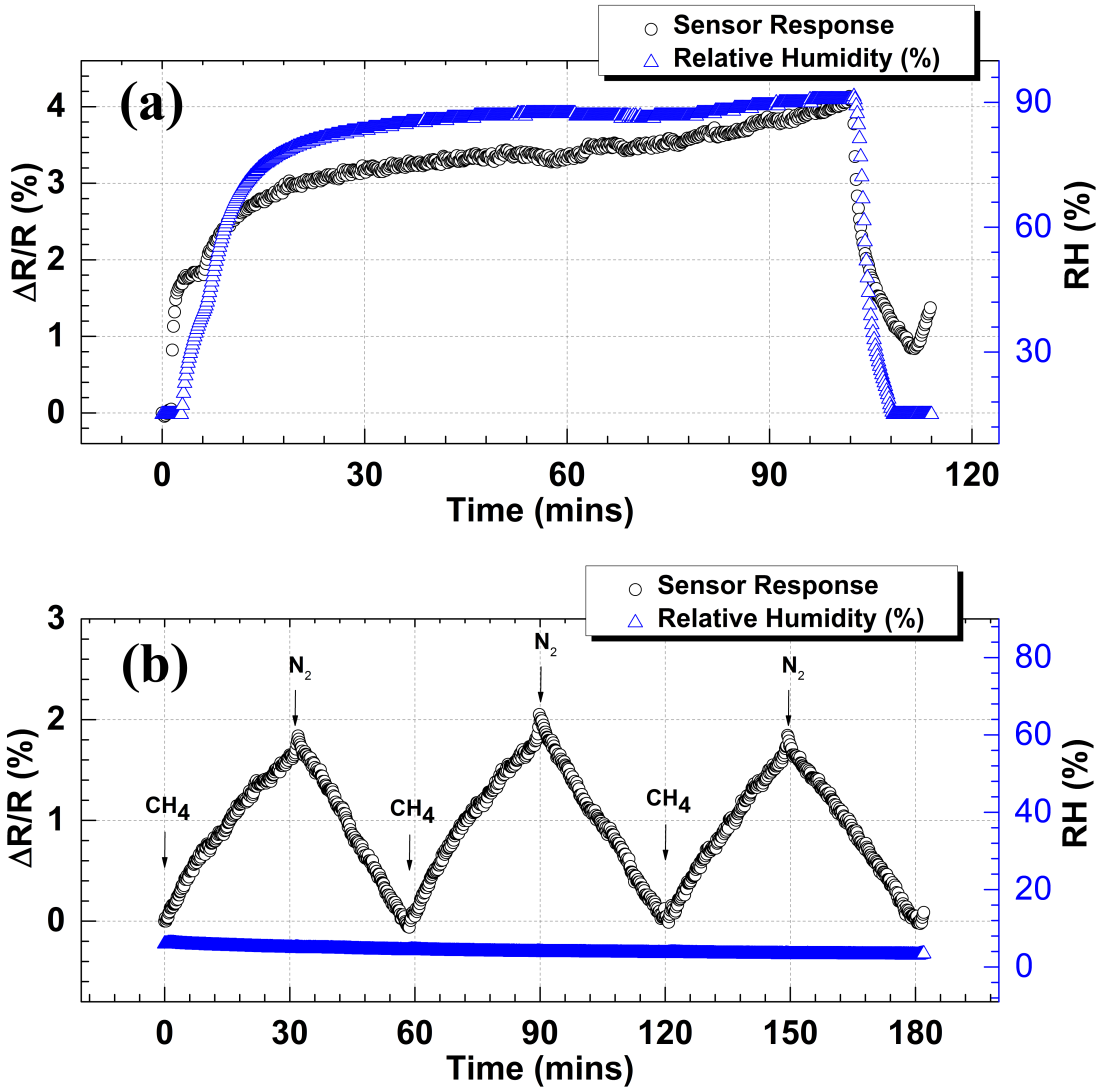

Figure 17: (a) Relative resistance change ($\Delta R/R = (R_{RH} - R_{air})/R_{air}$) of the ZnO-MWCNT sensor while the relative humidity inside the chamber was varied by a controlled flow of moist air, (b) Relative resistance change ($\Delta R/R = (R_{methane} - R_{air})/R_{air}$) of the ZnO-MWCNT (UVO pre-activated) sensor while exposed to iterative cycles of 10 ppm CH_4 or N_2. The RH inside the test chamber was kept constant at 5%.

CHAPTER 4

TIN OXIDE NANOCRYSTALS FUNCTIONALIZED MWCNT METHANE SENSORS

(A major portion of the chapter was previously published as: "Novel chemoresistive CH_4 sensor with 10 ppm sensitivity based on multi-walled carbon nanotubes (MWCNTs) functionalized with SnO_2 nanocrystals.", Md Humayun, R. Divan, Y. Liu, L. Gundel, P. A. Solomon, and I. Paprotny, J. Vac. Sci. Technol. A 34, 01A131 (2016))

Chemoresistive sensors based on MWCNTs functionalized with SnO_2 nanocrystals have great potential for detecting trace gases at low concentrations (single ppm levels) at room temperature. The SnO_2 nanocrystals act as active sites for the chemisorption of gas molecules, and CNTs act as an excellent current carrying platform, allowing the adsorption of gas on SnO_2 to modulate the resistance of the CNTs. However, uniform conjugation of SnO_2 NCs with MWCNTs is challenging. An effective atomic layer deposition (ALD) approach to functionalize the surface of MWCNTs with SnO_2 NCs is described in this chapter. SEM, TEM, EDX, and Raman spectroscopy were used to study the morphology, elemental composition, and the crystal quality of SnO_2 functionalized MWCNTs. High resolution transmission electron microscope (HRTEM) images showed that the crystal of the functionalizing SnO_2 NCs was of high quality with clear lattice fringes and dimensions almost 3 times smaller than previously described in literature. A lift-off based photolithography technique with bi-layer photoresists was optimized to fabricate SnO_2 functionalized MWCNTs chemoresistor sensors, which at room temperature

can reliably detect below 10 ppm CH_4 in air. Such strong response, with significant reversible relative resistance change is believed to be the direct result of the successful functionalization of the MWCNT surface by SnO_2 NCs.

Semiconductive SnO_2 is widely used in gas sensing metal oxide sensors (16; 66; 48; 67; 68). However, the use of bare SnO_2 as a gas sensor is limited by the requirement for continuous heating to initiate the surface chemisorption of O_2; a pre-requisite for the SnO_2 to react with the target gas species (16; 66; 48; 67; 68). As mentioned in earlier chapters, the surface of bare CNTs is non-reactive to many gas molecules, and in order to obtain selective gas sensing, it is necessary to functionalize the surfaces of the CNTs, i.e, embedding them with active sites, by controlled deposition of appropriate nano-materials (27; 28; 31; 32; 33). Thus the nano-scale integration of SnO_2 and CNTs provides a unique approach to building sensitive (<ppm) and selective chemoresistor gas sensors that do not require external heat to operate, making this conjugate a more effective gas sensing element than either of its constituents.

To confirm significant reversible relative resistance change at low level of the species of interest, it is necessary that the deposited SnO_2 NCs uniformly cover the surface of the MWCNTs. Most of the reported SnO_2-CNT nano-hybrids are synthesized chemically, where uniform coverage of the discrete NCs and their crystal quality cannot be precisely controlled (69; 70; 71). To facilitate the control of the deposition of nano-meter thick SnO_2 NCs on the surface of MWCNT, we developed a site-specific ALD functionalization process. To enhance the integration of the SnO_2 NCs with the MWCNTs, the surfaces of the MWCNTs were pre-treated using a UVO activation method.

Our highly-sensitive SnO_2-MWCNTs CH_4 sensor has the following important attributes: (a) the ALD technique we used ensures uniform coverage of SnO_2 NCs on the MWCNT surface (72; 73), (b) the UVO surface pre-treatment creates defects for nucleation sites on the MWCNTs ensuring strong bonding between SnO_2 and MWCNT, as well as high quality of the deposited SnO_2 NCs (44), (c) the work function is closer between SnO_2 and MWCNTs hence a low Schottky barrier at their junction compared to the Schottky barrier between previously reported Pd and MWCNT (28), and (d) SnO_2 is also less expensive than other functionalization materials used in reported CNT-based CH_4 chemoresistor sensors (28).

The remainder of this chapter is structured as follows: Section 4.1 describes the fabrication and SnO_2 functionalization of the MWCNT methane sensors and their characterization. The experimental setup for methane exposure tests is described in Section 4.2. Section 4.3 describes the experimental results, including the resistance change down to 10 ppm CH_4 at room temperature. Finally, concluding remarks are offered in Section 6.3.

4.1 Fabrication

A 1 μm thick SiO_2 layer was grown on Si (100) wafers using wet oxidation at 1100 °C for 3 hours. Following the growth of the oxide layer, a set of interdigitated gold (Cr/Au) electrodes was fabricated on the SiO_2-coated Si wafer using a lift-off based photolithography technique. Gaps between the interdigitated electrodes ranged from 5 μm to 10 μm.

A batch of 98% pure MWCNTs with 12 nm average diameter, 10 μm average lengths, and a specific surface area of 220 m^2/g was purchased (Sigma Aldrich). 1 mg MWCNTs in 50 mL of ethanol was sonicated and used to produce a well dispersed MWCNT slurry. Using a

micro-syringe, a 50 μL aliquot was deposited on a 1 mm^2 active area of the fabricated metal electrodes, which was followed by baking at 75 °C for 1 min to remove the solvent and to improve adhesion.

The deposited MWCNTs were treated with UVO inside a UVO chamber (Nanomax Ultra-100), for 15 min to 20 min. ALD was used to integrate SnO_2 NCs with UVO pre-treated MWCNTs. The growth was done employing an Ultratech Savannah S200 ALD system. The tetrakis(dimethylamino) tin(IV) pre-cursor was heated to 55 °C and delivered under its own vapor pressure in a 1 s pulse, followed by a 15 s purge, a 0.1 s water dose, and another 15 s purge. This process was repeated for 175 cycles at a growth temperature of 175 °C (74). ALD resulted in a deposition of SnO_2 NCs with an average diameter of 3.36 nm which was confirmed by TEM.

The electrical conductivity of the fabricated electrodes, the CNT-deposited resistive network, and ALD-functionalized MWCNTs devices was measured using a digital multimeter (Fluke 115). Parasitic and contact resistance was on the order of single ohms and considered insignificant compared to the resistance of the chemoresistor (1 KΩ to 100 KΩ).

The MWCNTs functionalized with SnO_2 NCs were characterized in several approaches. SEM (Raith 150) was used to characterize their morphology. The elemental composition of SnO_2-MWCNT samples was characterized using EDX (Nova 600 Nanolab Dualbeam SEM/FIB). A micro-Raman system (Renishaw Invia) was used to perform Raman spectroscopy (a green laser at 514 nm) on the SnO_2-MWCNT samples at room temperature. The atomic scale morphology and crystal quality were assessed with a TEM (JEOL 2100F) at 200 kV.

4.2 Experimental setup

SnO_2-MWCNT sensors were evaluated in a test chamber (1.43 L) connected with inlets and outlets for gases and an inlet for the electrical feedthroughs. The residence time of the chamber was 4.5 min at a flow rate of 0.94 L/min. Relative humidity (RH) and temperature inside the test chamber were continuously monitored and recorded by a data-logger (HOBO U-10 series). Electrical signals generated from the sensors were recorded by a computer with a custom interface circuit and an analog-to-digital converter. A mixture of 10 ppm methane in dry air (Praxair Inc., N_2 79.19 % and O_2 20.81 %) was introduced to the chamber at a constant flow rate (0.94 L/min) and monitored by a rotameter for 30 min. The RH inside the test chamber was kept constant, confirmed by the HOBO. Dry N_2 was used to purge CH_4 from the chamber resulting in the response of the device back to the baseline resistance after each cycle of CH_4 exposure.

To study the interference of water vapor on sensor performance the relative resistance change of the sensor was monitored while the RH in the chamber was maintained above 80 % for almost 24 hours. After this period the RH was reduced back approximately to 10 % by flowing dry air through the test chamber for almost 4 hours.

To understand the response of the sensor to CH_4 at relatively higher RH, 10 ppm of CH_4 was passed through a water bubbler at a constant flow rate (0.94 L/min) to maintain RH inside the chamber at about 70 %. After the CH_4 cycle, dry N_2 was allowed to flow through the water bubbler at the same flow rate to recover the sensor to its original response. Note: there was an abrupt change in RH level (approximately 2 %) when N_2 was added.

4.3 Results and discussion

For the MWCNT network to function as a chemoresistor, the ALD-deposited SnO_2 cannot create a direct conductive pathway between the electrodes outside the MWCNT mesh, i.e., the sensor electrodes are only connected via the MWCNTs and not the SnO_2. This was confirmed with electrical testing and the resistance depended on the structure of the interdigitated metal electrodes and the density of the deposited MWCNTs in the ethanol solution. The resistance of the MWCNT-connected electrodes varied between 1 KΩ to 100 KΩ, while the resistance outside of the MWCNT mesh was found to be infinite.

SEM images confirmed that the functionalized MWCNTs were in proper contact with the interdigitated Au metal pads (Figure 18). SEM and EDX results indicated that the SnO_2 NCs were present on the MWCNT surface, confirmed by the more intense Sn signal, as indicated by the brighter regions in Figure 19 (points 3, 4 and 5). The TEM micrograph shows discrete SnO_2 NCs uniformly covering the surface of the pre-treated MWCNT surface (Figure 20a). The inset shows the size distribution of the ALD deposited SnO_2 NCs on the MWCNT surface. The mean diameter of the "spherical" SnO_2 NCs was about 3.4 nm with a standard deviation of about 0.8 nm. The average SnO_2 NC size was smaller than reported in previous studies (27). The HRTEM image in Figure 20b illustrates the rutile structure of the SnO_2 NC and its good crystalline quality. The interplanar spacing of 3.3 $\mathring{A}$ and 2.6 $\mathring{A}$ corresponds to lattice spacing of rutile SnO_2 from <110> and <101> reflections, respectively (28).

Raman spectra, illustrated in Figure 21, reveal that after the surface pre-treatment and ALD functionalization, the D, G, G' peaks of the MWCNT are preserved, while an additional Raman peak originating from the SnO_2 NCs was also observed.

The D band frequency positions were 1349.56 cm^{-1} and 1350.7 cm^{-1}, respectively, for pristine and SnO_2-MWCNT. The G band frequency position was 1573.74 cm^{-1} and 1577.9 cm^{-1}, respectively, for pristine and SnO_2-MWCNT. Although the D band frequency was almost same for both type of samples, the G band frequency showed an upward shift for the SnO_2-MWCNT. The G-band has been attributed to the tangential mode (TM) C–C stretching vibrations (41). This upward shift of G band frequency (or "stiffening" of the TM) was interpreted as electron transfer from carbon atoms to electron acceptor atoms (such as oxygen atoms) during surface treatment of CNTs (41). The I_D/I_G ratios, where I represents the intensity of the Lorentzian function of the D and G peaks, were 0.81 and 1.02 for pristine and SnO_2 loaded MWCNT, respectively (Figure 21a, b). The D peak generally represents the defect or sp^3 carbon on the curved graphitic sheet. The ratio I_D/I_G allows for an estimate of the presence of a defect on the MWCNT surface (75; 41; 76). The increase in the intensity of the D peak with respect to the G peak may be caused by the presence of reactive sites on the surface of the MWCNTs (41; 76) due to the tube sidewalls are being oxidized as a result of the prolonged interaction with reactive O_3 during UVO treatment (76). The UVO surface treatment may give rise to these reactive sites, which helping to nucleate the SnO_2 nanoparticles, enhancing their uniform distribution on the MWCNT surface.

The characteristic Raman peak with frequency shift of 628.38 cm^{-1} corresponds to A_{1g} mode of SnO_2 (77). The nondegenerate mode A_{1g} vibrates in the plane perpendicular to the c axis (78). This is a normal vibrational mode of bulk SnO_2 that is modified because of nano-scale dimension of SnO_2 particles(78).

The polynomial fitting for the phonon dispersion curve of the A_{1g} mode has been reported as (78):

$$\omega(q) = A + B_1(q\pi) + B_2(q\pi)^2 + B_3(q\pi)^3 + B_4(q\pi)^4 + B_5(q\pi)^5 \tag{4.1}$$

where q is the phonon wave vector, ω is lattice vibrational frequency, and $A = 638.22$ cm^{-1}, $B_1 = -2.81$ cm^{-1}, $B_2 = 6.52$ cm^{-2}, $B_3 = -7.25$ cm^{-3}, $B_4 = 0.27$ cm^{-4}, $B_5 = 0.21$ cm^{-5}.

In infinite crystals, phonons only near the center of the Brillouin zone, with $q = 0$, contribute to the Raman scattering of the incident light. On the other hand, in nano-dimensional crystal, phonons with non-zero q also contribute to the Raman scattering of the incident light. Hence $\omega(q)$ starts shifting from $A = 638.22$ cm^{-1} to lower wave number (78). The observed A_{1g} Raman mode at 628.38 cm^{-1} for the SnO_2 NC is almost 10 cm^{-1} lower in comparison to the A_{1g} peak of 638.22 cm^{-1} for bulk SnO_2 (78; 77). Hence, the Raman behavior of our SnO_2 NCs is consistent with reported studies (78).

Methane exposure experiments were carried out at constant low RH (1.5%). When exposing the SnO_2-MWCNT chemoresistor sensor to 10 ppm of CH_4 in dry air, we observed a reproducible resistance change. Figure 22 shows the positive relative resistance change ($\Delta R/R = (R_{methane} - R_{air})/R_{air}$) of a SnO_2-MWCNT sensor (20 mins UVO treatment and

SnO_2 ALD at 175 ^{0}C) each time it was exposed to 10 ppm of CH_4 in dry air at a constant flow rate (0.94 L/min). The resistance of the sensor repeatedly returned back to its original level when the test chamber was purged with dry N_2 at the end of each CH_4 exposure cycle. No response to CH_4 was observed for sensors fabricated with non-functionalized MWCNTs.

MWCNTs act like a rolled graphene sheet with an electrical property similar to crystalline graphite, with overlapping conduction and valence bands (38). Hence the MWCNT shows a metallic type electrical property. However, the presence of p-type semiconductive MWCNTs has also been reported (38; 28). Lu et al. have shown that when SnO_2-MWCNT comes in contact with an oxidizing gas, such as NO_2, the conductance of the p-type MWCNT increases (28). As electrons are accepted by the oxidizing NO_2 molecules, the depletion region at the junction of the n-type SnO_2 and p-type MWCNT increases. The Fermi energy level (E_F) of p-type MWCNT shifts closer to the valence band. As a result, the electrical conductance of the p-type MWCNT increases. Accordingly, if the SnO_2-MWCNT hybrid structure interacts with reducing CH_4, the electrical conductance of the p-type MWCNT decreases. Results presented here support this hypothesis as:

$$\Delta R/R = (R_{methane} - R_{air})/R_{air} \tag{4.2}$$

The RH interference experiment indicated that the sensor resistance varied with RH inside the test chamber, suggesting electron transport between the H_2O molecules and the SnO_2-MWCNT chemoresistor sensors, i.e., a strong RH response (Figure 23). Since the sensors

responded strongly to a change in RH, caution was taken during the CH_4 experiments to keep the RH inside the test chamber constant (Figure 22).

When exposing the SnO_2-MWCNT chemoresistor sensor to 10 ppm of CH_4 in dry air at the higher RH (approximately 70 %), a similar monotonic resistance increment was observed (Figure 24b) compared to the low RH tests where RH was held constant at a few percent (Figure 24a). The sensor also equilibrated to its original response when the chamber was purged with dry N_2. Compared to lower RH the sensitivity to CH_4 and signal-to-noise ratio was reduced at higher RH, which we believe was a result of adsorbed H_2O molecules on the SnO_2-MWCNT sensor. Although the sensor showed decreased response it was still able to detect 10 ppm CH_4 in air at 70 % RH. A noticeable behavior of the sensor performance was the shorter recovery time of the sensor at lower RH shown in Figure 24a in comparison to the result shown in Figure 22. An improvement in sensor performance with respect to recovery time was observed after almost 2.5 months of extensive use. Similar effects have been reported in the literature. For example, Sayago et al.(62) reported that their CNT H_2 sensors showed significant improvement (response time of the sensor became twice faster one year after fabrication) with regard to response and recovery times as the sensors aged. The improvement was postulated to be due to the introduction of carboxylic functionalities from exposure to oxygen. Further research to study the aging related changes in the chemical composition of the SnO_2-MWCNT nano-hybrids is necessary, and has been reserved for future work.

4.4 Summary

The chapter presents a SnO_2-MWCNT chemoresistor CH_4 sensor that exhibits a reproducible relative resistance change to 10 ppm CH_4 in dry air at room temperature. This is believed to be due to a direct result of: (a) uniform distribution of discrete SnO_2 NCs on the surface of the MWCNTs, (b) strong sensitivity of SnO_2 NCs to CH_4 molecules, and (c) low Schottky barrier at the SnO_2-MWCNT junction. Uniform controlled deposition of discrete SnO_2 NCs on the MWCNT surface was achieved through an optimized ALD process. Various characterization results show that SnO_2 NCs on MWCNT surface have smaller dimensions and better crystal quality in comparison to others previously reported in the literature. Future work will focus on different pre-treatment methods of MWCNT surfaces and their effect on the sensor performance. Ongoing work will investigate the effect of other potential interfering gases.

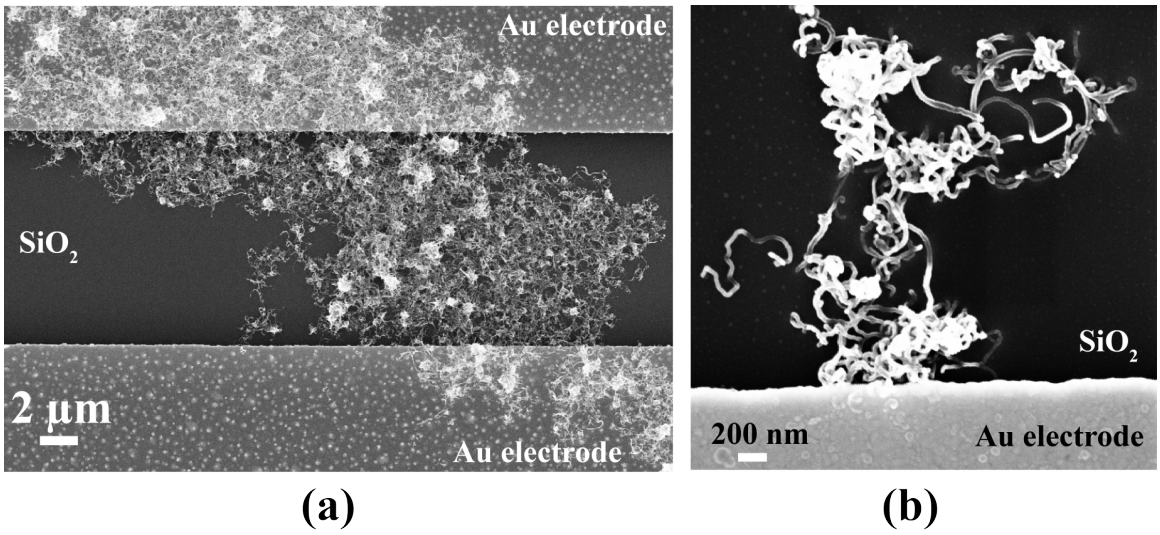

Figure 18: (a) SnO_2-MWCNTs mesh trapped between two fingers of an interdigitated Au electrode network, (b) Higher magnification SEM image focusing on the MWCNT mesh. Brighter surface of the MWCNTs is a result of SnO_2 NCs functionalization.

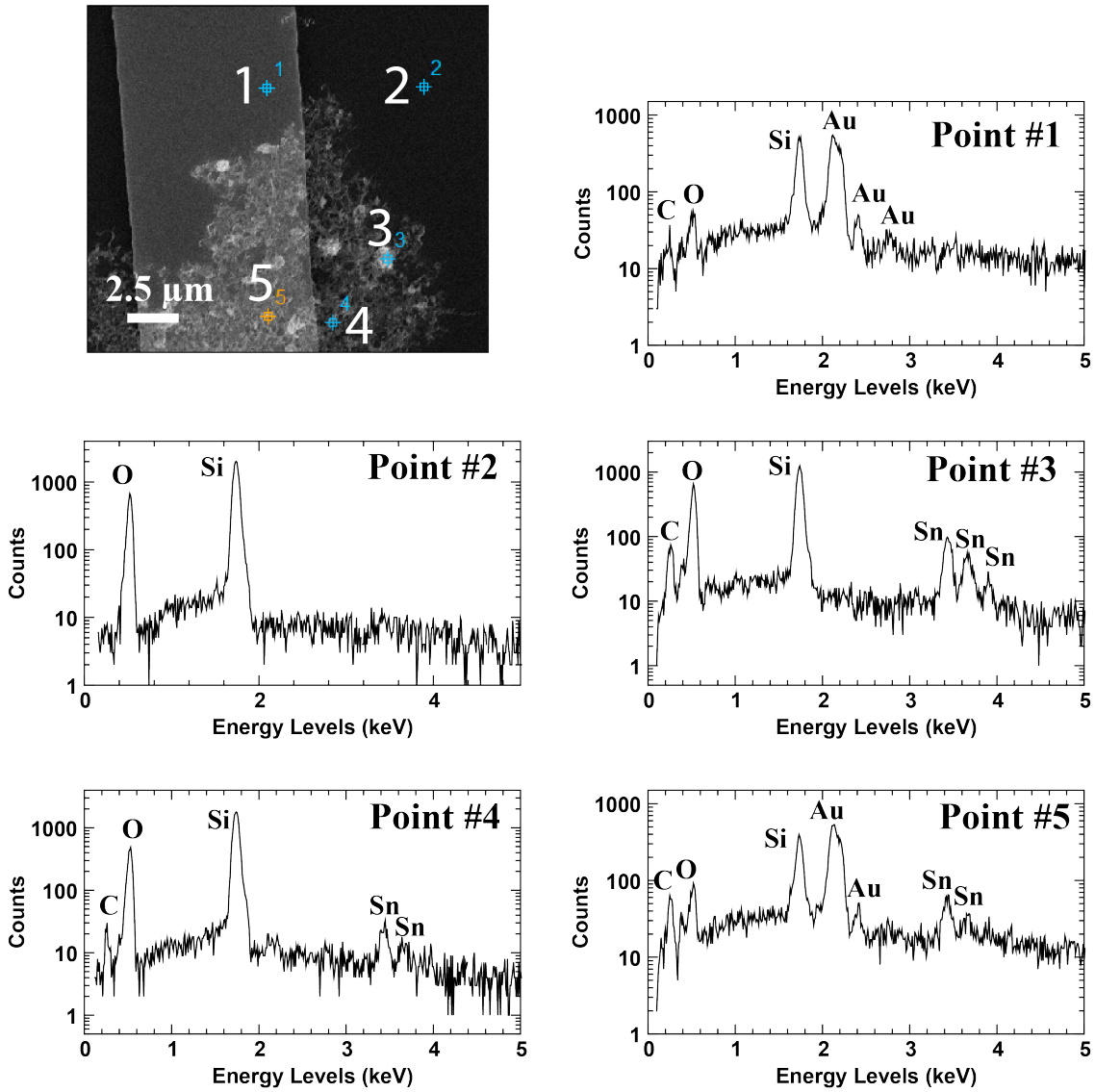

Figure 19: EDX plots obtained from various points on a SnO_2-MWCNT device. Signals of C, Sn, and O originated from points located on the functionalized MWCNT surface. Strength of Sn signal varied according to the brightness of points on the SEM micrograph.

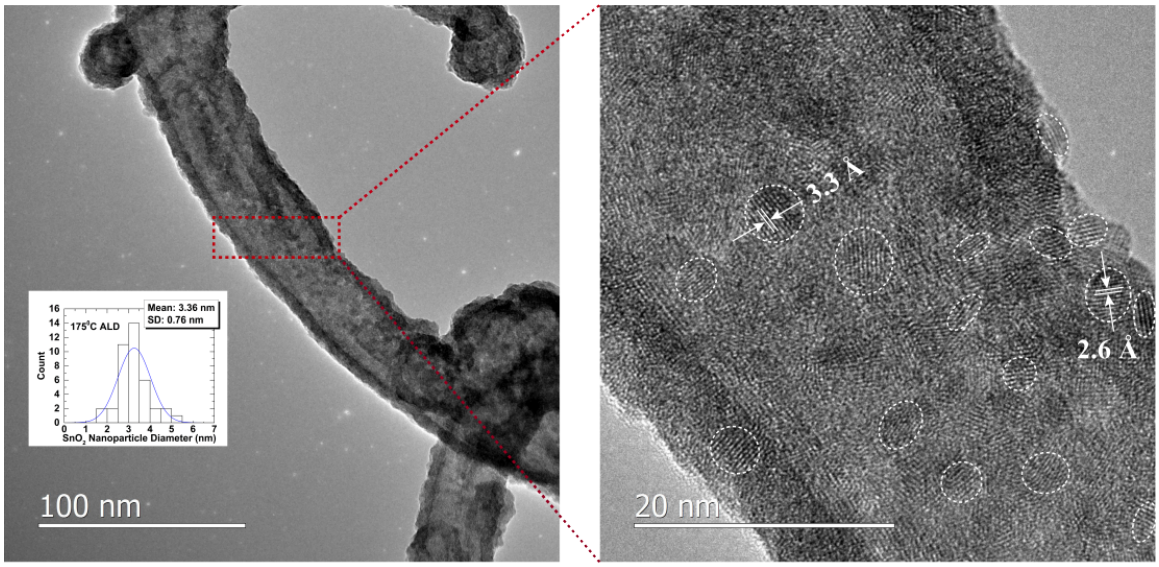

Figure 20: (a) TEM image of a single MWCNT functionalized by SnO_2 nanocrystals. Inset shows the statistical size distribution of functionalizing SnO_2 NCs with a mean diameter of 3.36 nm and a standard deviation of 0.76 nm. (b) HRTEM image showing the lattice fringes originated from SnO_2 NCs. Boundaries of the SnO_2 NCs are marked with white dashed lines in order to guide reader's view. Interplanar spacing of 3.3 $\AA$ and 2.6 $\AA$ correspond to lattice spacing of rutile SnO_2 from <110>, <101> reflections, respectively.

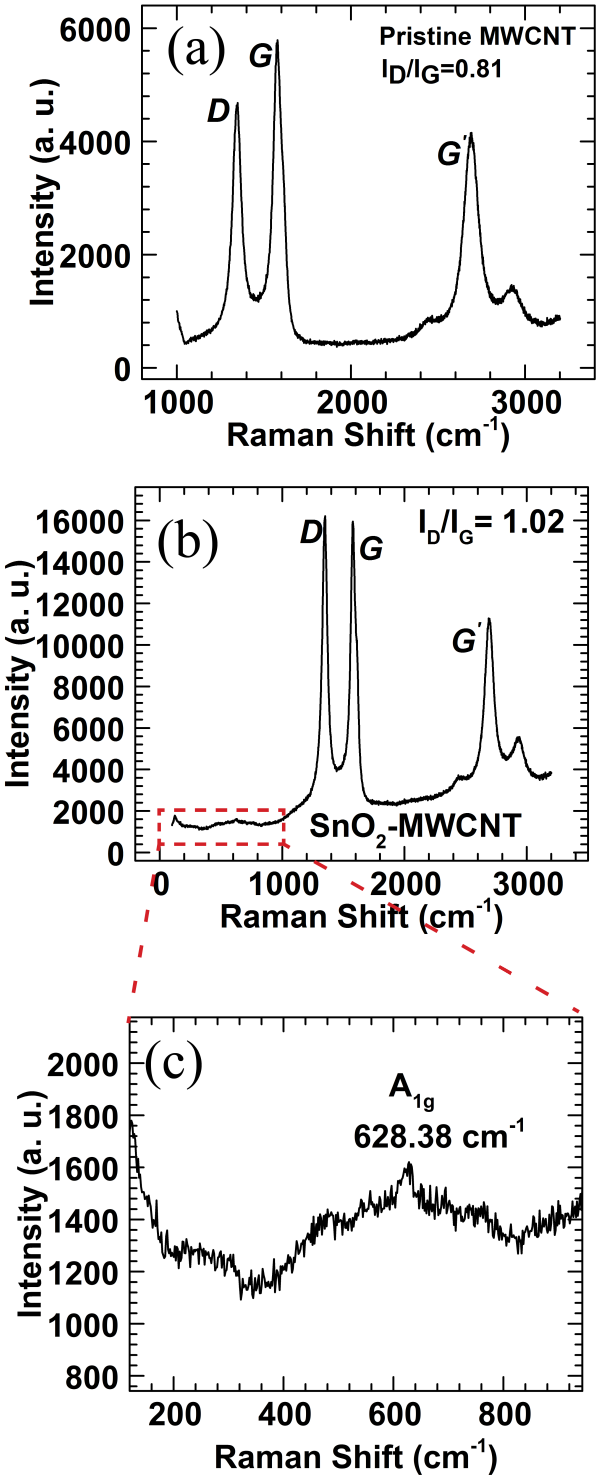

Figure 21: (a) Room temperature Raman spectrum obtained from (a) pristine MWCNT, and (b) SnO_2-MWCNTs while excited by a green laser at a wavelength of 514 nm. (c) Magnified view of the A_{1g} peak of SnO_2.

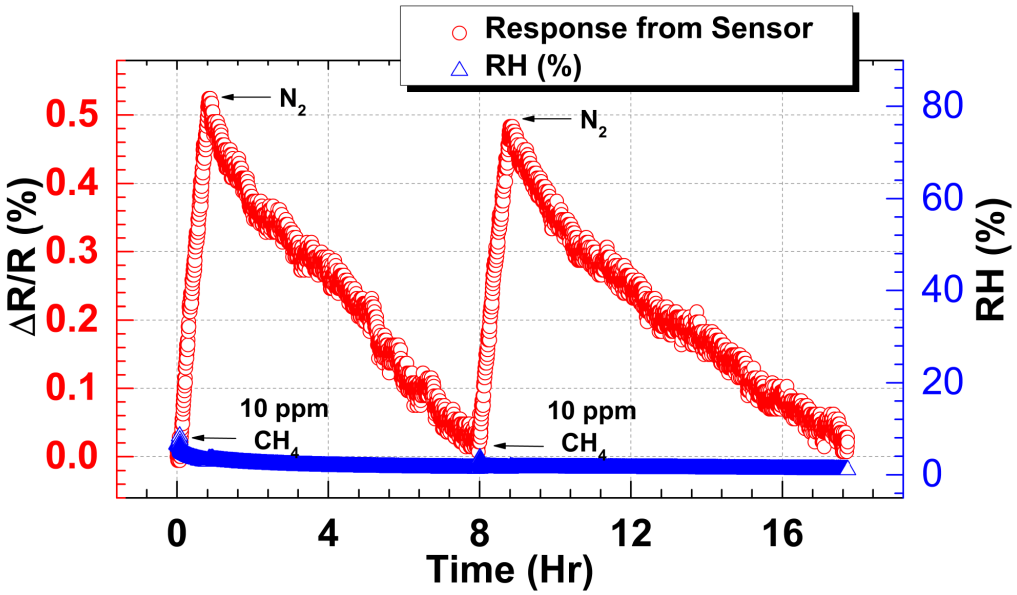

Figure 22: Relative resistance change of the SnO_2-MWCNT chemoresistor sensor while exposed to 10 ppm of CH_4 in dry air and N_2 in an iterative fashion. The circle represents relative resistance change ($\Delta R/R = (R_{methane} - R_{air})/R_{air}$) of the chemoresistor sensor (left hand y-axis) while the triangle represents the RH inside the test chamber recorded by a commercial RH data logger, HOBO (right hand y-axis).

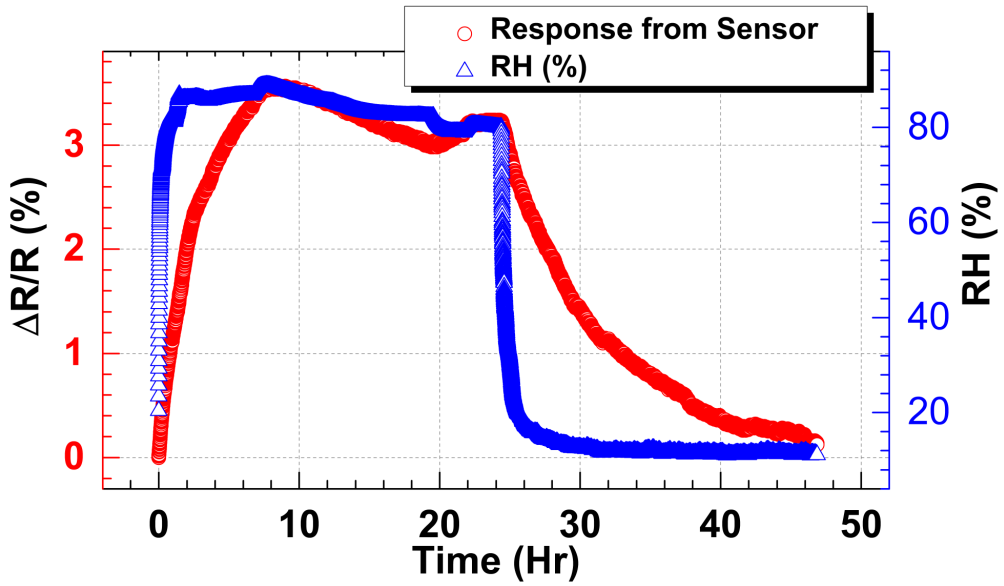

Figure 23: Response from the SnO_2-MWCNT chemoresistor sensor to variation in RH inside the test chamber. The circle represents relative resistance change ($\Delta R/R = (R_{water} - R_{air})/R_{air}$) of the chemoresistor sensor (left hand y-axis) while the triangle represents the RH inside the test chamber recorded by a commercial RH data logger, HOBO (right hand y-axis).

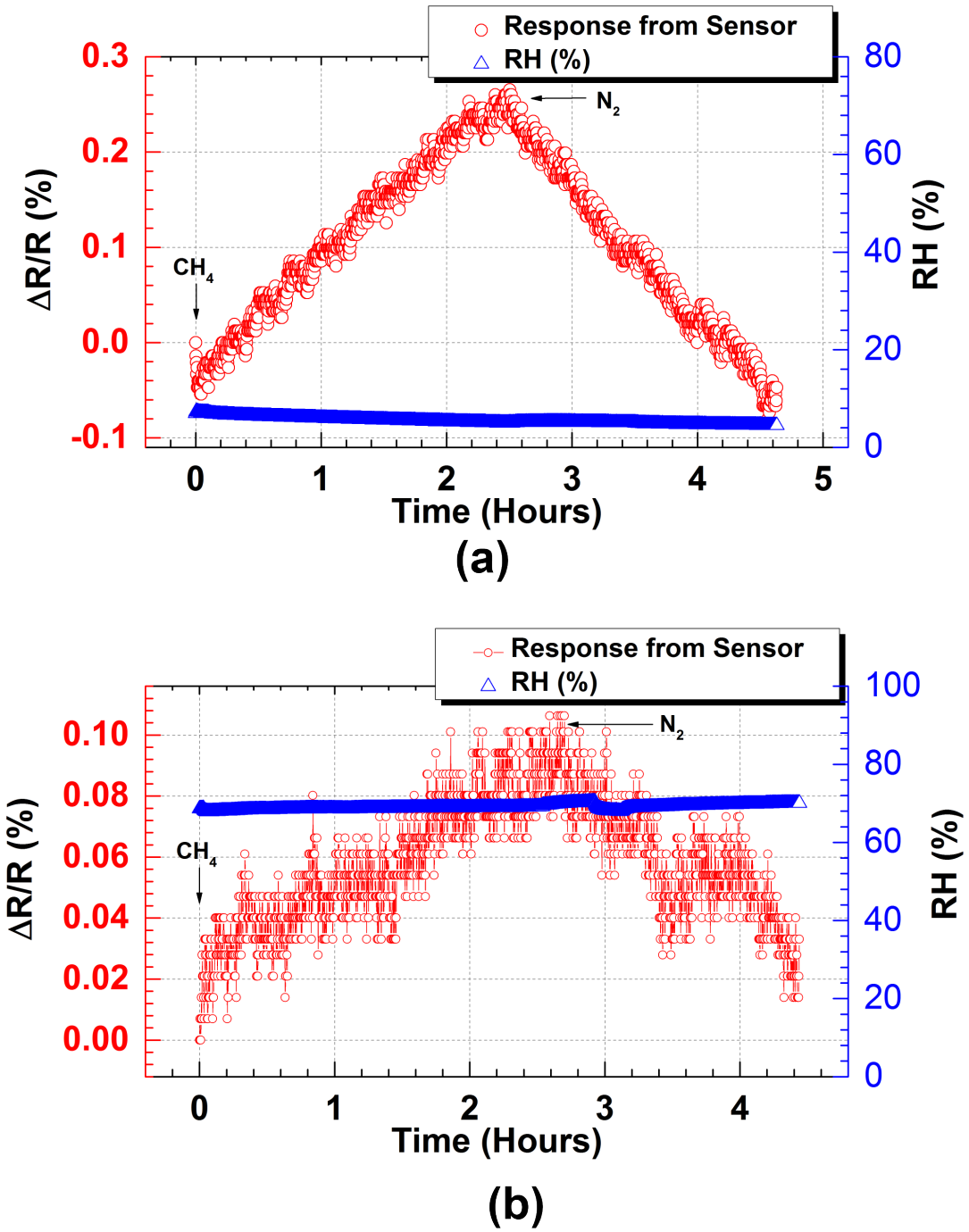

Figure 24: Relative resistance change of the SnO_2-MWCNT chemoresistor sensor when exposed to 10 ppm of CH_4 in dry air at (a) a lower RH (approximately 5%) and (b) a higher RH (approximately 70%). Both followed by a N_2 purge to recover the sensor response to its original value. The circle represents relative resistance change ($\Delta R/R = (R_{methane} - R_{air})/R_{air}$) of the chemoresistor sensor (left hand y-axis) while the triangle represents the RH inside the test chamber recorded by a commercial RH data logger, HOBO (right hand y-axis).

CHAPTER 5

THE EFFECTS OF SURFACE ACTIVATION ON THE RESPONSE OF METHANE SENSORS BASED ON METAL OXIDE NANOCRYSTALS FUNCTIONALIZED MULTI-WALLED CARBON NANOTUBES

A uniform coverage of functionalizing particles (ranging from metal (27), metal oxides (28), polymer coating (33) to biomolecules (32)) must be deposited uniformly on the surfaces of pristine carbon nanotubes in order to enable effective and reversible electrical modulation in the presence of target gas species. Unfortunately, in general, the surfaces of pristine CNTs show poor affinity with the functionalizing materials (43; 41; 42; 45; 46). Consequently, before applying the functionalization materials, *pre-activation* of the inert graphitic surface of the pristine CNTs is necessary (43; 41; 42).

In this chapter we present a comparative analysis of UVO and O_2 plasma-based surface pre-activation processes, that enable highly effective functionalization of MWCNTs with metal oxide nanocrystals (MONCs). O_2 plasma and UVO-based surface pre-activation have not yet been applied to CNT-based CH_4 chemoresistor sensors (27; 51; 79). Weaker affinity among the CNT surfaces and the functionalizing nano-particles, resulting from the absence of surface pre-activation, may greatly affect the sensor's reversible response to low ppm methane. TEM, SEM, XPS, and Raman spectroscopy results presented in this chapter show that by forming various functional (chemical) groups on the MWCNT surface, which act as active sites, O_2 plasma

and UVO-based dry pre-treatment techniques greatly enhance the affinity between MWCNT surface and the functionalizing MONCs deposited by ALD. This chapter presents a comparative study of the relative resistance changes of O_2 plasma and UVO pre-activated MONC-MWCNT chemoresistive sensors, in the presence of 10 ppm methane in air.

As mentioned in Section 2.2.2.4, prior to embedding functionalizing materials, the surface of bare CNTs is activated by exposing it to high temperature vapors (41) and/or using wet chemistry (42). Depending on temperature and air-exposure, the high-temperature may actually destroy or excessively damage the CNTs (41). Acid treatments used in wet chemistry can reduce considerably the mechanical and electronic performance of the tubes by introducing large numbers of defects (40). Wet chemistry also involves several additional steps, such as dissolution, sonication, mixing, and drying (41). This process also often causes undesirable agglomeration of treated CNTs.

To increase the efficiency of the functionalizing process, two alternative dry activation processes have been proposed: (a) gas plasma (43; 42; 41), and (b) UVO treatment (44).

Due to the interaction of surface C atoms with active O atoms during O_2 plasma or UVO activation, and subsequent exposure to atmosphere, chemical groups such as COOH (carboxyl), C=O (carbonyl), C-OH (hydroxyl) and C-O-C (ether) are formed on the MWCNT surface (42; 45; 46; 76; 80). These groups act as active sites for the nucleation of MONCs (42; 45; 46; 44). Both the O_2 plasma and UVO exposure have no effect on the aspect ratio (i.e. length to diameter ratio) of the MWCNTs (40).

A detail analysis on the effects of O_2 plasma and UVO based surface activation is presented in the remainder of this chapter.

Overall, the chapter is structured as follows: Section 5.1 describes XPS experimental results analyzing the formation of active functional groups on the O_2 plasma and UVO pre-activated MWCNT. Section A.1 shows the TEM results that describe the effect of surface pre-activation on the nucleation and binding of the MONCs on the MWCNT surface. Section 5.3 explains the results of Raman characterization of surface pre-activated and untreated MONC-MWCNTs. Section 5.4 focuses on the necessity of surface pre-activation of MWCNT based on different sensors' response to 10 ppm CH_4 in air mixture at room temperature. Finally, concluding remarks are offered in Section 6.3.

5.1 XPS study

High resolution XPS ($h\nu$=650 eV) was carried out using beamline 4-ID-C at the Advanced Photon Source (APS), Argonne National Laboratory. MWCNTs were deposited on gold-covered silicon substrates. Binding energies were calibrated to the Au 4f binding energy of 84.0 eV. Quantification was performed using XPS data analysis software CasaXPS. Figure 25 shows the C 1s and O 1s peaks originating from the pristine, 5 mins O_2 plasma-activated and 20 min UVO activated MWCNT. The assignments of the C 1s and O 1s components were based on reported spectra containing specific oxygen functional groups (80; 81; 82; 83). The measured spectra were fitted to a function having 70 % Gaussian and 30 % Lorentzian character, after performing a Shirley background correction. The C1 component centered at 284.3 eV represents the sp^2 graphitic component. The components at 285.4 eV, 286.5 eV, 287.7 eV and 289.1 eV (C2 up

to C5) were assigned to C atoms forming C-OH, C-O-C, >C=O and COOH functional groups respectively (81; 82; 83; 80). Peaks at 531.1 eV (O1), 532.2 eV (O2), 533.5 eV (O3), and 534.7 eV (O4) showed the presence of >C=O, C-OH, C-O-C, and H_2O, respectively(81; 82; 83; 80).

The normalized peak areas (NPA) of various components of C 1s and O 1s spectra were calculated with respect to the area of their respective C1 component (sp^2) (Table V). Comparison among the NPA of C5 (COOH group) in each type of sample suggests that COOH is the primary functional group created by the surface activation process. The NPA of C-OH components (C2 and O2) are significantly larger in the surface-activated sample compared to the pristine sample, suggesting a strong presence of C-OH in the surface activated MWCNT as well. The NPA of C4 and O1, representing the >C=O group, were found to be highest in the 5 min plasma-activated MWCNT, but insignificant in pristine and 20 min UVO-activated MWCNT. On the other hand, the NPA of the C3 and O3, representing the C-O-C functional group, were found to be highest in the pristine MWCNT (Table V).

It is well known that active π bonds in C=C dissociate during plasma/UVO activation and react with active O atoms to create C-O bonds (76). C-O group later stabilizes by reacting with atmospheric H_2O and creates C-OH (76). After prolonged interaction with plasma/UVO, C atoms get strongly oxidized and create >C=O and COOH (80). This is the probable cause of the strong presence of COH and COOH groups in our plasma/UVO-treated MWCNTs. In contrast, surface C atoms of pristine MWCNT react with atmospheric H_2O to create C-O, a probable cause of the presence of C-O-C groups in pristine MWCNT (80). The x-ray absorption

data illustrated in Figure 26 also suggest the presence of COOH, C-OH and C-O-C functional groups on the surface of the UVO activated MWCNT (81).

In summary, XPS results corroborate the hypothesis that the surface activation process produces the COOH functional group along with C-OH and >C=O. In later steps these groups in later steps help with nucleating the functionalizing MONCs on the surface of the MWCNTs.

5.2 TEM study

The TEM micrographs show that MONCs are not visible on the surface of the untreated but ALD processed MWCNTs (Figure 27a) (experimental details can be found in Appendix A). Uniform deposition of ZnO-MONCs was found on the surfaces of the pre-treated MWCNT (Figure 27b). The clearly visible lattice fringes in the HRTEM image in Figure 27d illustrate the wurtzite structure of the ZnO MONC and its good crystalline quality. The interplanar spacings of 2.8 Å, 2.68 Å and 2.48 Å correspond to the <100>, <002> and <101> planes of ZnO, resepectively (58). The HRTEM image in Figure 27c shows the atomic scale morphology of rutile SnO_2 MONCs deposited on the MWCNT surface. The interplanar spacings of 2.6 Å and 3.3 Å correspond to <101> and <110> planes of SnO_2, respectively. TEM results validate the hypothesis that surface pre-activation of the MWCNTs is essential for effective functionalization, i.e., nucleation and stronger binding of the MONCs to the surfaces of the MWCNTs.

5.3 Raman study

Room temperature Raman spectroscopy was performed using a Renishaw Invia micro-Raman system with a 514 nm laser. Three types of ZnO-ALD functionalized MWCNTs sam-

ples were used in the Raman characterization: (1) O_2 plasma pre-treated, (2) UVO pre-treated, and (3) untreated. Raman spectra, illustrated in Figure 28, reveal that after the surface pre-treatment and ALD functionalization, the D, G and G' band peaks of the MWCNTs are preserved, while additional Raman peaks originating from the ZnO NCs appeared. The characteristic Raman peaks of ZnO NCs, represented by a, b, c and e were observed only on the O_2 plasma pre-treated (1) b, c and e were observed on the UVO pre-treated samples (2), while none of these peaks were visible on the untreated MWCNTs samples (3); consistent with the hypothesis that the ZnO-MONC functionalization is enhanced in surface-activated MWCNTs. The peaks described in Fig. Figure 28b– 200.6 cm^{-1} (a), 324.25 cm^{-1} (b), 430.84 cm^{-1} (c), 569.87 cm^{-1} (e)–correspond to $2E_2^{low}$, $E_2^{high} - E_2^{low}$, E_2^{high}, A_1(LO), modes of ZnO(60; 39), respectively, suggesting that surface pre-treated samples have ZnO with a high crystalline quality. In addition, the characteristic ZnO Raman peaks are sharper in O_2 plasma pre-treated MWCNTs than in UVO pre-treated MWCNTs. The full width at half maximum (FWHM) of the A_1(LO) peak was found to be 50.5 cm^{-1} and 62.29 cm^{-1} for O_2 plasma pre-treated and UVO pre-treated samples, respectively, also suggesting superior crystal quality of ZnO on O_2 plasma pre-treated MWCNTs (60). Consequently, Raman characterization results validate the hypothesis that surface pre-activation of the MWCNTs is essential for effective functionalization, i.e., stronger nucleation and binding of the MONCs on to MWCNTs surfaces.

5.4 Methane Sensing Results

A series of experiments were conducted to evaluate the effects of UVO and O_2 plasma pre-treatments on the performance of the MONC-MWCNT sensor. The relative resistance of the

sensor ($\Delta R/R = (R_{methane} - R_{air})/R_{air}$) monotonically increased at room temperature when 10 ppm CH_4 in air was introduced to the test chamber. While maintaining a constant flow rate, when the incoming gas was switched from CH_4 to N_2, the relative resistance of the sensor decreased and returned to baseline (Figure 29 a-c). The monotonic increase in the sensor's relative resistance is a result of absorption of CH_4 molecules on the MONC functionalized MWCNT surface. The Fermi level (E_F) of the p-type MWCNT shifts away from the valence band due to electron transfer from the CH_4 molecules to the MONC-MWCNT hybrid nanostructure, and hence increases the electrical resistance of the MWCNT.

Figure 29 corroborates the assumption that surface pre-activation is essential for effective functionalization of the MWCNT by MONCs and for the sensor to act reversibly in the presence and absence of 10 ppm CH_4 in air. During alternating exposure to CH_4 and N_2 the relative resistance of the surface pre-treated ZnO-MWCNT sensor changed in reproducible fashion (Figure 29a and b). Figure 29c illustrates the dynamic response of a surface pre-activated SnO_2 functionalized MWCNT chemoresistor sensor. No discernible signals were observed from the untreated (but ZnO NC deposited) MWCNT sensor (Figure 29d).

At room temperature, the average relative resistance change ($\Delta R/R = (R_{methane} - R_{air})/R_{air}$) was found to be $1.91 \pm 0.98\%$ for UVO pre-treated, and $10.5 \pm 1.01\%$ for O_2 plasma pre-treated ZnO-MWCNT sensors. The result shows that the O_2 plasma pre-treatment significantly enhances the affinity of the MONCs (in this case ZnO NCs) to the MWCNTs surface in comparison to UVO pre-treatment; thus causing stronger electron transport through the ZnO-MWCNT junction, i.e, a larger resistance change in the presence of CH_4 at room temperature (Figure 29a-

b). This likely due to the better crystal quality of the ZnO NCs on O_2 plasma pre-treated MWCNTs compared to UVO pre-treated MWCNTs (as also indicated by the Raman results in Figure 28).

5.5 Summary

In summary, compared to UVO pre-treatment, O_2 plasma pre-treatment has a stronger impact on enhancing the MONC functionalization of MWCNTs and thus on the response of the chemoresistive sensors to 10 ppm CH_4 in air. The strong relative resistance change to a 10 ppm of CH_4 at room temperature is a consequence of: (a) strong electron transfer to the MONCs from CH_4 molecules, (b) energetically favorable electron transport at the MONC-MWCNT junction, and (c) enhanced affinity of the surface pre-treated MWCNT to MONCs as a result of formation of active chemical groups. The O_2 plasma and UVO-based activation processes give rise to COOH, >C=O, and C-OH functional groups on the MWCNT surface, hence enhance the nucleation and bonding of MONCs with the MWCNT. These treatments produce strong reversible relative resistance changes of the chemoresistors under iterative exposure to 10 ppm CH_4 in air.

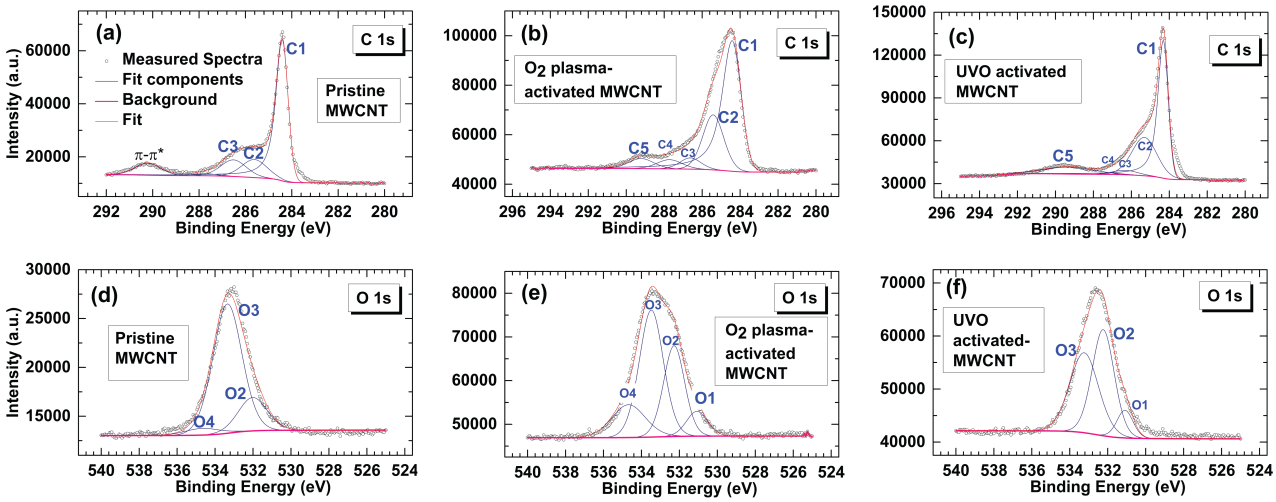

Figure 25: (a)-(c): C 1s XPS peaks of (a) pristine MWCNTs (b) 5 mins O_2 plasma activated MWCNTs, and (c) 20 mins UVO activated MWCNTs. (d)-(f): O 1s XPS peaks of (d) pristine MWCNTs (e) 5 mins O_2 plasma activated MWCNTs, and (f) 20 mins UVO activated MWCNTs.

TABLE V: Comparison among normalized peak areas (NPA; with respect to C1) of C 1s (C2 to C5) and O 1s (O1 to O3) peak components in pristine, plasma treated and UVO treated MWCNT samples

Peak Component	Location (eV)	Functional Group	**NPA**		
			Pristine MWCNT	Plasma Treated MWCNT	UVO Treated MWCNT
C2	285.4	C-OH	0.29	0.50	0.73
C3	286.5	C-O-C	0.26	0.10	0.08
C4	287.7	>C=O	0.03	0.10	0.02
C5	289.1	COOH	not present	0.11	0.26
O1	531.1	>C=O	0.02	0.13	0.09
O2	532.2	C-OH	0.20	0.47	0.48
O3	533.5	C-O-C	0.77	0.76	0.47

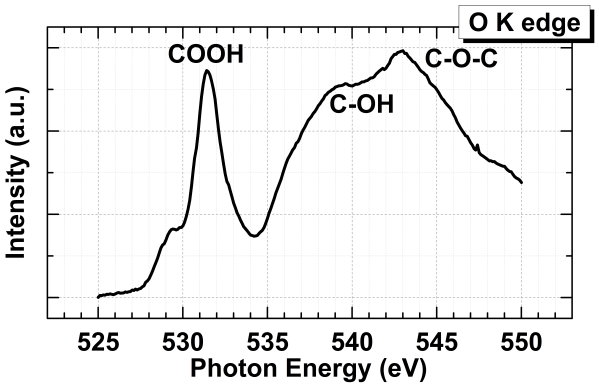

Figure 26: O K edge x-ray absorption spectra obtained from UVO activated MWCNTs.

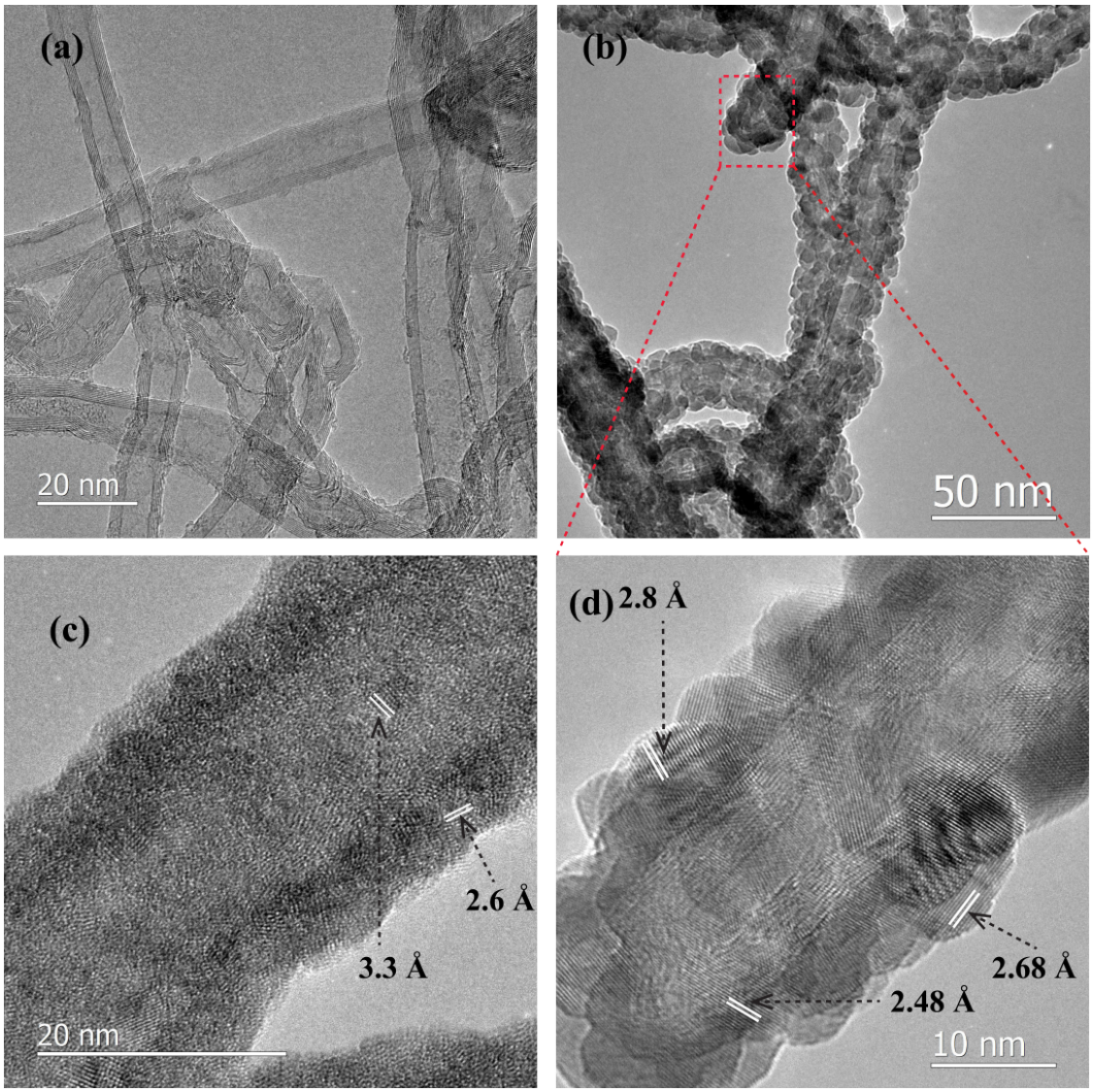

Figure 27: (a) The transmission electron microscopy (TEM) image of untreated but ZnO deposited MWCNTs. ZnO nanocrystals were not visible on the surface of these untreated MWCNTs. (b) Uniform distribution of atomic layer deposited ZnO nanocrystal layers on the UVO pre-treated MWCNT surface. (c) Higher resolution TEM image of a SnO_2-MWCNT (ALD at 175 ^{0}C) sample showing interplanar spacing of 2.6 Åand 3.3 Å corresponding to $< 101 >$ and $< 110 >$ planes of SnO_2. (d) Higher resolution TEM image of a ZnO-MWCNT (ALD at 175 ^{0}C) sample showing interplanar spacing of 2.8 Å, 2.68 Åand 2.48 Å corresponding to $< 100 >, < 002 >$ and $< 101 >$ planes of ZnO.

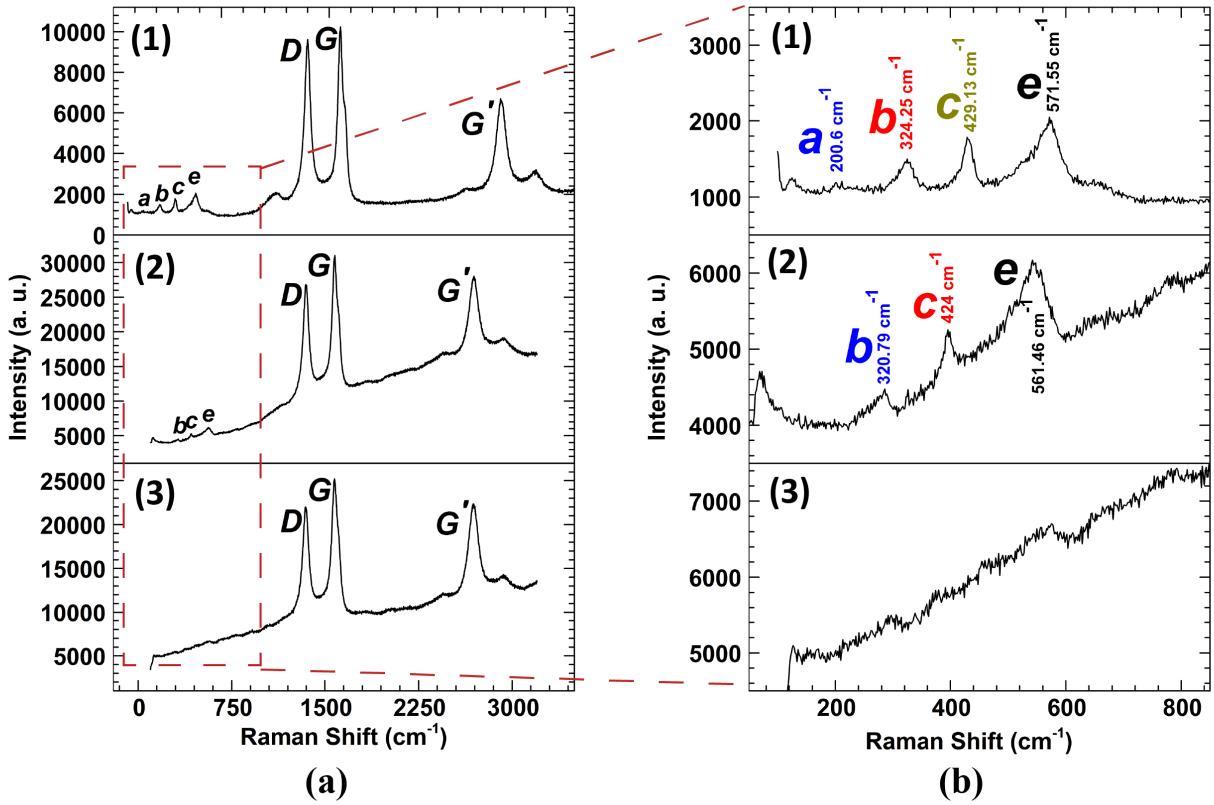

Figure 28: (a) Raman spectra obtained from the ZnO ALD at 220 ^{0}C on O_2 plasma treated MWCNT (top panel), UVO (30 mins) treated MWCNT (middle panel), untreated MWCNT (bottom panel). (b) Enlarged ZnO peaks in the range of 100 cm^{-1} to 850 cm^{-1} frequency shift.

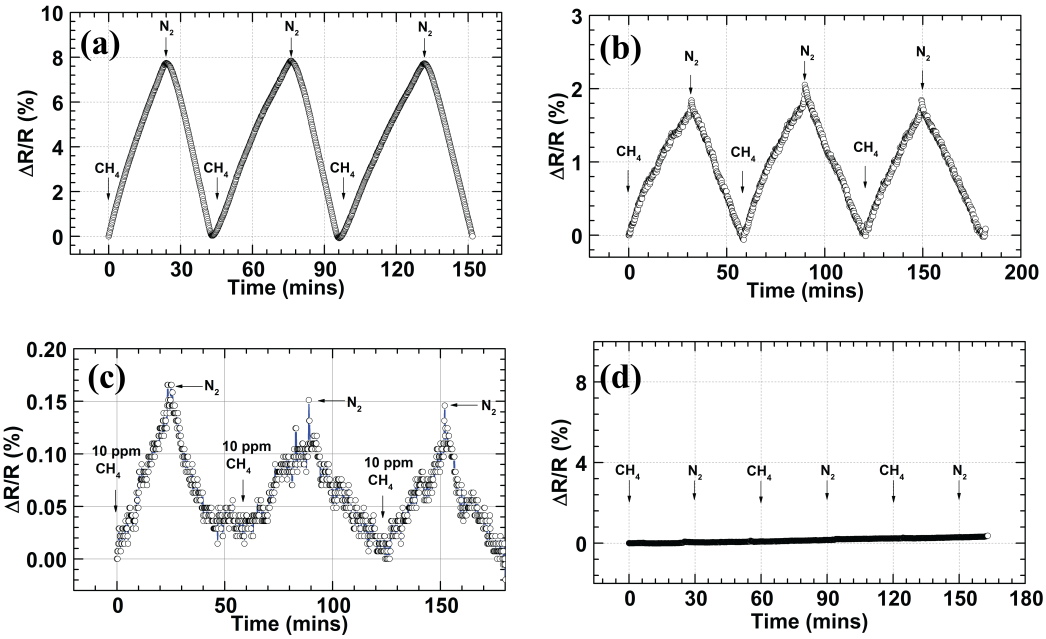

Figure 29: Comparison of the dynamic sensor response ($\Delta R/R = (R_{methane} - R_{air})/R_{air}$) of MONC-MWCNT sensors to 10 ppm CH_4 in dry air, followed by flushing by N_2 for sensor recovery. Each section of the figure shows ($\Delta R/R$ for: (a) O_2 plasma pre-treated ZnO functionalized, (b) a UVO pre-treated ZnO functionalized, (c) a UVO pre-treated SnO_2 functionalized, and (d) an untreated but ZnO deposited MWCNT sensor.

CHAPTER 6

PHOTOLUMINESCENCE OF ZNO-MWCNT AND UV-ACCELERATED RECOVERY TO BASELINE

Once a chemoresistor CH_4 sensor is exposed to CH_4 it takes a long time for the sensor to return to the baseline resistance, i.e., recovery (27; 84). In this chapter a UV recovery technique is presented for the ZnO-MWCNT CH_4 thus improving the recovery time two orders of magnitude compared to published studies (27) as well as our previous work (84). Optoelectronic application of ZnO-CNT, such as optical switching has been reported before (85; 59). ZnO is a wide-bandgap semiconductor (3.37 eV) with a large exciton binding energy (60 meV) (59), which facilitates photo-induced enhancement of sensor recovery. This chapter is constructed as follows: Section 6.1 describes room temperature photoluminescence experiments on ZnO-MWCNT samples with various thicknesses of ZnO NCs. Section 6.2 offers a study of the surface recovery of ZnO-MWCNT CH_4 chemoresistor sensors exposed to various wavelengths of UV light. Finally, Section 6.3 summarizes the chapter.

6.1 Photoluminescence of ZnO-MWCNT

PL experiments were conducted at room temperature using a Horiba Jobin-Yvon Nanolog Spectrofluorimeter with excitation at 255 nm. Surface pre-activated ZnO-MWCNT samples with various thicknesses of ZnO were used in the PL experiment.

6.1.1 PL sample preparation

ZnO was deposited on pre-treated MWCNTs using the ALD process described in Chapter 3 and shown in Figure 30. MWCNTs (98 % pure) with an average diameter of 12 nm, average lengths of 10 μm, and a specific surface area of about 220 m^2/g were purchased from Sigma Aldrich. Using a micro-syringe, an aliquot of 50 μL from a 50 g/50 mL solution of MWCNT-ethanol was deposited on 10 mm by 10 mm SiO_2/Si substrates. This was followed by baking the samples at 75 °C to remove the ethanol and improve adhesion. The deposited MWCNTs were O_2 plasma treated in a reactive ion etching (RIE) chamber (March plasma CS-1701). The base pressure of the plasma chamber was about 40 mTorr. O_2 was introduced at a flow rate of 20 sccm while the pressure was maintained at 160 mTorr during the process. The O_2 plasma was generated by applying a radio frequency (RF) of 13.56 MHz with a power of 100 watts. The duration of the plasma treatment was 5 mins. A UVO cleaner (Nanonex Ultra 100) was used for the UVO treatment of the MWCNT surface. Vacuum UV light (185 nm) illuminated ambient air for generating O_3 and activating the MWCNT surface. The process took 20 min.

ALD was used at 175 °C to deposit ZnO on the surfaces of the pre-activated MWCNTs with diethylzinc ($(C_2H_5)_2Zn$) (DEZ) as a precursor. The process was performed with an Arradiance Gemstar ALD tool. The pulse duration for DEZ and water vapor was 22 ms. Samples were prepared by 12, 24, 36, and 48 cycles of ALD, expected to produce 2 nm, 4 nm, 6 nm and 8 nm thick ZnO NCs, respectively. During each ALD process O_2 plasma (5 min) and UVO (20 min)treated SiO_2/Si substrates were used as reference samples.

6.1.2 PL results

Figure 31 illustrates the PL peaks emitted from ZnO NCs deposited on O_2 plasma and UVO treated SiO_2 substrates. The average peak positions for UV emission is about 385 nm while and the average peak positions for visible emission is about 517 nm. PL spectra of 5 min O_2 plasma pre-treated ZnO-MWCNTs (ZnO ALD temperature 175 °C,12–48 cycles) are presented in Figure 32. PL spectra of 20 min UVO pre-treated ZnO-MWCNTs (ZnO ALD temperature 175 °C, no. of cycles 12–48) are shown in Figure 33. The peak parameters are summarized in Table VI.

PL peaks at 376 nm – 385 nm represent the near-band edge emissions of the wide band-gap ZnO (59; 86; 87). The near band edge emission at approximately 3.2 eV has been reported to be caused by the radiative decay of free excitons and their phonon replicas (85). The presence of the green peak around 520 nm results from excitons that have relaxed to deeper defect states (85; 86). Extrinsic and intrinsic defects may cause this deep level emission (DLE) (87). Oxygen vacancy is the general intrinsic defect in ZnO causing green luminescence (86). Interstitial Zn atoms also have been reported to be the cause of green luminescence (87) from ZnO.

The PL results suggest UV irradiation (360 nm–390 nm) excites electrons from the valence band to the conduction band of the functionalizing ZnO, facilitating desorption of CH_4 molecules.

6.2 UV exposure accelerated recovery

Two types of tests were conducted to study the effect that UV irradiation has on the removal of the CH_4 from the MONC-MWCNT. For the first set of tests, after the introduction

of CH_4, the sensor was exposed to UV light (wavelength of 390 nm) while the test chamber was simultaneously flushed with N_2 (Figure 34). The recovery time (time to return to baseline) of the sensor was significantly reduced as a result of UV exposure while the time to saturation remained almost constant. Figure 34 demonstrates that the O_2 plasma (5 min) pre-activated ZnO-MWCNT sensor required almost an hour to reach saturation with an average relative resistance change of 20% ($(\Delta R/R = (R_{methane} - R_{air})/R_{air})$). The average recovery time was almost 30 min with N_2 exposure alone, while it was almost 6 min with application of UV (390 nm) and N_2 (the first and second cycle in Figure 34). The improvement in the recovery time was likely due to the UV induced reduction of the desorption energy barrier of the CH_4 molecules at the sensor surface (27).

During the second sets of tests the sensor was first exposed to 10 ppm CH_4 in air for 30 min. Without interrupting the flow of CH_4 , the sensor was irradiated with UV light (390 nm) until the sensor returned to its baseline resistance (Figure 35). A recovery time of about 3 minutes was observed.

Figure 36 shows the ZnO-MWCNT sensor recovery while irradiated with UV light at 365 nm. UV light with a wavelength of 365 nm is in resonance with the energy bandgap of ZnO (3.4 eV). The sensor was first exposed to 10 ppm CH_4 in air for 60 min, then without interrupting the flow of CH_4 , the sensor was irradiated with UV flashlight (365 nm) until the sensor returned to its baseline resistance. The recovery time was less than 10 s, two orders of magnitude shorter than results previously reported in literature (27; 84). This important result, coupled with reproducibility of the resistance increase while UV irradiation is off, allows us to dramatically

reduce the period during which data cannot be collected by the sensor while the sensor is being reflushed.

6.3 Summary

The recovery time for ZnO-MWCNT CH_4 sensors was significantly reduced by utilizing the strong response of ZnO to UV. Recovery times of the sensor by N_2 purge, N_2 purge + UV (390 nm) irradiation, and simple UV irradiation (390 nm and 365 nm) were compared. With 365 nm, the recovery time reduced two orders of magnitude (from about 30 min to about 10 s) compared to existing literature results including our previously published work. The behavior of the sensor under different wavelengths of UV exposure was predicted from the photoluminescence properties of ZnO-MWCNT.

TABLE VI: Photoluminescence peaks emitted from 5 min O_2 plasma and 20 min UVO pre-activated MWCNTs functionalized with ZnO NCs by ALD at 175 °C.

Pre-activation	No. of ALD cycles	ZnO Thickness	UV-peak position (nm)	Visible-peak position (nm)
5 min O_2 Plasma	12	2 nm	350, 400, 454	517
5 min O_2 Plasma	24	4 nm	376	517
5 min O_2 Plasma	36	6 nm	385	517
5 min O_2 Plasma	48	8 nm	385	517
20 min UVO	12	2 nm	331, 352, 394, 454	517
20 min UVO	24	4 nm	376	517
20 min UVO	36	6 nm	385	517
20 min UVO	48	8 nm	382	517

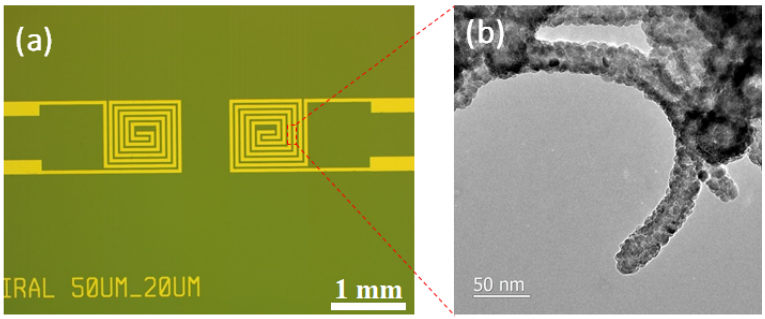

Figure 30: (a) Optical micrograph of a microfabricated ZnO-MWCNT chemoresistor CH_4 sensor. ZnO-MWCNT is deposited on top of interdigitated Au electrodes. (b) Transmission electron microscope image of ZnO functionalized MWCNT.

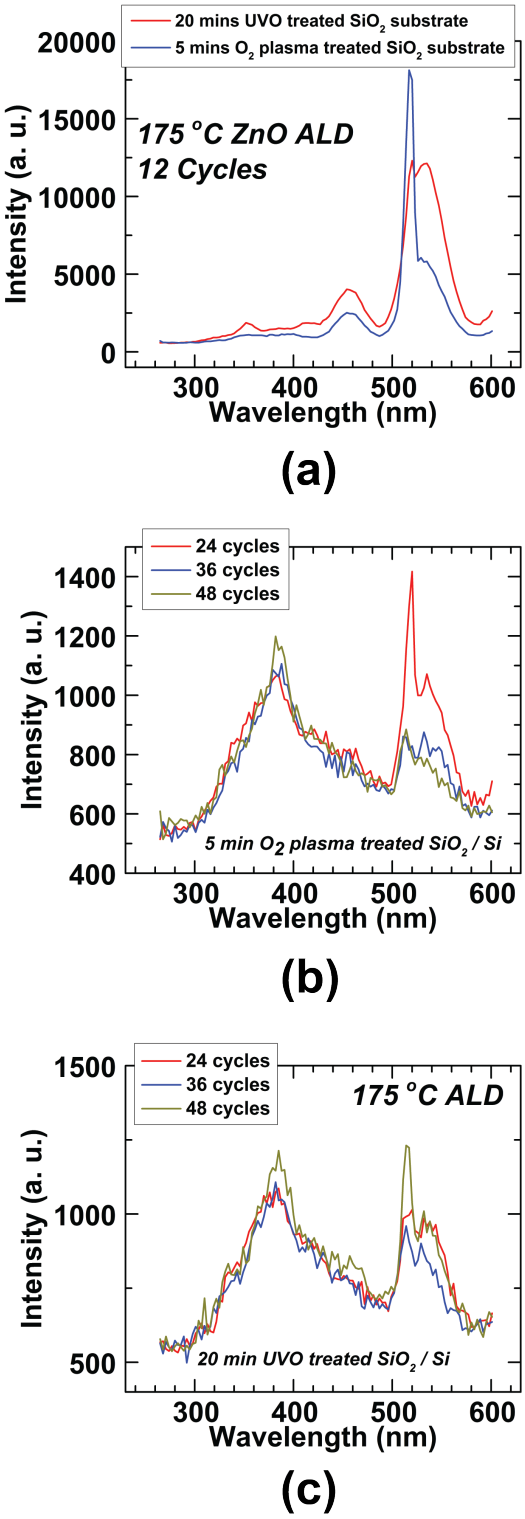

Figure 31: PL spectra after excitation at 255 nm. (a) 2 nm thick ZnO (12 cycles of ALD) deposited on 20 min UVO pre-treated and 5 min O_2 plasma pre-treated SiO_2/Si substrate. (b) ZnO deposited on 5 min O_2 plasma pre-treated SiO_2/Si substrate. 12, 24, 36, and 48 ALD cycles were expected to produce 2 nm, 4 nm, 6 nm, and 8 nm thick ZnO. (c) PL spectra from ZnO deposited on 20 min UVO pre-treated SiO_2/Si substrate. 12, 24, 36, and 48 ALD cycles were expected to produce 2 nm, 4 nm, 6 nm, and 8 nm thick ZnO. The ALD temperature was 175 °C for all samples.

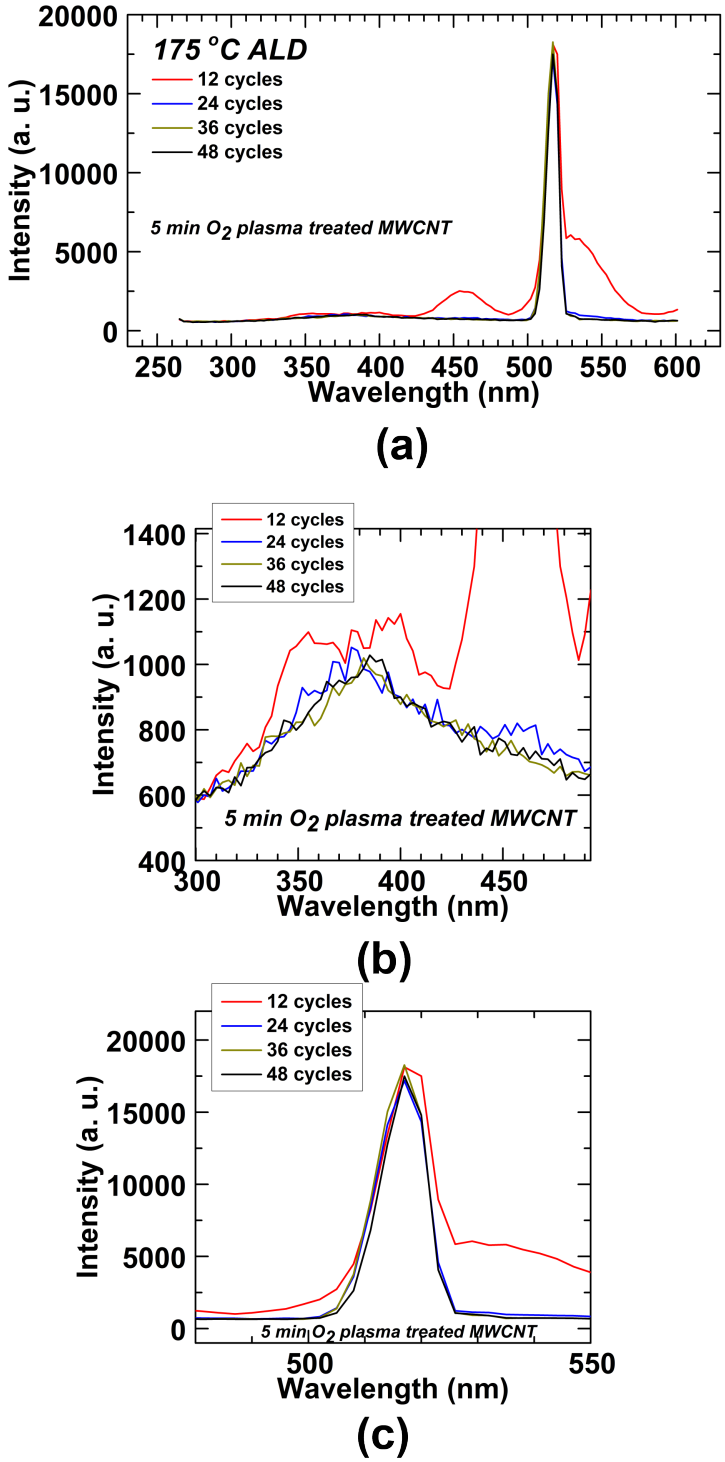

Figure 32: (a) PL spectra of 5 min O_2 plasma pre-treated and ZnO functionalized MWCNTs. The ALD temperature was 175 °C. 12, 24, 36, and 48 ALD cycles were expected to produce 2 nm, 4 nm, 6 nm, and 8 nm thick ZnO. (b) and (c) show UV and visible PL peaks in more detail. Horiba Jobin-Yvon Nanolog Spectrofluorimeter was used to conduct the room temperature PL experiments with a 255 nm incident light.

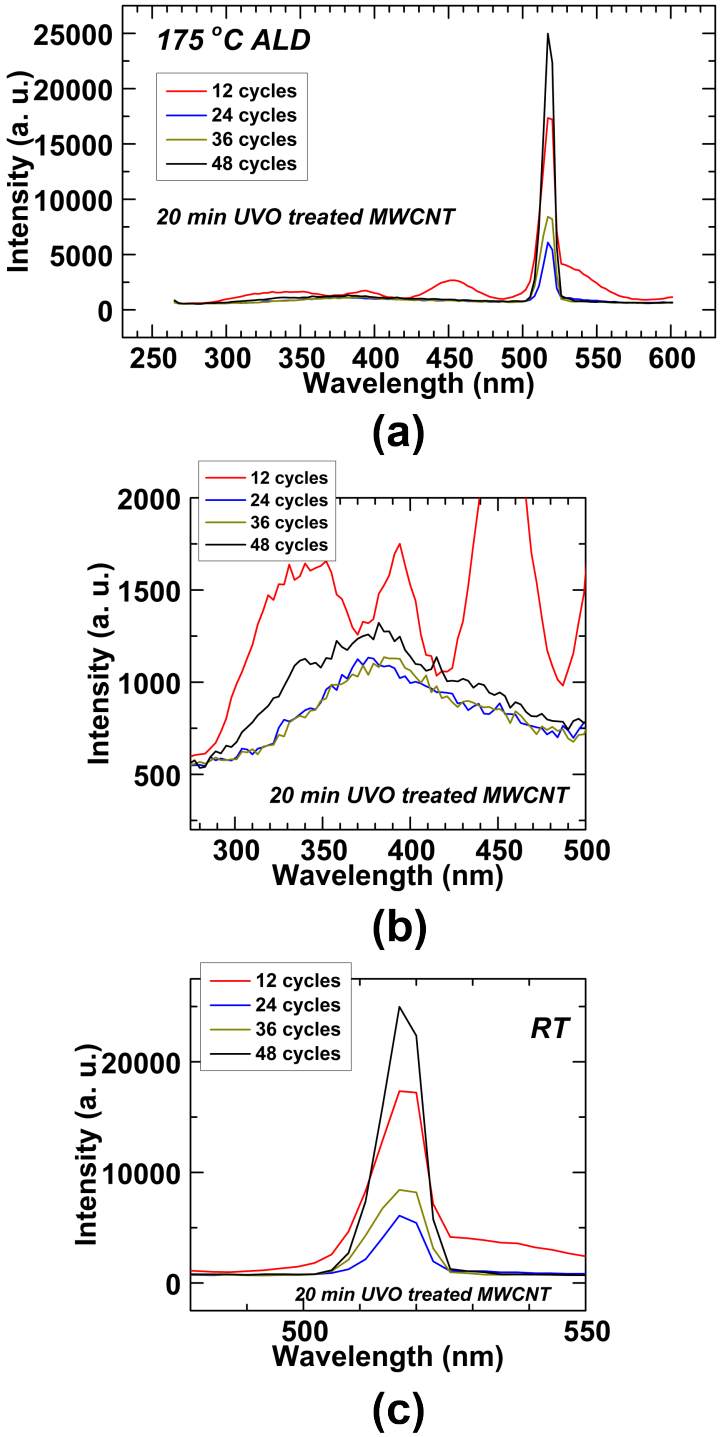

Figure 33: (a) PL spectra of 20 min UVO pre-treated and ZnO functionalized MWCNTs. The ALD temperature was 175 °C. The ALD temperature was 175 °C. 12, 24, 36, and 48 ALD cycles were expected to produce 2 nm, 4 nm, 6 nm, and 8 nm thick ZnO. (b) and (c) show UV and visible PL peaks in more detail. Horiba Jobin-Yvon Nanolog Spectrofluorimeter was used to conduct the room temperature PL experiments with a 255 nm incident light.

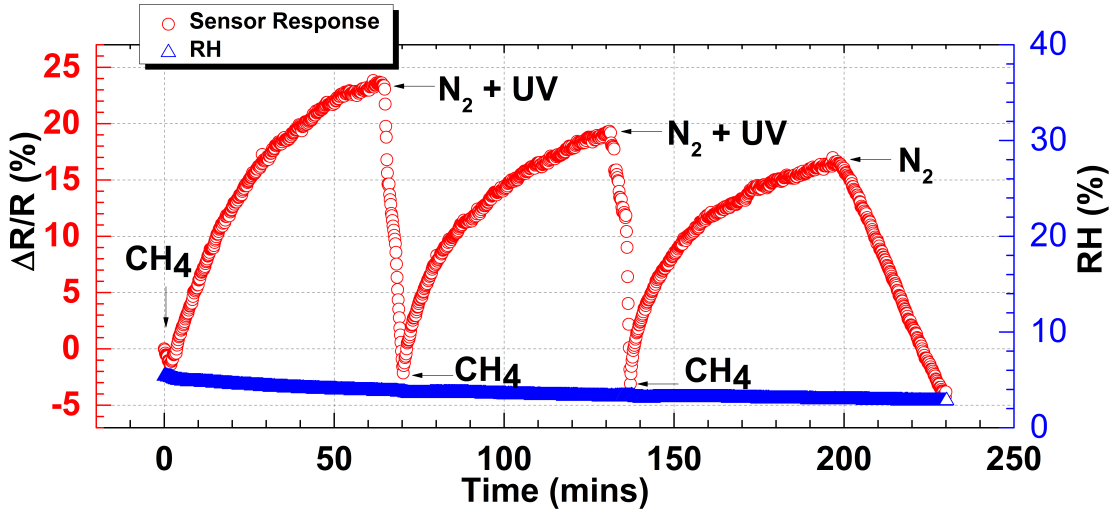

Figure 34: Relative resistance change ($\Delta R/R = (R_{methane} - R_{air})/R_{air}$) of the ZnO-MWCNT sensor while exposed to iterative cycles of 10 ppm of CH_4 in air and N_2+UV or N_2. The right hand y-axis represents the RH inside the chamber during the test. The duration of CH_4 exposure was approximately 60 mins in order to reach saturation with a relative resistance change of almost 20 %. The recovery time of the sensor was almost 6 mins with the UV application during the N_2 purge (first 2 cycles) while it was almost 30 mins with non-UV N_2 purge (last cycle).

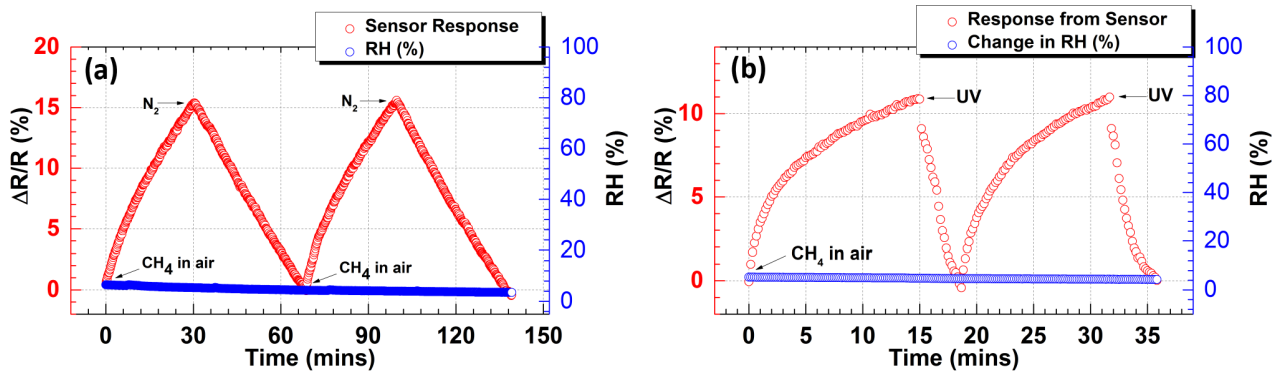

Figure 35: (a) Relative resistance ($\Delta R/R = (R_{methane} - R_{air})/R_{air}$) of the ZnO-MWCNT sensor while exposed to 10 ppm CH_4 in air and recovered by switching from CH_4 to N_2. Average recovery time was almost 35 mins. (b) The sensors were irradiated with a 390 nm wavelength UV light for recovery (without stopping the CH_4 flow). Average recovery time was about 3 mins. After each UV exposure, the sensor peaked in about 15 mins. Relative humidity during both tests was constant at 1 to 2%.

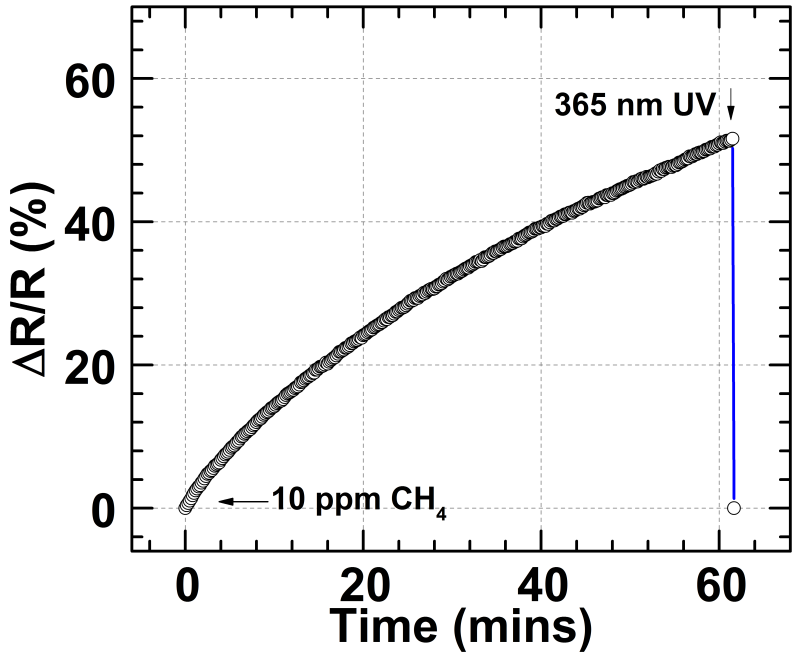

Figure 36: Relative resistance ($\Delta R/R = (R_{methane} - R_{air})/R_{air}$) of the ZnO-MWCNT sensor while exposed to 10 ppm CH_4 in air and recovered by UV irradiation with 365 nm of wavelength (without stopping the CH_4 flow). Recovery time was less than 10 s. Relative humidity during the test was constant at 1 to 2%.

CHAPTER 7

FUNCTIONALIZED MULTI-WALLED CARBON NANOTUBE BASED SENSORS FOR DISTRIBUTED METHANE LEAK DETECTION

(Some of the figures and a portion of text presented in this chapter was previously published as: "Functionalized Multi-Walled Carbon Nanotube based Sensors for Distributed Methane Leak Detection.", Md Humayun, R. Divan, L. Stan, D. Rosenmann, D. Gosztola, L. Gundel, P. A. Solomon, and I. Paprotny, Conference Proceeding for IEEE Sensors, 1-4 Nov. 2015, DOI: 10.1109/ICSENS.2015.7370207 © 2015 IEEE)

This chapter presents a highly sensitive, energy efficient and low-cost distributed methane sensor system (DMSS) for continuous monitoring, detection, and localization of CH_4 leaks in natural gas infrastructure, such as transmission and distribution pipelines, wells, and production pads. The CH_4 sensing element, a key component of the DMSS, consists of a metal oxide functionalized multi-walled carbon nanotube (MWCNT) mesh. For the DMSS, a Gaussian plume triangulation algorithm has been developed, which, given a geometric model of the surrounding environment, can precisely detect and localize a CH_4 leak as well as estimate its mass flow rate.

In this chapter, we describe a low-cost microfabricated CH_4 sensing system and a corresponding detection algorithm for pinpointing leaks in natural gas infrastructures. A leak detection algorithm for low-cost microfabricated CH_4 sensor networks for natural gas distribution systems has not been previously reported. The Gaussian plume triangulation algorithm

can precisely detect and localize a CH_4 leak and estimate its mass flow rate, if a geometric model of the surrounding environment is available. This algorithm complements the metal oxide functionalized CNT micro-fabricated CH_4 sensing element, which is the key component for the DMSS.

We are assuming a relatively faster response (less than 1 min) compared to our current generation of MWCNT sensors to gain accurate readings that account for wind speed and direction. Our on-going fabrication work focuses on reducing significantly the response time of the functionalized MWCNT sensor as described in Chapter 6.

In the following example the DMSS nodes are assumed to be distributed on a 10 m $\times$ 10 m grid over an area with potential for CH_4 leaks. However, the DMSS can be extended to numerous spatial sensor distributions. The approach relies on wind to sweep a plume of CH_4 from a nearby leak across two or more sensors. Using the National Wind Technology Center dataset (88) as a baseline (obtained near Boulder, Colorado, US) wind rose plots were analyzed for 4 randomly chosen 18 days period in 2013. The average (prevailing) direction of wind was west or south-west with the wind covering more than 180° in the course of 18 days. This is assumed to be a representative wind distribution and is used in the leak detection algorithm.

The remainder of the chapter is structured as follows: Section 7.1 provides mathematical background for the Gaussian plume model for the triangulation algorithm. Quantification of sensor the response and noise are analyzed in Section 7.2. The chapter is summarized in Section 7.3.

7.1 Gaussian plume model

A Gaussian plume model (GPM) (89) estimates the evolution of a plume emanating from a ground level leak for different wind directions and speeds. For a constant leak rate and a constant wind speed the ground level concentration χ (μg/m^3) at the point (x,y) may be written using the Gaussian plume equation as:

$$\chi(x, y, z_0, H) = \frac{Q \times 10^6}{\pi \sigma_y \sigma_z U} exp[-\frac{1}{2}(\frac{y}{\sigma_y})^2] \times exp[-\frac{1}{2}(\frac{H}{\sigma_z})^2] \tag{7.1}$$

where Q (μg/s) is the source emission rate, U(m/s) is the wind speed at stack height, σ_y and σ_z are the standard deviation of concentration distributions in crosswind and vertical directions respectively, H (m) is the effective stack height (the sum of stack height and plume rise), x (m) is the downwind distance from the stack, y (m) is the crosswind distance from the plume centerline, and z_0 (m) is the vertical distance from ground level, assumed to be zero.

From the fitting of Pasquill-Gifford-Turner diffusion coefficient curves, σ_y and σ_z are given as:

$$\sigma_y = cx^d \tag{7.2}$$

$$\sigma_z = ax^b \tag{7.3}$$

where, constants a, b, c, and d are 0.112, 0.91, 0.197, and 0.908, respectively. Figure 37 illustrates the Gaussian plume dispersion model terminology. Note that although the GPM

might not be applicable (due to turbulence) during high (> 6 m/s) wind velocities, such wind speeds are uncommon, and sensor readings during those times will be ignored without significantly compromising the 18 day detection time. Similarly, the readings at wind speeds below 1 m/s will be omitted.

If valid, the Gaussian plume distribution at a point x downstream of the leak is uniquely defined by the dispersion parameters, which are assumed constant, the wind velocity U (m/s) and the emission rate at the leak Q (μg/s).

Once a plume moves across a sensor location due to variations in wind direction, a plume distribution can be reconstructed. This concept is illustrated on Figure 38. As CH_4 plume from a nearby leak rotates from position (i) to position (ii), the sensor signal records the plume profile. The below analysis assumes the wind velocity is constant, which may not be the case; however the theory extends easily to cases with variable wind velocity.

Calculated distributions of a CH_4 plume using Equation 7.1 are plotted on Figure 39 as a function of rotating wind direction for two different wind velocities (1 ms^{-1} and 5 ms^{-1}). The distribution of methane concentration was calculated at different points along the centerline of the plume (2 m – 14 m distances from the leak location). The mass emission rate was assumed to be 0.032 g/s or 6 standard cubic feet per hour (SCFH).

The down-wind coordinate (x) from the leak (the distance to the sensor from the leak along the centerline of the plume), can be extrapolated from the peak concentration λ (ppm) and wind velocity U (m/s) by numerically solving the following equation:

$$log(ca) + (b+d)logx = log\frac{QV_m \times 10^3}{M\lambda\pi U} - \frac{(\Delta h)^2}{2a^2x^{2b}} \tag{7.4}$$

where, λ is the concentration of the detected CH_4 in parts per millions (ppm), M is the Molar mass of CH_4 (g/mol), V_m is the molar volume of an ideal gas at standard temperature and pressure. The plume rise due to the buoyancy of CH_4 (Δh) is calculated as

$$\Delta h = \frac{Ex^\beta}{\overline{u^\alpha}} \tag{7.5}$$

where, for a stable atmosphere, $\alpha = 1$, $\beta = 2/3$, and $E = 1.6F^{(1/3)}$, where F is the buoyancy flux parameter, defined as

$$F = \frac{gd^2V_s(T_s - T_a)}{4T_s} \tag{7.6}$$

where g is acceleration due to gravity (9.8 ms^{-2}), d (m) is stack diameter, V_s (m/s) is stack exit velocity, T_a (°C) is ambient temperature at stack height, and T_s (°C) is stack exit temperature at stack height.

Once distance to the leak (x) is established, the following formula can be used to calculate the leakage rate:

$$Q = \frac{\lambda M}{V_m} \times \frac{\pi\sigma_y\sigma_z U}{10^6} \times exp[\frac{1}{2}(y/\sigma_y)^2] \times exp[\frac{1}{2}(H/\sigma_z)]^2 \tag{7.7}$$

where Q (g/s) is the mass emission rate (MER) of the leak. Consequently, estimation of the MER of a single leak is possible by scanning the leak distribution plume.

The mass emission rate (MER) of the leak (g/s) as a function of maximum detected CH_4 concentration by sensors located at various distances along the plume centerline is illustrated in Figure 40.

The methane plume distribution at the sensor location is dependent on the vertical position of the leak, i.e., leak height. The distributions of a CH_4 plume as a function of wind angle for three different leak heights (0 m, 0.25 m, and 0.5 m) are plotted in Figure 41. The sensor experiences strongest plume concentration for ground level leak (Figure 41a). As the leak height increases the plume concentration experienced by the sensor becomes weaker (Figure 41b and c). The plume rise due to the buoyancy of CH_4 (Δh) is included in the plume distribution calculation. The distribution of methane concentration was calculated at different locations of the sensor along the centerline of the plume (2 m – 14 m distances from the leak position). The wind speed is assumed to be 5 m/s. The mass emission rate was assumed to be 0.032 g/s or 6 SCFH.

7.2 Quantifying sensor response and noise

The shape of the plume recorded by the sensor depends on its lower detection limit (LDL). Single ppm CH_4 LDL is currently achieved using our MONC-MWCNT chemoresistor sensor (84; 90). Our ongoing research is focused on achieving below ppm detection limit. For this particular analysis we estimated the integration time of the sensor as one minute. Assuming an error of $\pm LDL$, the error in plume height and plume width can be estimated. Errors in other factors, such as wind speed or wind direction will also contribute to the error of the sensor, but can be reduced by increasing integration time.

Figure 42 shows the center point plume concentration as a function of wind speed (1 − 5 ms^{-1}) and distance, for a point leak with mass emission rate of 6 SCFH. The error bars (Figure 42) indicate the distance uncertainty at 8 m distance from the leak (Note 14 m is the largest distance from the leak in a 10 m × 10 m grid).

7.3 Summary

This chapter presents a GPM-based algorithm for a distributed methane sensor system (DMSS) which can use our chemoresistor sensor to localize leaks in natural gas infrastructure, such as production wells and pads. We present a localization algorithm, which can be used with the distributed sensors to pinpoint CH_4 leaks, allowing the DMSS to be used for continuous low-cost monitoring of CH_4 emission. Together with energy harvesting and ultra-low power wireless solutions the DMSS can be used for ubiquitous monitoring of natural gas infrastructure.

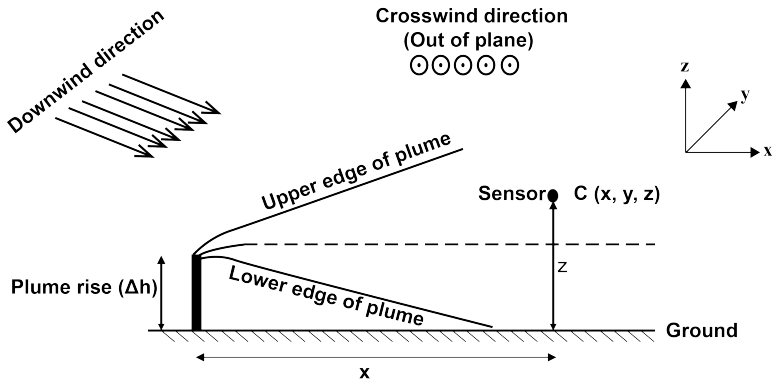

Figure 37: Illustration of the Gaussian plume dispersion model. © 2015 IEEE

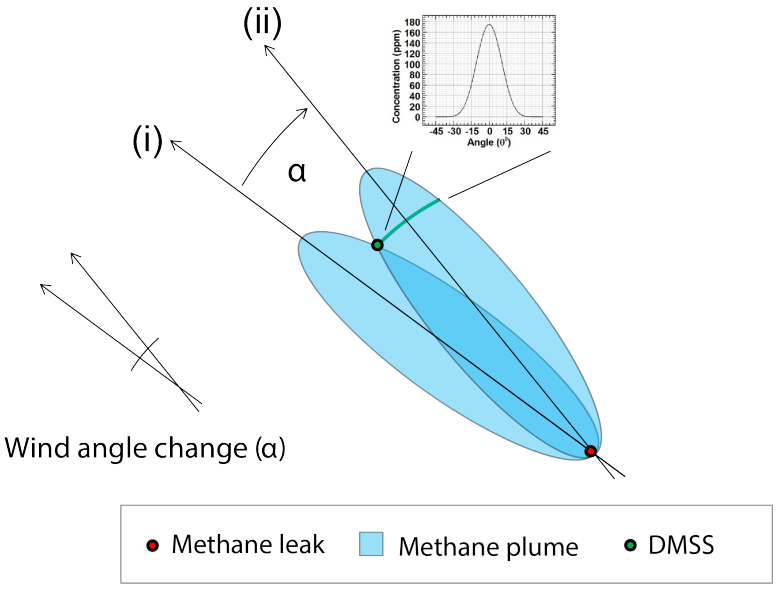

Figure 38: CH_4 plume propagating across a sensor node due to varying wind direction. This example assumes that wind velocity is constant as the angle varies. This example assumes that wind velocity is constant as the angle varies. © 2015 IEEE

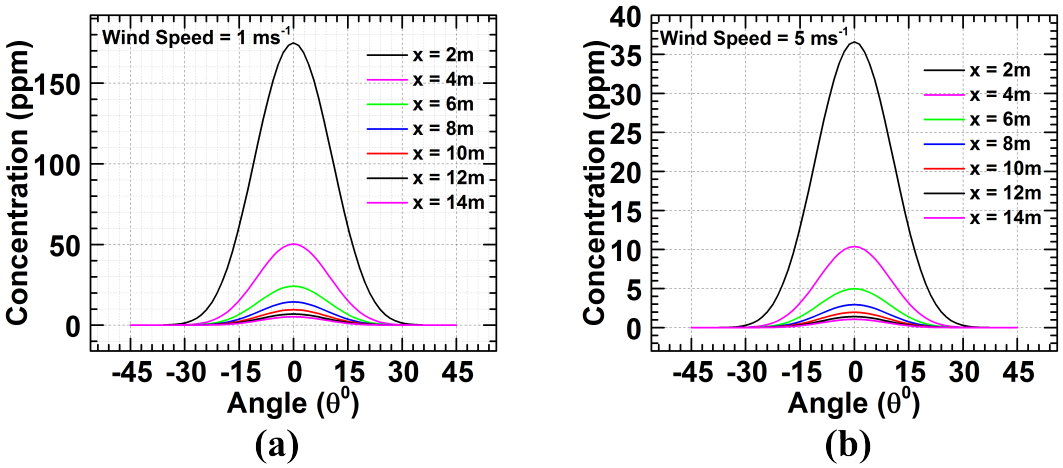

Figure 39: Distribution of CH_4 plume as a function of wind angle for two different wind speeds: (a) 1 m/s and (b) 5 m/s. The distribution of methane concentration was calculated at different points along the centerline of the plume (2 m – 14 m distances from the leak location). "Wind angle" is defined as the angle between the wind direction and the straight line connecting the location of the leak and the sensor. It also represents the rotation of the wind direction. The mass emission rate was assumed to be 0.032 g/s or 6 standard cubic feet per hour (SCFH).

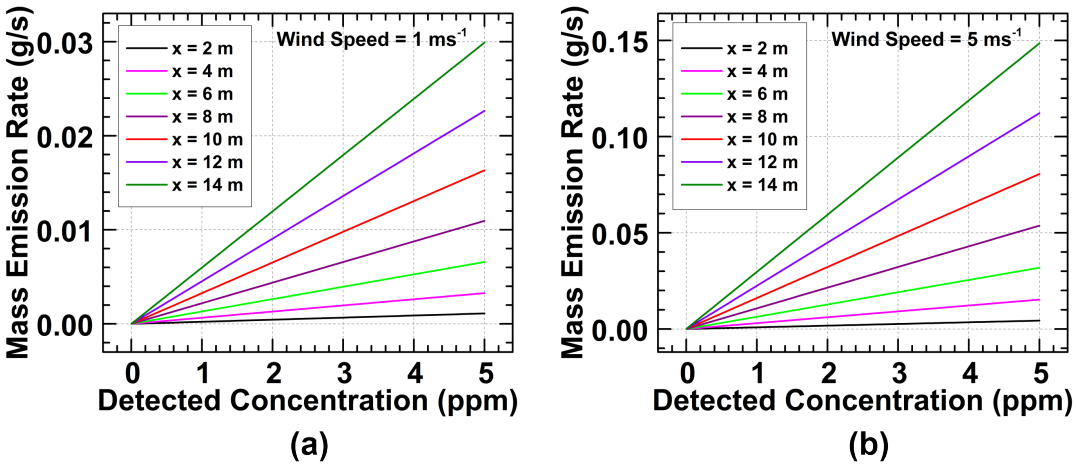

Figure 40: Mass emission rate (g/s) as a function of maximum detected CH_4 concentration (ppm) by a sensor located at different distances from the leak location (2 m – 14 m) along the centerline of the plume. The wind speed was assumed as 1 m/s in (a), and 5 m/s in (b), respectively.

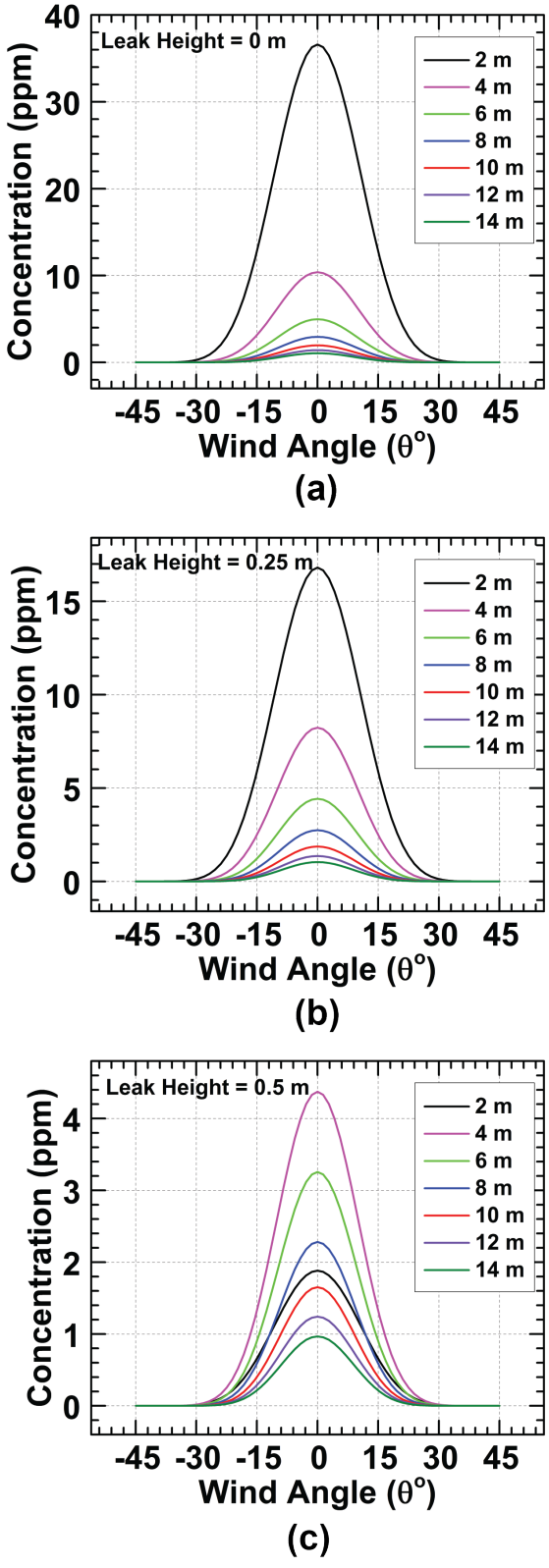

Figure 41: Distribution of CH_4 plume as a function of wind angle for three different leak heights: (a) 0 m, (b) 0.25 m and (c) 0.5 m. The distribution of methane concentration was calculated at different points along the centerline of the plume (2 m – 14 m distances from the leak location). The wind speed is assumed to be 5 m/s. The mass emission rate was assumed to be 0.032 g/s or 6 standard cubic feet per hour (SCFH).

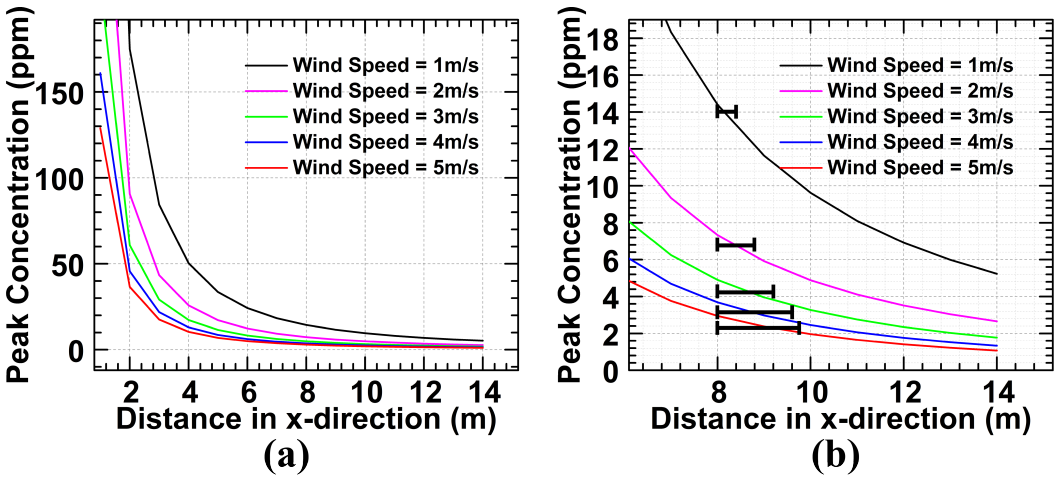

Figure 42: (a) Peak concentration of the plumes at different distances along the centerline (2 m − 14 m) at various wind speeds (1 ms^{-1} − 5 ms^{-1}) (b) Peak concentration of the plumes at different distances along the centerline (7 m 14 m) at various wind speeds (1 ms^{-1} − 5 ms^{-1}). The error bars correspond to uncertainty in distance to sensor due to LDL quantization, assuming an effective LDL of 1 ppm.

CHAPTER 8

CONCLUSIONS

Surface pre-activated MONC-functionalized MWCNT-based chemoresistor sensors were developed which were more able to reproducibly detect 10 ppm of methane in dry air at room temperature. Effective O_2-plasma and UVO-based dry pre-activation techniques have been developed in order to pre-activate the surface of the MWCNT before MONC functionalization. By using ALD, ZnO and SnO_2 NCs were deposited on the pre-activated surface of MWCNT. These MONCs acted as functionalizing materials for the originally inert surface of MWCNTs. MONC-functionalization was found to be essential for reversible, selective, room temperature CH_4 sensing by the MWCNT-based chemoresistor sensor.

The effects of O_2-plasma and UVO-based activation of the MWCNT surface have been studied using characterization tools such as XPS, TEM and Raman spectroscopy. The morphology of the MONC-MWCNTs has been characterized by using SEM and TEM; the chemical composition was characterized by EDS and Raman spectroscopy; the crystal quality was characterized by Raman spectroscopy and TEM. The optical properties of the ZnO NCs have been characterized by PL spectroscopy. These revealed the high crystal quality of the ALD deposited MONC on the surface of the MWCNT, as well as the essential role of the surface pre-activation on the integration of the MONC with the MWCNT.

The principal findings of the research are discussed below:

Principal finding 1: MONC functionalization of MWCNT is essential for the strong relative resistance change in presence of 10 ppm of CH_4 in air at room temperature. TEM and Raman results show that the optimized ALD process produces MONCs with high crystal quality. The crystal quality of the MONCs is ALD temperature dependent. Metal oxides, such as ZnO and SnO_2 are less expensive than previously reported functionalization materials, e.g., Pd. The improved performance of the sensor is a result of (a) strong electron transfer to the MONCs from CH_4 molecules, and (b) energetically favorable electron transport at the MONC-MWCNT junction.

Principal finding 2: Enhanced affinity of the surface pre-activated MWCNT to MONCs, due to formation of active chemical groups, is a key factor for the strong response of the sensors to low ppm CH_4. XPS results show that the O_2 plasma and UVO-based activation processes give rise to COOH, >C=O, and C-OH functional groups on the MWCNT surface; TEM and Raman results show that these groups enhance the nucleation and bonding of MONCs with the MWCNT. Experimental results corroborate the fact that this phenomena contributes to strong reversible relative resistance change of the chemoresistors under iterative exposure to 10 ppm CH_4 in air. Furthermore, compared to the UVO-based technique, the O_2 plasma-based surface pre-activation process was found to be more effective in enhancing sensor response to 10 ppm methane in air mixture.

Principal finding 3: The highest observed response of the MONC-MWCNT sensors to 10 ppm of CH_4 at room temperature was 4 times that of other reported CNT-based CH_4 sensors.

Principal finding 4: A UV-based surface recovery technique enhanced the sensor recovery time by two orders of magnitude compared to our previous result as well as results reported by other researchers.

We also developed a shadow mask based technique which offers resistless electrode fabrication for the MONC-MWCNT chemoresistor sensor, hence providing flexibility in controlling the process temperature during the ALD deposition of the MONCs. This particular fabrication technique will allow high temperature ALD for the MONC-functionalization of MWCNT with excellent crystal quality of the deposited MONCs without degrading the Au electrodes during the ALD. High crystal quality of the functionalizing MONCs is crucial for the long life of the sensor that must perform well under harsh outdoor conditions.

We also proposed a highly sensitive, energy efficient and low-cost distributed methane (CH_4) sensor system (DMSS) for continuous monitoring, detection and localization of CH_4 leaks in natural gas infrastructure such as wells, production pads, transmission and distribution pipelines. The CH_4 sensing element, a key component of the DMSS, consists of a MONC-MWCNT mesh. For the DMSS a Gaussian plume triangulation algorithm has been developed, which, used with a geometric model of the surrounding environment, can precisely detect and localize a CH_4 leak as well as estimate its mass flow rate.

Future Work:

Characterizations:

- Further characterizations of the current and next generation of MONC-MWCNT sensors.

- Examine the response of the MONC-MWCNT sensor to CH_4 as a function of its concentration.
- Study the variability of the response to CH_4 within a set of MONC-MWCNT sensors from the same batch.
- Test the variability of the sensor from batch to batch.
- Examine the lifetime of the sensor.
- Test the response to CH_4 concentrations varying with time.
- Test response to CO_2, CH_4 + CO_2, CH_4 + H_2O, C_2H_6, CH_4 + C_2H_6, C_3H_8, CH_4 + C_3H_8, C_4H_{10}, CH_4 + C_4H_{10}, O_3, CH_4 + O_3, NO_x, and CH_4 + NO_x

Scopes of improvement:

- Obtain faster response to CH_4, i.e., shorter time to show maximum response (so that the sensor response will spike up and spike down when the CH_4 is ON and OFF).
- Obtain lower detection limit.

Furthermore, the MONC-MWCNT chemoresitor CH_4 sensors showed a strong response to RH variation, a potential interference in outdoor CH_4 detection. In general, chemoresistor gas sensors exhibit lack of selectivity to CH_4 in presence of other longer chain hydrocarbons present in natural gas. We proposed a differential grid consisting of selectively functionalized CNT which will be able to selectively detect CH_4 in presence of interference gases by employing constructive/destructive interference resulting from the functional groups different sensitivities

to different hydrocarbons. Differential grid-based chemoresistor sensors can also be employed to determine and nullify the interference caused by variable RH during CH_4 sensing.

In summary, a MONC-MWCNT ppm level CH_4 sensor has been developed. The findings presented in this thesis may help develop CH_4 sensors (a) with higher response to lower concentration of CH_4, and (b) stronger selectivity to CH_4, one of the most important greenhouse gases. Hence, the developed sensor has potential to play an important role in fighting climate change.

APPENDICES

Appendix A

ADDITIONAL INFORMATION ON TEM AND XPS STUDY

A.1 Transmission electron microscope (TEM): sample preparation and imaging

Holey carbon film on Cu grids was used to prepare the TEM samples. MWCNT (98 % pure) with an average diameter of 12 nm, average length of 10 μm and a specific surface area of about 220 m^2/g was purchased from Sigma Aldrich. Using a micro-syringe, an aliquot of 50 μL from a 1 g/50 mL solution of MWCNT-ethanol was deposited on the holey carbon film on Cu grids. It was followed by baking the devices at 75 °C to remove the ethanol and improve adhesion.

The deposited MWCNTs were O_2 plasma treated in a reactive ion etching (RIE) chamber (March plasma CS-1701). The base pressure of the plasma chamber was almost 40 mTorr. O_2 was introduced at a flow rate of 20 standard cubic centimeter per minute (sccm) while the pressure was maintained at 160 mTorr during the process. The O_2 plasma was generated by applying a radio frequency (RF) of 13.56 MHz with a power of 100 watts. The duration of the plasma treatment was 5 min. A UVO cleaner (Nanonex Ultra 100) was used for the UVO treatment of the MWCNT surface, where a vacuum UV (185 nm) was radiated to atmosphere for generating O_3 and activating the MWCNT surface. The process duration was 20 mins. The fabrication steps are illustrated in Figure 4.

Appendix A (Continued)

Using diethylzinc ($(C_2H_5)_2Zn$) as a precursor, ALD of ZnO on the surface pre-treated MWCNTs was performed at 175 °C with an Arradiance Gemstar ALD tool. The pulse duration for DEZ and water vapor was 22 ms and were repeated for 48 cycles. ALD resulted in a deposition of 7.74 nm of ZnO confirmed by TEM.

ALD also was used to integrate SnO_2 NCs with surface pre-treated MWCNTs. The growth was done using an Ultratech Savannah S200. The tetrakis (dimethylamino)tin(IV) was heated to 55 °C and delivered under its own vapor pressure in a 1 s pulse, followed by a 15 s purge, a 0.1 s water dose, and another 15 s purge. This process was repeated for 175 cycles at a growth temperature of 175 °C. ALD resulted in a deposition of SnO_2 NCs with an average diameter of 3.36 nm and confirmed by TEM. Figure 43 illustrates the ALD of MONCs on the MWCNT surface.

A JEOL 2100F TEM operated at 200 kV was used to characterize atomic scale morphology and crystal quality of the MONCs deposited on MWCNT surfaces.

A.2 XPS sample preparation

A gold thin film (20 nm) was deposited on clean Si wafer using electron beam evaporation. Using a micro-syringe, an aliquot of relatively higher density (compared to the one used for device fabrication) solution (1 mg/1 μL) of MWCNT-ethanol was deposited on the Au-coated Si wafers. It was followed by baking the devices at 75 °C to remove the ethanol and improve adhesion. MWCNTs were surface activated a similar manner as described in Section A.1 (5 min O_2 plasma or 20 mins UVO).

Appendix A (Continued)

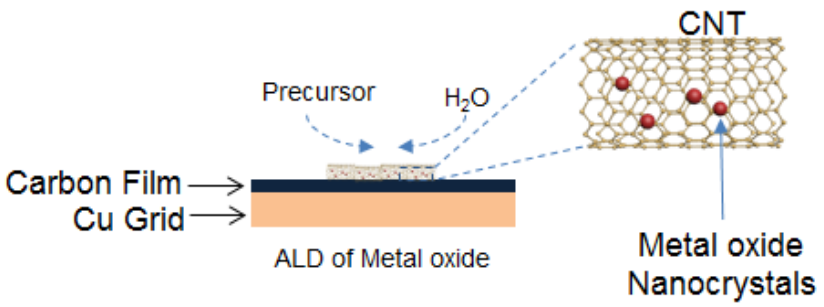

Figure 43: TEM sample preparation. Atomic layer deposition of metal oxide nanocrystals on pre-activated MWCNT surface.

Appendix B

MORPHOLOGY OF THE GOLD METAL PADS AFTER HIGH TEMPERATURE ALD AND SHADOW MASK BASED ALTERNATIVE FABRICATION APPROACH

Results in chapter 3 showed that as the ZnO ALD temperature increases the crystal quality of the ZnO NCs on the MWCNT surface is enhanced. Superior crystal quality of the functionalizing ZnO NCs enhances the electron transport in the ZnO-MWCNT junction (34) thus has positive impact on the sensor performance with respect to relative resistance change, i.e., sensitivity. It is important to ensure the chemical stability and robustness of the functionalizing material so that the sensor operates accurately in harsher environments(26). High crystal quality of the functionalizing NCs helps minimize cross-response and optimize reversibility as the sensor ages (26; 62).

SEM characterization (Figure 44) demonstrated that at high temperature ALD (225 °C), Au acts as catalyst to produce "nanorod"-shaped ZnO structures on top of the electrodes of the ZnO-MWCNT sensor. Atomic force microscopy (Figure 45) shows the evolution of the Au electrode's surface roughness as a result of increasing ALD temperature. Figure 45a shows the AFM image of an untreated Au pad. Figure 45b, c, and d show AFM images of Au pads after subjected to ZnO-ALD at 175, 200 and 225 °C, respectively. Surface roughness of the Au metal electrodes significantly increased due to high temperature ALD; hence the adhesiveness of the

Appendix B (Continued)

Au metal pads to external metal wires degrades significantly as well. The phenomenon is also illustrated in Figure 12. Consequently, we were only able to test the sensitivity of 175 °C ALD samples.

A shadow mask-based technique to overcome this issue is being developed. Figure 46a illustrates the process flow chart used to fabricate silicon on insulator (SOI)-based shadow mask. Figure 46b shows a fabricated shadow mask. The shadow mask based technique offers a resist-less alternative electrode fabrication process for the MONC-MWCNT chemoresistor sensor. Without affecting the quality of the Au electrodes during the ALD process, this fabrication technique will allow high temperature ALD for the MONC-functionalization of MWCNT with excellent crystal quality of the deposited MONCs.

Appendix B (Continued)

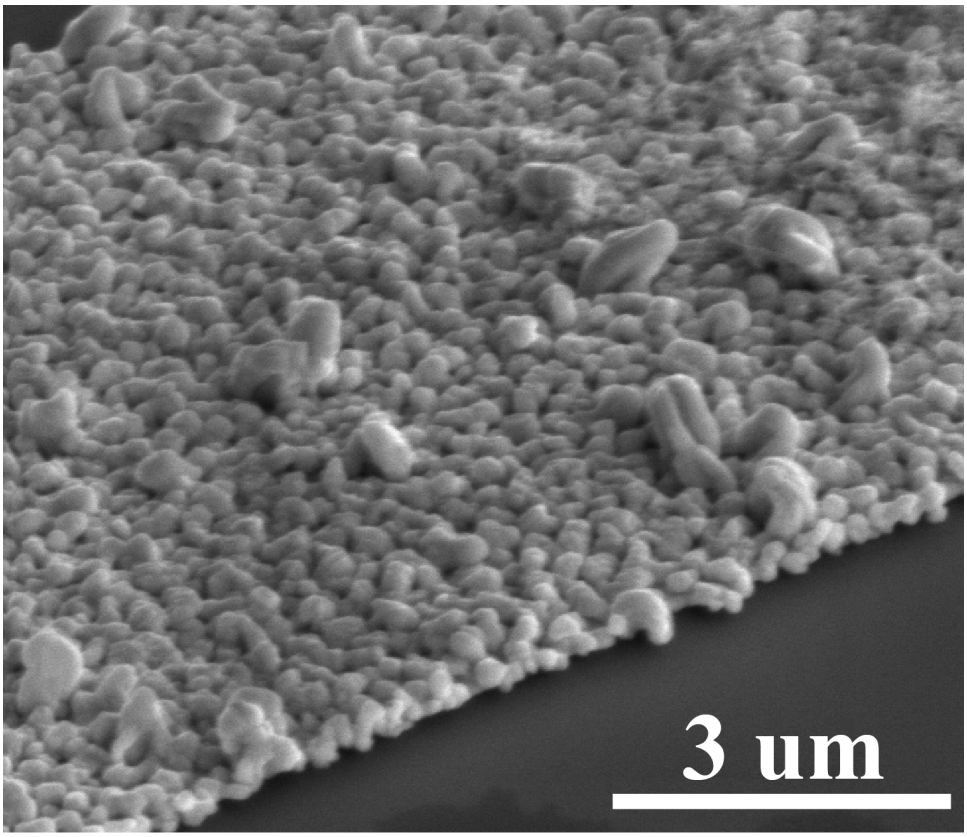

Figure 44: SEM image of the Au electrode after 225 °C ALD. ZnO "nanorods" are clearly visible on the Au surface. This phenomenon significantly degrades the adhesiveness of the Au metal pads.

Appendix B (Continued)

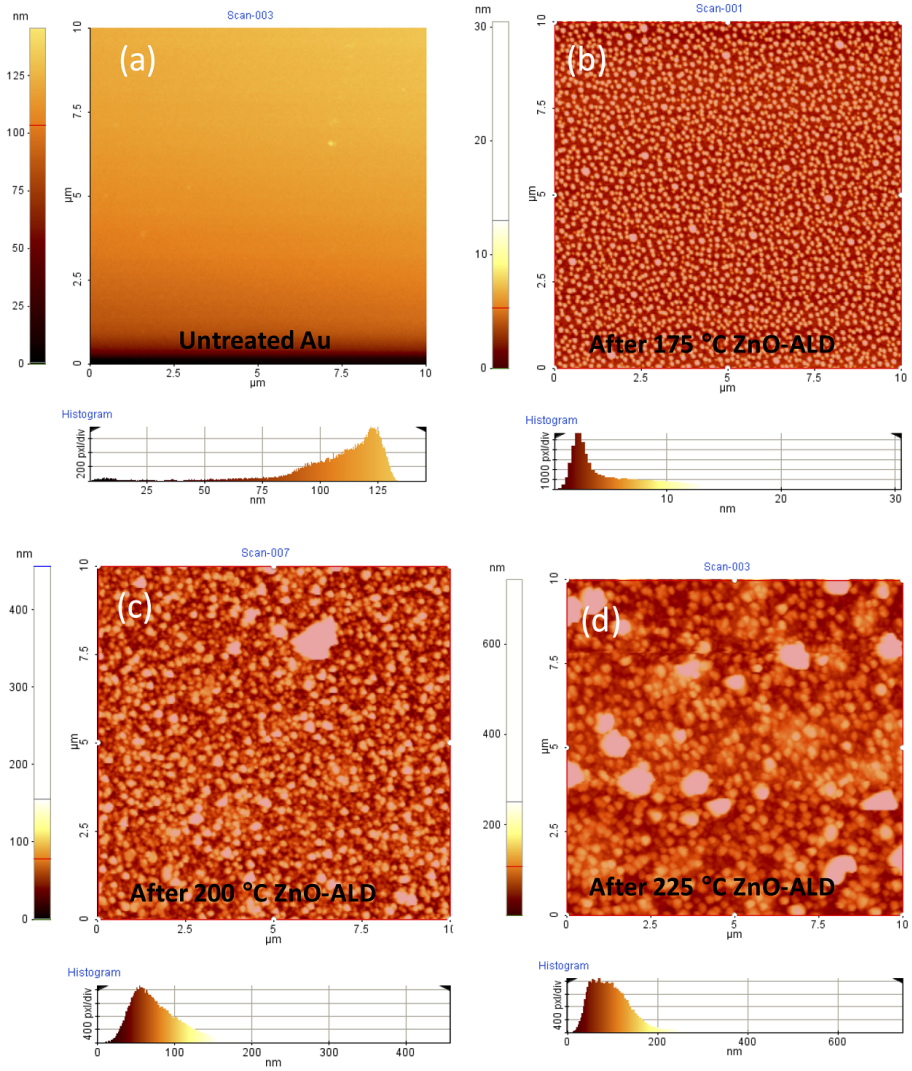

Figure 45: AFM image illustrating the evolution of the roughness of Au metal pads resulting from different ALD temperatures.

Appendix B (Continued)

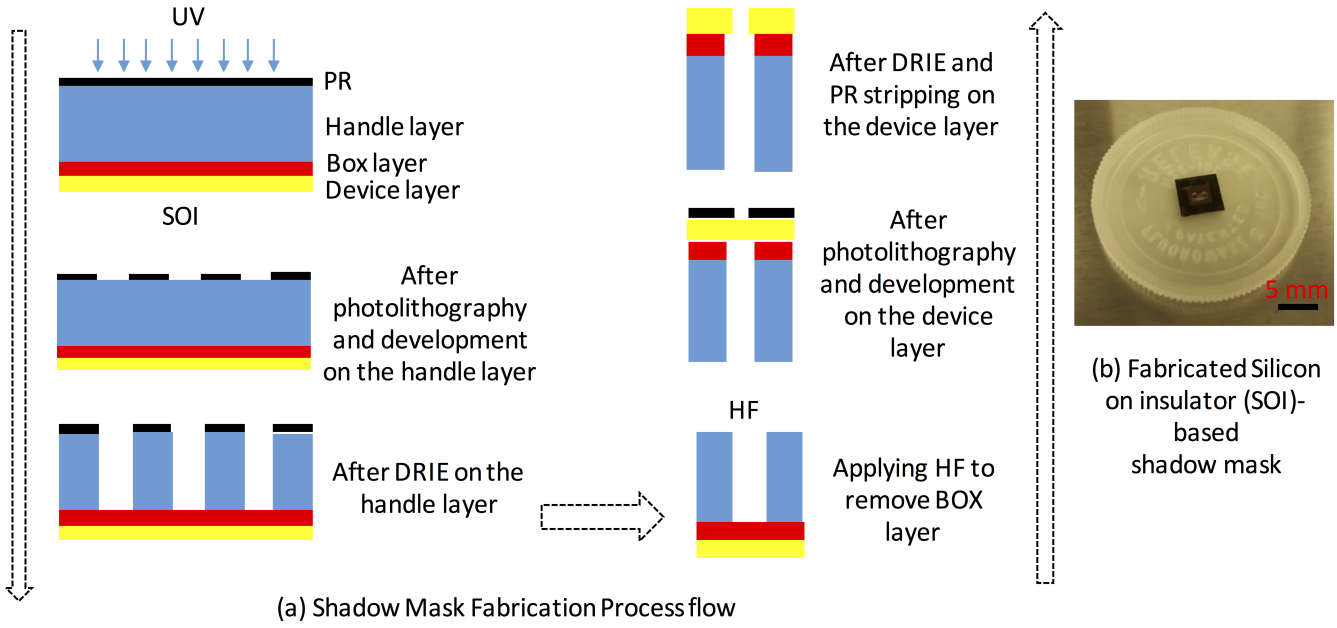

Figure 46: (a) Silicon on insulator (SOI)-based shadow mask fabrication steps. (b) An optical image of a fabricated shadow mask.

Appendix C

THESIS / DISSERTATION REUSE GUIDELINES: IEEE

Thesis / Dissertation Reuse

The IEEE does not require individuals working on a thesis to obtain a formal reuse license, however, you may print out this statement to be used as a permission grant:

Requirements to be followed when using any portion (e.g., figure, graph, table, or textual material) of an IEEE copyrighted paper in a thesis:

1) In the case of textual material (e.g., using short quotes or referring to the work within these papers) users must give full credit to the original source (author, paper, publication) followed by the IEEE copyright line © 2011 IEEE. 2) In the case of illustrations or tabular material, we require that the copyright line © [Year of original publication] IEEE appear prominently with each reprinted figure and/or table. 3) If a substantial portion of the original paper is to be used, and if you are not the senior author, also obtain the senior authors approval.

Requirements to be followed when using an entire IEEE copyrighted paper in a thesis:

1) The following IEEE copyright/ credit notice should be placed prominently in the references: © [year of original publication] IEEE. Reprinted, with permission, from [author names, paper title, IEEE publication title, and month/year of publication] 2) Only the accepted version of an IEEE copyrighted paper can be used when posting the paper or your thesis on-line. 3) In placing the thesis on the author's university website, please display the following message in a prominent place on the website: In reference to IEEE copyrighted material which is used with

Appendix C (Continued)

permission in this thesis, the IEEE does not endorse any of [university/educational entity's name goes here]'s products or services. Internal or personal use of this material is permitted. If interested in reprinting/republishing IEEE copyrighted material for advertising or promotional purposes or for creating new collective works for resale or redistribution, please go to `http://www.ieee.org/publications_standards/publications/rights/rights_link.html` to learn how to obtain a License from RightsLink.

If applicable, University Microfilms and/or ProQuest Library, or the Archives of Canada may supply single copies of the dissertation.

Appendix D

THESIS / DISSERTATION REUSE GUIDELINES: AMERICAN INSTITUTE OF PHYSICS (AIP)

Copyright and Permission to Reuse AIP Material

"AIP permits authors to include their published articles in a thesis or dissertation. It is understood that the thesis or dissertation may be published in print and/or electronic form and offered for sale, as well as included in a universitys repository. Formal permission from AIP is not needed. If the university requires written permission, however, we are happy to supply it." Please see Figure 47.

Also consult: https://publishing.aip.org/authors/copyright-reuse

Appendix D (Continued)

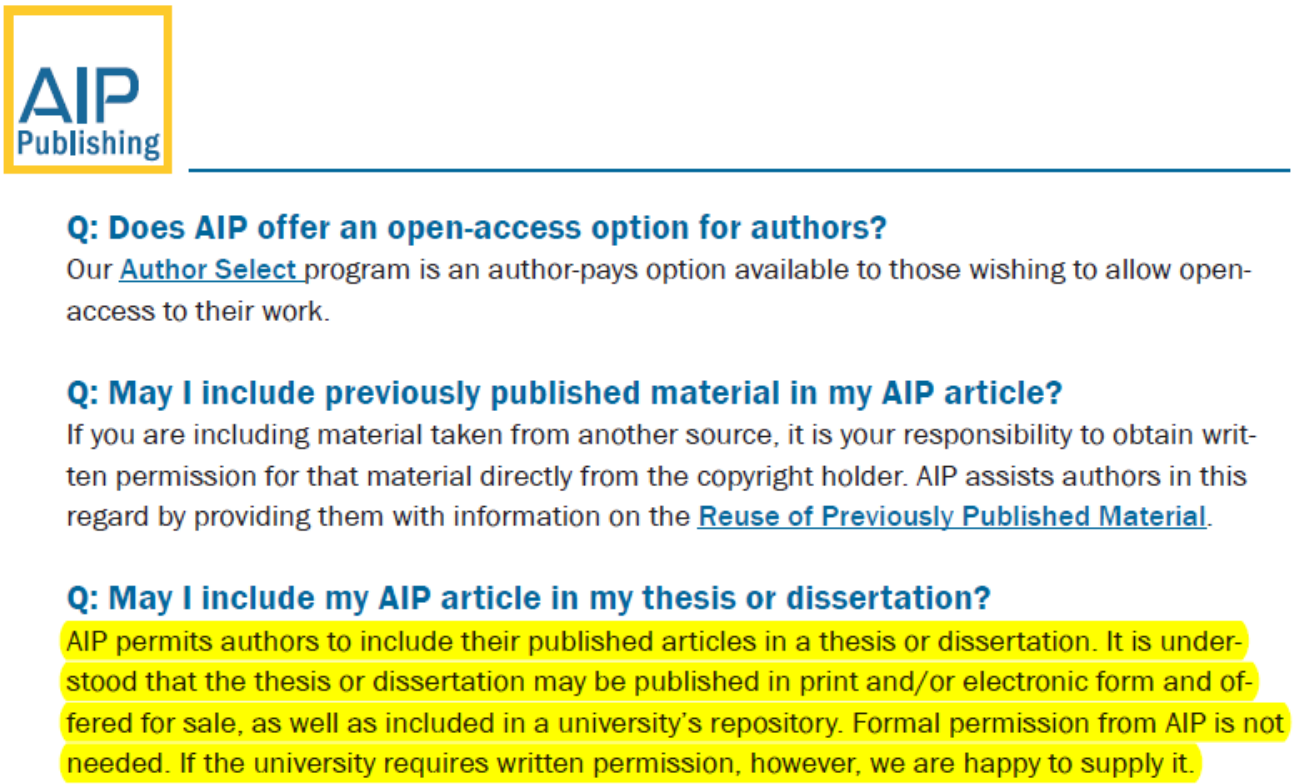

Figure 47: Copyright and Permission to Reuse AIP Material FAQ.

CITED LITERATURE

1. Climate Change 2007: Working Group I: The Physical Science Basis. `http://www.ipcc.ch/publications_and_data/ar4/wg1/en/ch2s2-10-2.html`. Accessed: 2016-01-17.

2. Overview of Greenhouse Gases. `http://epa.gov/climatechange/ghgemissions/Gases/ch4.html`. Accessed: 2015-09-02.

3. Thompson, D., Leifer, I., Bovensmann, H., Eastwood, M., Fladeland, M., Frankenberg, C., GeriLowski, K., Green, R., Kratwurst, S., Krings, T., et al.: Real-time Remote Detection and Measurement for Airborne Imaging Spectroscopy: a Case Study with Methane. Atmospheric Measurement Techniques, 8(10):4383–4397, 2015.

4. Massie, C., Stewart, G., McGregor, G., and Gilchrist, J. R.: Design of a Portable Optical Sensor for Methane Gas Detection. Sensors and Actuators B: Chemical, 113(2):830–836, February 2006.

5. Lai, W.-C., Chakravarty, S., Wang, X., Lin, C., and Chen, R. T.: On-chip Methane Sensing by Near-IR Absorption Signatures in a Photonic Crystal Slot Waveguide. Optics Letters, 36(6):984–986, 2011.

6. Nadezhdinskii, A., Berezin, A., Chernin, S., Ershov, O., and Kutnyak, V.: High Sensitivity Methane Analyzer Based on Tuned Near Infrared Diode Laser. Spectrochimica Acta Part A: Molecular and Biomolecular Spectroscopy, 55(10):2083–2089, 1999.

7. Krier, A. and Sherstnev, V.: Powerful Interface Light Emitting Diodes for Methane Gas Detection. Journal of Physics D: Applied Physics, 33(2):101–106, January 2000.

8. Wang, C., Crowder, J., Mannheim, V., Ashley, T., Dutton, D., Johnson, A., Pryce, G., and Smith, S.: Detection of Nitrogen Dioxide Using a Room Temperature Operation Mid-infrared InSb Light Emitting Diode. Electronics Letters, 34(3):300–301, February 1998.

9. Rella, C., Hoffnagle, J., He, Y., and Tajima, S.: Local and Regional Scale Measurements of CH_4, $\delta^{13}CH_4$, and C_2H_6 in the Uintah Basin Using a Mobile Stable Isotope Analyzer. 2015.

10. Roscioli, J., Yacovitch, T., Floerchinger, C., Mitchell, A., Tkacik, D., Subramanian, R., Martinez, D., Vaughn, T., Williams, L., Zimmerle, D., et al.: Measurements of Methane Emissions from Natural Gas Gathering Facilities and Processing Plants: Measurement Methods. Atmospheric Measurement Techniques, 8(5):2017–2035, 2015.

11. Jahjah, M., Ren, W., Stefański, P., Lewicki, R., Zhang, J., Jiang, W., Tarka, J., and Tittel, F. K.: A Compact QCL Based Methane and Nitrous Oxide Sensor for Environmental and Medical Applications. Analyst, 139(9):2065–2069, 2014.

12. Measurement of the Carbon Isotopic Ratio of Atmospheric Methane. `http://cfpub.epa.gov/ncer_abstracts/index.cfm/fuseaction/display.abstractDetail/abstract/6351/report/0`. Accessed: 2016-01-17.

13. Otagawa, T., Zaromb, S., and Stetter, J. R.: Electrochemical Oxidation of Methane in Nonaqueous Electrolytes at Room Temperature Application to Gas Sensors. Journal of the Electrochemical Society, 132(12):2951–2957, August 1985.

14. Comparison of Gas Detection Technologies. `http://global-controls.net/home/pdfs/OI_Analytical/SAM-MAX_Gas_Detection_Technologies.pdf`. Accessed: 2016-03-14.

15. Barreca, D., Bekermann, D., Comini, E., Devi, A., Fischer, R. A., Gasparotto, A., Maccato, C., Sberveglieri, G., and Tondello, E.: 1D ZnO Nano-assemblies by Plasma-CVD as Chemical Sensors for Flammable and Toxic Gases. Sensors and Actuators B: Chemical, 149(1):1–7, August 2010.

16. Fau, P., Sauvan, M., Trautweiler, S., Nayral, C., Erades, L., Maisonnat, A., and Chaudret, B.: Nanosized Tin Oxide Sensitive Layer on a Silicon Platform for Domestic Gas Applications. Sensors and Actuators B: Chemical, 78(1):83–88, August 2001.

17. Waitz, T., Wagner, T., Sauerwald, T., Kohl, C.-D., and Tiemann, M.: Ordered Mesoporous In_2O_3: Synthesis by Structure Replication and Application as a Methane Gas Sensor. Advanced Functional Materials, 19(4):653–661, February 2009.

18. Morrison, S. R.: Selectivity in Semiconductor Gas Sensors. Sensors and Actuators, 12(4):425–440, November-December 1987.

19. Gopel, W.: Chemisorption and Charge Transfer at Ionic Semiconductor Surfaces: Implications in Designing Gas Sensors. Progress in Surface Science, 20(1):9–103, 1985.

20. Butta, N., Cinquegrani, L., Mugno, E., Tagliente, A., and Pizzini, S.: A Family of Tin Oxide-Based Sensors with Improved Selectivity to Methane. Sensors and Actuators B: Chemical, 6(1):253–256, 1992.

21. Lee, D.-D., Chung, W.-Y., and Sohn, B.-K.: High Sensitivity and Selectivity Methane Gas Sensors Doped with Rh as a Catalyst. Sensors and Actuators B: Chemical, 13(1):252–255, 1993.

22. Quaranta, F., Rella, R., Siciliano, P., Capone, S., Epifani, M., Vasanelli, L., Licciulli, A., and Zocco, A.: A novel Gas Sensor Based on SnO_2/Os thin film for the Detection of Methane at Low Temperature. Sensors and Actuators B: Chemical, 58(1):350–355, 1999.

23. Choi, S.-D. and Lee, D.-D.: CHH_4 Sensing Characteristics of K-, Ca-, Mg Impregnated SnO_2 Sensors. Sensors and Actuators B: Chemical, 77(1):335–338, 2001.

24. Iijima, S. et al.: Helical Microtubules of Graphitic Carbon. Nature, 354(6348):56–58, November 1991.

25. Dresselhaus, M., Dresselhaus, G., and Saito, R.: Physics of Carbon Nanotubes. Carbon, 33(7):883–891, December 1995.

26. Zhang, T., Mubeen, S., Myung, N. V., and Deshusses, M. A.: Recent Progress in Carbon Nanotube-Based Gas Sensors. Nanotechnology, 19(33):332001, July 2008.

27. Lu, Y., Li, J., Han, J., Ng, H.-T., Binder, C., Partridge, C., and Meyyappan, M.: Room Temperature Methane Detection Using Palladium Loaded Single-walled Carbon Nanotube Sensors. Chemical Physics Letters, 391(4):344–348, June 2004.

28. Lu, G., Ocola, L. E., and Chen, J.: Room-temperature Gas Sensing Based on Electron Transfer between Discrete Tin Oxide Nanocrystals and Multiwalled Carbon Nanotubes. Advanced Materials, 21(24):2487–2491, June 2009.

29. Peigney, A., Laurent, C., Flahaut, E., Bacsa, R., and Rousset, A.: Specific Surface Area of Carbon Nanotubes and Bundles of Carbon Nanotubes. Carbon, 39(4):507–514, April 2001.

30. Kumar, M. K. and Ramaprabhu, S.: Nanostructured Pt Functionlized Multiwalled Carbon Nanotube Based Hydrogen Sensor. The Journal of Physical Chemistry B, 110(23):11291–11298, June 2006.

31. Kong, J., Chapline, M. G., and Dai, H.: Functionalized Carbon Nanotubes for Molecular Hydrogen Sensors. Advanced Materials, 13(18):1384–1386, September 2001.

32. Staii, C., Johnson, A. T., Chen, M., and Gelperin, A.: DNA-Decorated Carbon Nanotubes for Chemical Sensing. Nano Letters, 5(9):1774–1778, September 2005.

33. Qi, P., Vermesh, O., Grecu, M., Javey, A., Wang, Q., Dai, H., Peng, S., and Cho, K.: Toward Large Arrays of Multiplex Functionalized Carbon Nanotube Sensors for Highly Sensitive and Selective Molecular Detection. Nano Letters, 3(3):347–351, March 2003.

34. Zhang, H., Du, N., Chen, B., Li, D., and Yang, D.: Carbon Nanotube-ZnO Nanosphere Heterostructures: Low-temperature Chemical Reaction Synthesis, Photoluminescence, and their Application for Room Temperature NH_3 Gas Sensor. Science of Advanced Materials, 1(1):13–17, April 2009.

35. Moormann, H., Kohl, D., and Heiland, G.: Work Function and Band Bending on Clean Cleaved Zinc Oxide Surfaces. Surface Science, 80:261–264, February 1979.

36. Bai, X., Wang, E. G., Gao, P., and Wang, Z. L.: Measuring the Work Function at a Nanobelt Tip and at a Nanoparticle Surface. Nano Letters, 3(8):1147–1150, August 2003.

37. Shiraishi, M. and Ata, M.: Work Function of Carbon Nanotubes. Carbon, 39(12):1913–1917, October 2001.

38. Varghese, O., Kichambre, P., Gong, D., Ong, K., Dickey, E., and Grimes, C.: Gas Sensing Characteristics of Multi-wall Carbon Nanotubes. Sensors and Actuators B: Chemical, 81(1):32–41, December 2001.

39. Li, X., Li, C., Zhang, Y., Chu, D., Milne, W., and Fan, H.: Atomic Layer Deposition of ZnO on Multi-walled Carbon Nanotubes and Its Use for Synthesis of CNT–ZnO Heterostructures. Nanoscale Research Letters, 5(11):1836–1840, November 2010.

40. Zamudio, A., Elías, A. L., Rodríguez-Manzo, J. A., López-Urías, F., Rodríguez-Gattorno, G., Lupo, F., Rühle, M., Smith, D. J., Terrones, H., Díaz, D., et al.: Efficient Anchoring of Silver Nanoparticles on N-doped Carbon Nanotubes. Small, 2(3):346–350, March 2006.

41. Utegulov, Z. N., Mast, D. B., He, P., Shi, D., and Gilland, R. F.: Functionalization of Single-walled Carbon Nanotubes Using Isotropic Plasma Treatment: Resonant Raman Spectroscopy Study. Journal of Applied Physics, 97(10):104324, May 2005.

42. Yang, D.-Q. and Sacher, E.: Strongly Enhanced Interaction between Evaporated Pt Nanoparticles and Functionalized Multiwalled Carbon Nanotubes via Plasma Surface Modifications: Effects of Physical and Chemical Defects. The Journal of Physical Chemistry C, 112(11):4075–4082, March 2008.

43. Felten, A., Bittencourt, C., Pireaux, J.-J., Van Lier, G., and Charlier, J.-C.: Radio-Frequency Plasma Functionalization of Carbon Nanotubes Surface O2, NH3, and CF4 Treatments. Journal of Applied Physics, 98(7):074308, October 2005.

44. Najafi, E., Kim, J.-Y., Han, S.-H., and Shin, K.: UV-ozone Treatment of Multi-walled Carbon Nanotubes for Enhanced Organic Solvent Dispersion. Colloids and Surfaces A: Physicochemical and Engineering Aspects, 284:373–378, August 2006.

45. Espinosa, E., Ionescu, R., Bittencourt, C., Felten, A., Erni, R., Van Tendeloo, G., Pireaux, J.-J., and Llobet, E.: Metal-decorated Multi-wall Carbon Nanotubes for Low Temperature Gas Sensing. Thin Solid Films, 515(23):8322–8327, September 2007.

46. Kar, P. and Choudhury, A.: Carboxylic Acid Functionalized Multi-walled Carbon Nanotube Doped Polyaniline for Chloroform Sensors. Sensors and Actuators B: Chemical, 183:25–33, July 2013.

47. Kim, J. C., Jun, H. K., Huh, J.-S., and Lee, D. D.: Tin Oxide-Based Methane Gas Sensor Promoted by Alumina-supported Pd Catalyst. Sensors and Actuators B: Chemical, 45(3):271–277, December 1997.

48. Min, B.-K. and Choi, S.-D.: SnO_2 Thin Film Gas Sensor Fabricated by Ion Beam Deposition. Sensors and Actuators B: Chemical, 98(2):239–246, March 2004.

49. Bhattacharyya, P., Basu, P., Mondal, B., and Saha, H.: A Low power MEMS Gas Sensor Based on Nanocrystalline ZnO thin Films for Sensing Methane. Microelectronics Reliability, 48(11):1772–1779, December 2008.

50. Basu, P., Jana, S., Saha, H., and Basu, S.: Low Temperature Methane sensing by Electrochemically Grown and Surface Modified ZnO Thin Films. Sensors and Actuators B: Chemical, 135(1):81–88, July 2008.

51. Li, Z., Li, J., Wu, X., Shuang, S., Dong, C., and Choi, M. M.: Methane Sensor Based on Nanocomposite of Palladium/Multi-walled Carbon Nanotubes Grafted with 1, 6-Hexanediamine. Sensors and Actuators B: Chemical, 139(2):453–459, June 2009.

52. Roy, R., Chowdhury, M. P., and Pal, A.: Room Temperature Sensor Based on Carbon Nanotubes and Nanofibres for Methane Detection. Vacuum, 77(3):223–229, February 2005.

53. Willinger, M.-G., Neri, G., Rauwel, E., Bonavita, A., Micali, G., and Pinna, N.: Vanadium Oxide Sensing Layer Grown on Carbon Nanotubes by a New Atomic Layer Deposition Process. Nano Letters, 8(12):4201–4204, October 2008.

54. Boukhalfa, S., Evanoff, K., and Yushin, G.: Atomic Layer Deposition of Vanadium Oxide on Carbon Nanotubes for High-power Supercapacitor Electrodes. Energy & Environmental Science, 5(5):6872–6879, February 2012.

55. Bhattacharyya, P., Basu, P., Saha, H., and Basu, S.: Fast Response Methane Sensor Using Nanocrystalline Zinc Oxide Thin Films Derived by Sol–gel Method. Sensors and Actuators B: Chemical, 124(1):62–67, July 2007.

56. Application Notes TGS 2611, Figaro Engineering Inc., Japan. `http://www.datasheetarchive.com/dlmain/Datasheets-11/DSA-218253.pdf`. Accessed: 2015-09-21.

57. Park, H., Afzali, A., Han, S.-J., Tulevski, G. S., Franklin, A. D., Tersoff, J., Hannon, J. B., and Haensch, W.: High-density Integration of Carbon Nanotubes via Chemical Self-assembly. Nature Nanotechnology, 7(12):787–791, 2012.

58. Bindu, P. and Thomas, S.: Estimation of Lattice Strain in ZnO Nanoparticles: X-ray Peak Profile Analysis. Journal of Theoretical and Applied Physics, 8(4):123–134, December 2014.

59. Zhu, Y., Elim, H. I., Foo, Y.-L., Yu, T., Liu, Y., Ji, W., Lee, J.-Y., Shen, Z., Wee, A. T.-S., Thong, J. T.-L., et al.: Multiwalled Carbon Nanotubes Beaded with ZnO Nanoparticles for Ultrafast Nonlinear Optical switching. Advanced Materials, 18(5):587–592, 2006.

60. Cuscó, R., Alarcón-Lladó, E., Ibáñez, J., Artús, L., Jiménez, J., Wang, B., and Callahan, M. J.: Temperature Dependence of Raman Scattering in ZnO. Physical Review B, 75(16):165202, April 2007.

61. Alim, K. A., Fonoberov, V. A., Shamsa, M., and Balandin, A. A.: Micro-Raman Investigation of Optical Phonons in ZnO Nanocrystals. Journal of Applied Physics, 97(12):124313–124313, June 2005.

62. Sayago, I., Terrado, E., Aleixandre, M., Horrillo, M., Fernández, M., Lozano, J., Lafuente, E., Maser, W., Benito, A., Martinez, M., et al.: Novel Selective Sensors Based on Carbon Nanotube Films for Hydrogen Detection. Sensors and Actuators B: Chemical, 122(1):75–80, June 2007.

63. Khanderi, J., Hoffmann, R. C., Gurlo, A., and Schneider, J. J.: Synthesis and Sensoric Response of ZnO decorated Carbon Nanotubes. Journal of Materials Chemistry, 19(28):5039–5046, June 2009.

64. Albiss, B., Sakhaneh, W., Jumah, I., Obaidat, I. M., et al.: Gas Sensing Properties of ZnO/Single-Wall Carbon Nanotube Composites. Sensors Journal, IEEE, 10(12):1807–1812, December 2010.

65. Lupan, O., Chai, G., and Chow, L.: Novel Hydrogen Gas Sensor Based on Single ZnO Nanorod. Microelectronic Engineering, 85(11):2220–2225, July 2008.

66. Lee, D.-D., Chung, W.-Y., and Sohn, B.-K.: High Sensitivity and Selectivity Methane Gas Sensors Doped with Rh as a Catalyst. Sensors and Actuators B: Chemical, 13(1):252–255, May 1993.

67. Nitta, M. and Haradome, M.: CO Gas Detection by ThO_2-Doped SnO_2. Journal of Electronic Materials, 8(5):571–580, September 1979.

68. Quaranta, F., Rella, R., Siciliano, P., Capone, S., Epifani, M., Vasanelli, L., Licciulli, A., and Zocco, A.: A Novel Gas Sensor Based On SnO_2 Thin Film for the Detection of Methane at Low Temperature. Sensors and Actuators B: Chemical, 58(1):350–355, September 1999.

69. Liu, Y.-L., Yang, H.-F., Yang, Y., Liu, Z.-M., Shen, G.-L., and Yu, R.-Q.: Gas Sensing Properties of Tin Dioxide Coated onto Multi-walled Carbon Nanotubes. Thin Solid Films, 497(1):355–360, February 2006.

70. Zhou, J., Fang, H., Maley, J., Ko, J., Murphy, M., Chu, Y., Sammynaiken, R., and Sham, T.: An X-ray Absorption, Photoemission, and Raman Study of the Interaction Between SnO_2 Nanoparticle and Carbon Nanotube. The Journal of Physical Chemistry C, 113(15):6114–6117, March 2009.

71. Zhang, H.-X., Feng, C., Zhai, Y.-C., Jiang, K.-L., Li, Q.-Q., and Fan, S.-S.: Cross-Stacked Carbon Nanotube Sheets Uniformly Loaded with SnO_2 Nanoparticles: A Novel Binder-Free and High-Capacity Anode Material for Lithium-Ion Batteries. Advanced Materials, 21(22):2299–2304, June 2009.

72. Elam, J. W., Baker, D. A., Hryn, A. J., Martinson, A. B., Pellin, M. J., Hupp, J. T., et al.: Atomic Layer Deposition of Tin Oxide Films Using Tetrakis (Dimethylamino) Tin. Journal of vacuum science & technology. A. Vacuum, Surfaces, and films, 26(2):244, March 2008.

73. Functionalization of Suspended Carbon Nanotubes in Silicon Microsystems by Atomic Layer Deposition (ALD).

74. Elam, J. W., Baker, D. A., Martinson, A. B., Pellin, M. J., and Hupp, J. T.: Atomic Layer Deposition of Indium Tin Oxide Thin Films Using Nonhalogenated Precursors. The Journal of Physical Chemistry C, 112(6):1938–1945, February 2008.

75. Antunes, E., Lobo, A., Corat, E., and Trava-Airoldi, V.: Influence of Diameter in the Raman Spectra of Aligned Multi-walled Carbon Nanotubes. Carbon, 45(5):913–921, April 2007.

76. Chen, C., Liang, B., Ogino, A., Wang, X., and Nagatsu, M.: Oxygen Functionalization of Multiwall Carbon Nanotubes by Microwave-excited Surface-wave Plasma Treatment. The Journal of Physical Chemistry C, 113(18):7659–7665, April 2009.

77. Mcguire, K., Pan, Z., Wang, Z., Milkie, D., Menendez, J., and Rao, A.: Raman Studies of Semiconducting Oxide Nanobelts. Journal of Nanoscience and Nanotechnology, 2(5):499–502, October 2002.

78. Dieguez, A., Romano-Rodrıguez, A., Vila, A., and Morante, J.: The Complete Raman Spectrum of Nanometric SnO_2 Particles. Journal of Applied Physics, 90(3):1550–1557, August 2001.

79. Li, Y., Wang, H., Chen, Y., and Yang, M.: A Multi-walled Carbon Nanotube/Palladium Nanocomposite Prepared by a Facile Method for the Detection of Methane at Room Temperature. Sensors and actuators B: Chemical, 132(1):155–158, May 2008.

80. Larciprete, R., Gardonio, S., Petaccia, L., and Lizzit, S.: Atomic Oxygen Functionalization of Double Walled C Nanotubes. Carbon, 47(11):2579–2589, September 2009.

81. Ganguly, A., Sharma, S., Papakonstantinou, P., and Hamilton, J.: Probing the Thermal Deoxygenation of Graphene Oxide Using High-resolution In Situ X-ray-based Spectroscopies. The Journal of Physical Chemistry C, 115(34):17009–17019, August 2011.

82. Surface Functionalization of Graphite and Carbon Nanotubes by Vacuum-Ultraviolet Photochemical Reactions.

83. Zielke, U., Hüttinger, K., and Hoffman, W.: Surface-Oxidized Carbon Fibers: Surface Structure and Chemistry. Carbon, 34(8):983–998, January 1996.

84. Humayun, M. T., Divan, R., Stan, L., Gupta, A., Rosenmann, D., Gundel, L., Solomon, P. A., and Paprotny, I.: ZnO Functionalization of Multiwalled Carbon Nanotubes for Methane Sensing at Single Parts Per Million Concentration Levels. Journal of Vacuum Science & Technology B, 33(6):06FF01, November 2015.

85. Kim, D., Lee, S.-M., Scholz, R., Knez, M., Gösele, U., Fallert, J., Kalt, H., and Zacharias, M.: Synthesis and Optical Properties of ZnO and Carbon Nanotube Based Coaxial Heterostructures. Applied Physics Letters, 93(10):103108, 2008.

86. Leiter, F., Alves, H., Hofstaetter, A., Hofmann, D., and Meyer, B.: The Oxygen Vacancy as the Origin of a Green Emission in Undoped ZnO. Physica Status Solidi (B), 226(1):R4–R5, 2001.

87. Zeferino, R. S., Flores, M. B., and Pal, U.: Photoluminescence and Raman scattering in Ag-doped ZnO Nanoparticles. Journal of Applied Physics, 109(1):014308, 2011.

88. National Wind Technology Center, NWTC M2 Tower, National Renewable Energy Laboratory. `http://www.nrel.gov/midc/nwtc_m2`. Accessed: 2015-09-02.

89. J. H. Seinfeld, S. N. P.: Atmospheric Chemistry and Physics: From Air Pollution to Climate Change. John Willey and Sons, second edition, 2006.

90. Humayun, M. T., Divan, R., Liu, Y., Gundel, L., Solomon, P. A., and Paprotny, I.: Novel Chemoresistive CH4 Sensor with 10 ppm Sensitivity Based on Multiwalled Carbon Nanotubes Functionalized with SnO_2 Nanocrystals. Journal of Vacuum Science & Technology A, 34(1):01A131, 2016.

91. Aasmundtveit, K. E., Ta, B. Q., Nguyen, Q.-H., Haugen, T. B., Hoivik, N., and Halvorsen, E.: Local Synthesis of Carbon Nanotubes for Direct Integration in Si Microsystems–Design Considerations. Advances in Manufacturing, 1(3):218–225, September 2013.

92. Heinze, S., Tersoff, J., Martel, R., Derycke, V., Appenzeller, J., and Avouris, P.: Carbon Nanotubes as Schottky Barrier Transistors. Physical Review Letters, 89(10):106801, August 2002.

93. Penza, M., Rossi, R., Alvisi, M., and Serra, E.: Metal-modified and Vertically Aligned Carbon Nanotube Sensors Array for Landfill Gas Monitoring Applications. Nanotechnology, 21(10):105501, March 2010.

94. Star, A., Joshi, V., Skarupo, S., Thomas, D., and Gabriel, J.-C. P.: Gas Sensor Array Based on Metal-decorated Carbon Nanotubes. The Journal of Physical Chemistry B, 110(42):21014–21020, October 2006.

95. Biaggi-Labiosa, A., Solá, F., Lebrón-Colón, M., Evans, L., Xu, J., Hunter, G., Berger, G., and González, J.: A Novel Methane Sensor Based on Porous SnO_2 Nanorods: Room Temperature to High Temperature Detection. Nanotechnology, 23(45):455501, November 2012.

VITA

MD TANIM HUMAYUN

PROFILE

Electrical engineer with expertise in nanoscale device design, fabrication and characterization with emphasis on carbon nanotube gas sensors.
Research interests involve: growth or synthesis of 1D and 2D materials; characterization of their morphology, chemical composition and crystal quality using various microscopy and spectroscopy techniques.

EDUCATION

University of Illinois at Chicago
Ph.D. in Electrical and Computer Engineering, Spring 2016
M.S. in Electrical and Computer Engineering, Summer 2013
CGPA: 3.9/4.0

Bangladesh University of Engineering and Technology
B.Sc. in Electrical and Electronic Engineering, Spring 2008
CGPA: 3.71/4.0

PROFESSIONAL EXPERIENCE

University of Illinois at Chicago
Department of Electrical and Computer Engineering
Graduate Research Assistant (08/2009—04/2016)
Supervisor: Dr. Igor Paprotny

- Designed and fabricated a metal oxide functionalized multi-walled carbon nanotubes (MWCNT) based chemiresistor sensors which can detect ppm levels of methane at room temperature.
- Worked on various gas plasma and UV-ozone based surface treatments of multi walled carbon nanotubes.
- Worked on atomic layer deposition (ALD) of metal oxides (ZnO and SnO2) to functionalize the MWCNTs surface for selective gas sensing.
- Characterized the morphology, elemental composition and graphitic quality of the functionalized MWCNTs, respectively, by scanning electron microscope (SEM), energy dispersive x-ray spectroscopy (EDX) and Raman spectroscopy and transmission electron microscope (TEM) (mostly worked on TEM grid preparation).
- Fabricated a deep reactive ion etching (DRIE)-based stencil mask for selective functionalization of carbon nanotubes.

- Built and maintained a gas sensor calibration system which can record real time electrical signals from multiple gas sensors along with the concentration of the detectable gas, relative humidity and temperature of the system. As a super-user, was responsible for training other users, maintenance/trouble-shooting of the setup and development of the sensor testing process.
- Worked on a project to grow bi and tri-layer of molybdenum disulfide (MoS_2) on SiO_2/Si substrates using a custom-made chemical vapor deposition tool.

University of Illinois at Chicago
Department of Electrical and Computer Engineering
Teaching Assistant (08/2009—04/2016)

- As a teaching assistant taught 100, 200, 300 and 400 level lab and theory classes.
- As a teaching assistant of the course ECE 449 (MEMS Fabrication) for 3 semesters, trained different fabrication techniques and tools to graduate and undergraduate students (oxidation, metal deposition, photolithography using mask aligner, wet etching, deep reactive ion etching, HF release and critical point drying) using the cleanroom at Nanotechnology Core Facilities (NCF) of UIC.

Argonne National Laboratory, IL
Center for Nanoscale Material
Student User (09/2012—04/2016)
Supervisor: Dr. Ralu Divan

- As a certified user performed different lithography, deposition and metrology facilities inside the cleanroom of the Center for Nanoscale Material (CNM) at Argonne National Laboratory for more than 3 years.
- Project: Selectively Functionalized Carbon Nanotube Based Gas Sensor.

Lawrence Berkeley National Laboratory, CA
Indoor Environment Group
Affiliate Researcher (12/2014—04/2016)
Supervisor: Dr. Lara Gundel

- Developed a gas sensor calibration system which, in parallel, can record real time electrical signal from multiple gas sensors along with the concentration of the detectable gas, relative humidity and temperature inside the system.
- Project: Selectively Functionalized Carbon Nanotube Based Gas Sensor.

United International University, Dhaka, Bangladesh
Department of Electrical and Communication Engineering
Lecturer (06/2008—06/2009)

- Taught 100, 200, 300 and 400 level undergraduate lab and theory classes

Eastern University, Dhaka, Bangladesh
Department of Electrical and Communication Engineering
Lecturer (01/2008—05/2008)

- Taught 100, 200, 300 and 400 level undergraduate lab and theory classes

EXPERTISE
Device Fabrication:

- Standard lithography processes: Spin coating photoresists, development, lift-off, wet etching, and release.
- Photolithography: Direct laser writer (LW 405), MJB 3, and MA6 mask aligner.
- Metal deposition: Electron-beam evaporation (Varian).
- Atomic Layer Deposition: Arradiance Gemstar.
- Reactive Ion Etching: March CS-170.
- Deep Reactive Ion Etching: Oxford Plasma.
- UV-Ozone Treatment: Nanomax Ultra-100 tool.
- Profilometer: KLA Tencor.
- Dicing Saw: Thermocarbon (TCAR 864-1).

Characterization:

- Raman Spectroscopy: Renishaw Invia, Renishaw 2000.
- Photoluminescence: Horiba Jobin-Yvon Nanolog Spectrofluorimeter
- Scanning Electron Microscopy (SEM): TESCAN VEGA3, Raith 150.
- Energy dispersive x-ray spectroscopy (EDS): TESCAN VEGA3.
- 4-point and 2-point probe current-voltage characterization: Various Keithley/Agilent sources and meters programmed with LabVIEW.

Software and Programming Languages:

- L-Edit, Clewin, AutoCAD, 3ds Max, MATLAB, C, C++, ATLAS, COMSOL, P-SPICE, LT-SPICE, CADENCE, Casa XPS, LaTex, MS Office, HTML.

AWARD

- CNM best student poster prize: 2015 Advanced Photon Source (APS)/ Center for Nanoscale Material (CNM) Users Meeting, Argonne National Laboratory, IL, USA.

ACHIEVEMENT

- A write-up on the following article was featured in the "AVS Beneath the Surface" newsletter, December 2015 issue:

- Md Humayun, R. Divan, Y. Liu, L. Gundel, P. Solomon, and I. Paprotny, Novel chemoresistive CH_4 sensor with 10 ppm sensitivity based on multi-walled carbon nanotubes (MWCNTs) functionalized with SnO_2 nanocrystals. Journal of Vacuum Science and Technology A, 34, 01A131 (2016). http://dx.doi.org/10.1116/1.4936384

- The above article was featured as the editor's pick on the Journal of Vacuum Science and Technology A (JVST-A), Dec 2015 — Feb 2016.

PUBLICATIONS/PRESENTATIONS
Journals:

- Md Humayun, R. Divan, Y. Liu, L. Gundel, P. Solomon, and I. Paprotny, "Novel chemoresistive CH4 sensor with 10 ppm sensitivity based on multi-walled carbon nanotubes (MWCNTs) functionalized with SnO2 nanocrystals". Journal of Vacuum Science and Technology A, 34, 01A131 (2016). http://dx.doi.org/10.1116/1.4936384
- Md Humayun, R. Divan, L. Stan, A. Gupta, D. Rosenmann, L. Gundel, P. Solomon, and I. Paprotny, "ZnO functionalization of multiwalled carbon nanotubes for methane sensing at single parts per million concentration levels", Journal of Vacuum Science and Technology B, 33, 06FF01 (2015). http://dx.doi.org/10.1116/1.4931694
- Md Humayun, R. Divan, L. Stan, D. Rosenmann, D. Gosztola, L. Gundel, P. A. Solomon, I. Paprotny "Ubiquitous Low-cost Functionalized Multi-Walled Carbon Nanotube Sensors for Distributed Methane Leak Detection", Submitted on 03/01/2016 to IEEE Sensors Journal. Under review.
- Md Humayun, R. Divan, R. Rosenberg, L. Gundel, P. Solomon, and I. Paprotny,"Effects of O_2 plasma and UV-O_3 assisted surface pre-activation on high sensitivity metal oxide functionalized multi-walled carbon nanotube CH_4 sensors", In preparation.

Conference Proceedings:

- Md Humayun, R. Divan, L. Stan, D. Rosenmann, D. Gosztola, L. Gundel, P. A. Solomon, I. Paprotny "Functionalized Multi-Wall Carbon Nanotube based Sensors for Distributed Methane Leak Detection", Proceeding of *IEEE Sensors* Conference, November 1-4 2015, Busan, South Korea. 10.1109/ICSENS.2015.7370207

- Md Humayun, J. Gjanci and M. Chowdhury, "On-Chip Voltage Regulator Without Physical Inductor", paper 8256, Proceeding of 10th IEEE International NEWCAS Conference, Montreal, Canada, June 17 - 20, 2012. 10.1109/NEWCAS.2012.6328967

Conference Presentations:

- Md Humayun, R. Divan, L. Stan, Y. Liu, I. Paprotny, "Atomic Layer Deposition of ZnO Nanoparticles on Multi-Walled Carbon Nanotubes (MWCNTs) as a Functionalization Compound for Methane Sensing Application", 15th International Conference on Atomic Layer Deposition 2015, Portland, Oregon, USA (Oral presentation).
- Md Humayun, R. Divan, L. Stan, A. Gupta, D. Rosenmann, L. Gundel, P. Solomon and I. Paprotny, "ZnO Functionalization of Multi-walled Carbon Nanotubes for PPM Level Methane Sensing", The 59th International Conference on Electron, Ion, and Photon Beam Technology and Nanofabrication, 2015, San Diego, USA (Invited poster presentation).
- Md Humayun, R. Divan, L. Stan, A. Gupta, D. Rosenmann, Y.Liu, L. Gundel, P. Solomon, and I. Paprotny, "ZnO Functionalization of Surface Pre-treated Multi-walled Carbon Nanotubes for Methane Sensing", Poster presentation, 2015 APS/CNM Users Meeting, May 11-May14. (CNM best student poster).
- Md Humayun, "Functionalized Carbon Nanotubes Based Methane Sensing", Invited Speech, Center for Nanoscale Material, Argonne National Laboratory, IL, January 27th, 2015.
- K. G. Punchihewa, E. Zaker, R. Kuljic, A. Rangaraj, M. Liu, M. Purahmad, H. Saboonchi, A. Vesa, G.Gezahegne, C.Hughes, Md Humayun et al, "Improvements of the Sensitivity and Operating Range of MEMS-based Resistive-type Vacuum Gauges", Technical Digest, 24th International Vacuum Nano-electronics Conference, paper O10-5, p.50, July 18 - 22, Wuppertal, Germany (2011).
- Md Humayun, R. Divan, L. Stan, D. Gosztola, L. Gundel, P. A. Solomon, I. Paprotny "UV-Accelerated Detection and Recovery of CH4 in ZnO Functionalized Multi-walled Carbon Nanotube Sensors", Abstract submitted for the 60th International Conference on Electron, Ion, and Photon Beam Technology and Nanofabrication, 2016, Pittsburgh, PA

PROPOSALS

- "Selectively Functionalized Carbon Nanotube Based Methane Sensor", Principal Investigators: Igor Paprotny, Ralu Divan, and Md Tanim Humayun, Center For Nanoscale Materials, Argonne National Laboratory, Proposal No. 41099, Granted for the year January 2015 — January 2016.
- "Functionalized Carbon Nanotube based Chemoresistive Methane Sensor", Principal Investigators: Md Tanim Humayun, Igor Paprotny, and Ralu Divan, Center For Nanoscale Materials, Argonne National Laboratory, Proposal No. 45862, Granted for the year January 2016 — January 2017.

PROFESSIONAL SOCIETIES

- Institute of Electrical and Electronics Engineers (IEEE)